

Numerical Investigation of Foam Mixing in Gypsum Slurry

By

DOMINIC A. DANNESSA

MS, Youngstown State University, USA, 1981.

DISSERTATION

Submitted as a partial fulfillment of the requirements

for the degree of Doctor of Philosophy in Mechanical Engineering

in the Graduate College of the

University of Illinois at Chicago, 2017

Chicago, Illinois

Defense Committee:

Alexander L. Yarin,	Chair & Advisor
Michael J. Scott,	Department of Mechanical & Industrial Engineering, UIC
W. J. Minkowycz,	Department of Mechanical & Industrial Engineering, UIC
Kenneth Brezinsky,	Department of Mechanical & Industrial Engineering, UIC
Farhad Ansari,	Department of Civil & Materials Engineering, UIC

This Thesis is dedicated to my dear wife Josette and our daughters Lieutenant Susie Dannessa, United States Coast Guard and Kate Dannessa, Rhode Island School of Design, without whose constant support, encouragement and visualization of a dream this work would not have been possible.

They continue to be my inspiration, pride and joy from the beginning to completion of this work to what lies ahead in the future.

ACKNOWLEDGEMENTS

Prior to the reader starting to review this dissertation, I would like to acknowledge those individuals without whose inspiration, support and guidance I would not have been able to accomplish this work.

First, I would like to thank my parents Amil and Mary Dannessa, both now deceased. They stressed the importance of academics and striving to do your best at all times. They taught me that persistence, hard work and doing the right things would always pay off in the end despite of obstacles. They believed higher education was the path to a better future. Completion of this Thesis and PhD program completes the loop on something they encouraged me to pursue more than thirty years ago.

I am grateful for the excellent overall education I received at Woodrow Wilson High School in Youngstown, Ohio and the superb technical education I received in obtaining my Bachelor of Engineering and Masters of Engineering Degrees in Mechanical Engineering at Youngstown State University. I would like to recognize Dr. Frank D'Isa, retired Mechanical Engineering Department Head, for his mentoring and academic training during those years.

In the present time, I must most especially thank my dear wife Josette and our children Susie and Kate for providing me continuous support and inspiration throughout this long process and giving me the courage to never quit. They never flinched in their belief that I should do this and never made an issue of the time commitment. Every spare minute I

had they reminded me to work on the Thesis. When I started this they were beginning High School and both now have budding careers. My wife has been the model of understanding.

It was at the very beginning of this process Professor Constantine Megaridis gave me the vision, courage and confidence that obtaining a PhD at my age, having been out of school for thirty years, was not only doable but a good thing for my Company, UIC, my family and myself personally. He convinced me to try. He was quite persuasive that after having been in the business world for decades my brain was clouded by the grey and this academic pursuit would not only open my mind to fresh and creative thought processes but expose me to different bright people, young and diverse points of view, and a direct current understanding of what was important to our young people. He guaranteed it to be exciting and ultimately would open doors for others and add years to my life. So far he has been correct on all points and I hope so on the life expectancy as well! I am forever indebted to him for his insight into me and his vision.

I want to express my thanks to my employer of nearly four decades, USG Corporation, for provided ongoing opportunity and technical challenge in a variety of positions as well as an environment that encourages continuous learning. In particular, my direct superior and friend for 25 years, Jim Metcalf, retired Chairman and CEO of USG Corporation has been a constant and patient supporter of this endeavor and has provided ongoing inspiration to completion. I also want to recognize two of my outstanding colleagues at

our Corporate Innovation Center, Dr. Srinivas Veeramasuneni and Dr. Kumar Natesaiyer for their technical support and guidance.

Next, I give my heartfelt thanks to Dr. Suman Sinha Ray, who is not only my young colleague, but professor, sounding board and chief motivator in navigating the Thesis protocol in a meticulous fashion. Without his guidance and incessant challenge the process would have been much more inefficient and painstaking.

Lastly, I have been honored to have the brilliant distinguished Professor Alexander Yarin as my mentor. It is a rarity in life and privilege to have been able to work so closely with such a renowned scientist and experienced academic leader. He, like Professor Megaridis, gave me the insight and confidence to pursue this dream while understanding the realities of my work and family obligations. He also provided great humor, historical context and business relevance to the project. I am blessed to have become a friend of such a great man.

I express my wholehearted gratitude to my thesis committee members for their assistance and time in achieving my Thesis goals.

To conclude, I thank God above for giving me the persistence, knowledge, opportunity, relationships and family to have successfully pursued this endeavor.

TABLE OF CONTENTS

<u>CHAPTER</u>	<u>PAGE</u>
1. INTRODUCTION.....	1
2. BACKGROUND AND LITERATURE REVIEW	6
2.1 Practical Motivation.....	6
2.2 Interaction of Foam with Non-Newtonian Fluid.....	12
2.3 Rheological Characterization of Complex Fluids.....	16
2.4 Non-Newtonian Fluid Jets.....	33
3. STRAIGHT FOAM JET INJECTED INTO SLURRY: PROBLEM FORMULATION.....	39
3.1 Governing Equations for the Boundary Layer of the Power-Law Two-Phase Matter.....	39
3.2 The Boundary Conditions.....	41
3.3 The Integral Invariants.....	43
3.4 Dimensionless Form of the Governing Equations.....	49
3.5 Density of Foam-slurry Mixtures.....	52
3.6 Viscosity of Stucco-Water-Foam Suspensions.....	53
4. STRAIGHT FOAM JET INJECTED INTO SLURRY: NUMERICAL METHOD	55
4.1 Coordinate Transformation for Numerical Solution.....	55
4.2 Numerical Solution Algorithm.....	60
4.3 Treatment of the Boundary Conditions in Numerical Simulations.....	63
5. NUMERICAL RESULTS FOR STRAIGHT FOAM JETS ISSUED INTO SLURRY.....	68
5.1 The Results for WSR 68.....	68
5.2 The Effect of WSR: WSR 75 in Comparison with the results for WSR 68.....	87
6. FOAM JET ISSUED in CROSS-FLOW of SLURRY.....	94
6.0 Introduction.....	94
6.1 Governing Equations for the Foam Jet in Cross-Flow of Slurry.....	94
6.2 Results and Discussion.....	102
6.3 Results and Discussion.....	103
7. CONCLUSIONS.....	113
8. REFERENCES	115

9. APPENDIX 1: Computer code in FORTRAN developed to predict flow in straight foam jets issued into stagnant slurry.....	125
10. APPENDIX 2: Computer code in FORTRAN developed to predict flow in foam jets issued into slurry cross-flow.....	138
VITA.....	153

LIST OF TABLES

<u>TABLES</u>	<u>PAGE</u>
2.2.1 Summary of previous investigations on the rise velocity discontinuity of bubbles in non-Newtonian fluids. (Courtesy of Amirnia et al. 2013).....	15
2.3.1 Basic Geometric Shape Factor.....	21
2.3.2 Summary of extensional rheometer designs and application ranges.....	23
3.6.1 The coefficients involved in the empirical Eqs. (3.6.2) and (3.6.3).....	54
5.1.1 Input files for the FORTRAN code described in detail in Appendix.....	69

LIST OF FIGURES

<u>FIGURE</u>	<u>PAGE</u>
1.1. Schematic of gypsum wallboard manufacturing process. (Picture courtesy- United States Gypsum Corporation).....	3
1.2. (a) Gypsum wallboard at a construction site being carried on a boom truck. (b) Gypsum wallboard at a construction site is being carried by a construction site worker. (c) Stack of gypsum wallboard and the cross-section of gypsum wallboard.....	4
2.1.1. Total industry shipment during year 2005-2015. In the figure Res, Non Res and R&R stand for residential, non-residential and repair & remodel, respectively.....	7
2.1.2. A typical foam mixer in gypsum wallboard forming line.....	11
2.3.1. Stress relaxation for viscoelastic and rubbery materials (te Nijenhuis2008).....	18
2.3.2. (a) Semi-logarithmic plot of the reduced relaxation modulus $G_{red}(t) = G(t)/G = \sigma(t)/\sigma_0$ for two Maxwell elements, with relaxation times of 1 s and 10,000 s, respectively. (b) Semi-logarithmic plot of the relaxation of the reduced stress σ/σ_0 for the Maxwell-Wiechert model, with relaxation times of 1 s and 10,000 s and spring constants G_1 and $G_2 = 0.5G_1$; the results of (a) are also shown (te Nijenhuis 2008).....	19
2.3.3. Shearing a thixotropic liquid after short and long rest times. The inset shows breakdown of an idealized two-dimensional (2D) thixotropic system: (a) completely structured - giving elastic, solid- like behavior; (b) partly structured - giving a viscoelastic response; and (c) completely unstructured - giving a viscous, shear-thinning response (Barnes 2008).....	26

LIST OF FIGURES(CONTINUED)

<u>FIGURE</u>	<u>PAGE</u>
2.3.4. (a.) Schematic of Elongation Rheometer. (b) Self-thinning of a cylindrical liquid thread, driven by surface tension, namely, by the pressure gradient $\alpha/a > \alpha/R$. (c) Example of the evolution of a self-thinning gypsum thread. In the insets, the snapshots of the gypsum thread in the Elongation Rheometer are shown. (Sinha-Ray 2011).....	31
2.3.5. Experimental values of K and n for foamed gypsum at 68 and 75 WSR with different foam contents. The experimental values are fitted using a polynomial function. (Jun 2013).....	33
2.4.1. Evolution of jet profile in cross-flow [Obtained with permission from No et al. (2015).....	34
2.4.2 The evolution of laminar-turbulent jet profile (from Kumar et al.1984).....	36
3.1.1. Sketch of axisymmetric submerged jet of foam issued into slurry.....	39
3.2.1. Nozzle exit conditions.....	41
3.2.2. Velocity boundary conditions.....	42
3.2.3. The unphysical velocity profiles excluded by the boundary conditions (3.2.2).....	43
3.3.1. Sketch of the axial momentum flux in jet.....	44
4.1.1. Integration domain in new coordinates.....	56
4.2.1 Semi-discretization of the partial differential equations.....	60
4.3.1. Posing boundary conditions in the $\xi\eta$ -plane.....	63
4.3.2. The initial conditions at the nozzle exit.....	65
4.3.3. The integration domain and the initial and boundary conditions.....	67

LIST OF FIGURES(CONTINUED)

<u>FIGURE</u>	<u>PAGE</u>
5.1.1. Dependence of the effective viscosity on R_0 (the values shown in the panels are in centimeters). (a) $Sc=18$, (b) $Sc=30$. The value of $x=0.04$. WSR68.....	71
5.1.2. Dependence of half-jet width on the nozzle radius R_0 (the values shown in the panels are in centimeters). (a) $Sc=18$, (b) $Sc=30$. WSR 68.....	72
5.1.3. Dependence of the longitudinal velocity profile on the nozzle radius R_0 (the values shown in the panels are in centimeters). (a) $Sc=18$, (b) $Sc=30$. The value of $x=0.04$. WSR 68.....	73
5.1.4. Profiles of the foam content ϕ at different values of the nozzle radius (the values shown in the panels are in centimeters). (a) $Sc=18$, (b) $Sc=30$. The value of $x=0.04$. WSR 68.....	74
5.1.5. Foam content in the submerged jet. The following values of the parameters were used: $v_z=1000$, $R_0=1.9$ cm, $Sc= 30$. The panel (a) shows the global view, whereas panel (b) shows the zoomed-in views of the central part of the jet. WSR 68.....	75
5.1.6. Dependence of the effective viscosity on the radial coordinate in the jet cross-section at different values of the Schmidt number. (a) $v_{z0}=500$ cm/s, (b) $v_{z0} =1000$ cm/s. The value of $x=0.04$. WSR 68.....	76
5.1.7. Dependence of half jet width for different values of the Schmidt number Sc . Panel (a) $v_{z0} =500$ cm/s, panel (b) $v_{z0} =1000$ cm/s. WSR 68.....	77
5.1.8. The axial velocity profiles at different values of the Schmidt number and for the following two values of the initial velocity of the foam jet: (a) $v_{z0}=500$ cm/s, (b) $v_{z0} =1000$ cm/s. The value of $x=0.04$. WSR 68.....	78
5.1.9. Dependence of the foam content on the radial coordinate in the jet cross-section predicted at different values of the Schmidt number Sc at two values of the initial velocity of the foam jet: (a) $v_{z0} =500$ cm/s, (b) $v_{z0} =1000$ cm/s. The value of $x=0.04$. WSR 68.....	79

LIST OF FIGURES(CONTINUED)

<u>FIGURE</u>	<u>PAGE</u>
5.1.10. Profiles of the effective viscosity at different values of the initial foam jet velocity v_{z0} (shown in the insets in cm/s). (a) $Sc=18$, (b) $Sc=30$. The value of $x=0.04$. WSR 68.....	80
5.1.11. Variation of the half jet width at different values of the initial foam jet velocity v_{z0} (shown in the insets in cm/s). (a) $Sc=18$, (b) $Sc=30$.....	81
5.1.12. Longitudinal velocity profiles at different values of the initial foam jet velocity v_{z0} (shown in the insets in cm/s). (a) $Sc=18$, (b) $Sc=30$. The value of $x=0.04$. WSR 68.....	82
5.1.13. Dependence of the foam content on the radial coordinate in the jet cross-section predicted at different values of the initial foam jet velocity v_{z0} (shown in the insets in cm/s). (a) $Sc=18$, (b) $Sc=30$. The value of $x=0.04$. WSR 68.....	83
5.1.14. Foam content in the submerged jet. The panels (a1), (b1) and (c1) show the global views, whereas panels (a2), (b2) and (c2) show the zoomed-in views of the central part of the jet. Specifically, for panels (a1)-(a2) $v_z=500$ cm/s, $R_0=1.9$ cm, $Sc=18$; for panels (b1)-(b2) $v_z=1000$ cm/s, $R_0=1.9$ cm, $Sc=18$; for panels (c1)-(c2) $v_z=1000$ cm/s, $R_0=1.9$ cm, $Sc=30$. WSR 68.....	84
5.1.15. The longitudinal velocity field in the submerged jet. The panels (a1), (b1) and (c1) show the global views, whereas panels (a2), (b2) and (c2) show the zoomed-in views of the central part of the jet. Specifically, for panels (a1)-(a2) $v_z=500$ cm/s, $R_0=1.9$ cm, $Sc=18$; for panels (b1)-(b2) $v_z=1000$ cm/s, $R_0=1.9$ cm, $Sc=18$; for panels (c1)-(c2) $v_z=1000$ cm/s, $R_0=1.9$ cm, $Sc=30$. WSR 68.....	86
5.2.1. Longitudinal velocity profiles in the jet for the Schmidt number of $Sc=10$. The value of $x=0.04$. The initial velocity of the foam jet $v_{z0}=500$ cm/s. The results for WSR 68 are shown in the left panel, and for WSR 75-in the right panel.....	87
5.2.2. Foam content profiles in the jet for the Schmidt number of $Sc=10$. The value of $x=0.04$. The initial velocity of the foam jet $v_{z0}=500$ cm/s. The results for WSR 68 are shown in the left panel, and for WSR 75-in the right panel.....	88

LIST OF FIGURES(CONTINUED)

<u>FIGURE</u>	<u>PAGE</u>
5.2.3. The effective viscosity profiles in the jet for the Schmidt number of $Sc=10$. The value of $x=0.04$. The initial velocity of the foam jet $v_{z0}=500$ cm/s. The results for WSR 68 are shown in the left panel, and for WSR 75-in the right panel.....	88
5.2.4. Half-widths of the jet for the Schmidt number of $Sc=10$. The initial velocity of the foam jet $v_{z0}=500$ cm/s. The results for WSR 68 are shown in the left panel, and for WSR 75-in the right panel.....	89
5.2.5. Longitudinal velocity profiles in the jet for the Schmidt number of $Sc=10$. The value of $x=0.04$. The radius the nozzle issuing the jet was $R_0=1.9$ cm. The results for WSR 68 are shown in the left panel, and for WSR 75-in the right panel.....	89
5.2.6. Foam content in the jet for the Schmidt number of $Sc=10$. The value of $x=0.04$. The radius the nozzle issuing the jet was $R_0=1.9$ cm. The results for WSR 68 are shown in the left panel, and for WSR 75-in the right panel.....	90
5.2.7. The effective viscosity profiles in the jet for the Schmidt number of $Sc=10$. The value of $x=0.04$. The radius the nozzle issuing the jet was $R_0=1.9$ cm. The results for WSR 68 are shown in the left panel, and for WSR 75-in the right panel.....	90
5.2.8. Half-widths of the jets. The Schmidt number of $Sc=10$. The radius the nozzle issuing the jet was $R_0=1.9$ cm. The results for WSR 68 are shown in the left panel, and for WSR 75-in the right panel.....	91
5.2.9. Longitudinal velocity profiles (left) and the foam content profiles (right) in the jet for the Schmidt number of $Sc=10$. The value of $x=0.04$. The radius the nozzle issuing the jet was $R_0=1.9$ cm.....	92
5.2.10. The effective viscosity profiles in the jet for the Schmidt number of $Sc=10$. The value of $x=0.04$. The radius the nozzle issuing the jet was $R_0=1.9$ cm.....	92

LIST OF FIGURES(CONTINUED)

<u>FIGURE</u>	<u>PAGE</u>
5.2.11. Half-widths of the jets. The Schmidt number of $Sc=10$. The radius the nozzle issuing the jet was $R_0=1.9$ cm.....	93
6.1.1. Sketch of foam jet issued in cross-flow of slurry.....	95
6.1.2. The jet axis slope.....	99
6.3.1. The foam jet characteristics for two values of the water-to-slurry ratio (WSR): WSR 75 (the left-hand side columns, i.e. panels with numerals “1”) and WSR 68 (the right-hand side columns, i.e. panels with numerals “2”) in the case of the normal injection of the foam jet, i.e. $\alpha_0=\pi/2$ at the Schmidt number $Sc=18$. Panels “a” show the variation of air volume fraction along the arc length of the jet. Panels “b” show the variation of the centerline velocity along the arc length of the jet. Panels “c” show shapes of the jet centerline. Different values of the cross-flow velocity U_B shown in the panels correspond to curves of different colors.....	105
6.3.2. The foam jet characteristics for two values of the water-to-slurry ratio (WSR): WSR 75 (the left-hand side columns, i.e. panels with numerals “1”) and WSR 68 (the right-hand side columns, i.e. panels with numerals “2”) in the case of the normal injection of the foam jet, i.e. $\alpha_0=\pi/2$ at the Schmidt number $Sc=30$. Panels “a” show the variation of air volume fraction along the arc length of the jet. Panels “b” show the variation of the centerline velocity along the arc length of the jet. Panels “c” show shapes of the jet centerline. Different values of the cross-flow velocity U_B shown in the panels correspond to curves of different colors.....	107
6.3.3. Effect of variation of the slurry injection angle α on the foam jet flow characteristics for two values of the water-to-slurry ratio (WSR): WSR 75 (the left-hand side columns, i.e. panels with numerals “1”) and WSR 68 (the right-hand side columns, i.e. panels with numerals “2”). The cross-flow velocity $U_B=0.333$. The Schmidt number $Sc= 18$. The results for the injection angles $\alpha= 0^\circ, 10^\circ, 30^\circ, 45^\circ, 60^\circ, 80^\circ$, and 90° are shown by different colors. The results for $\alpha=90^\circ$ correspond to those in Figure 6.3.1 for $U_B=0.333$	109

LIST OF FIGURES(CONTINUED)

<u>FIGURE</u>	<u>PAGE</u>
6.3.4. Effect of variation of the slurry injection angle α on the foam jet flow characteristics for two values of the water-to-slurry ratio (WSR): WSR 75 (the left-hand side columns, i.e. panels with numerals “1”) and WSR 68 (the right-hand side columns, i.e. panels with numerals “2”). The cross-flow velocity $U_B=0.333$. The Schmidt number $Sc= 30$. The results for the injection angles $\alpha= 0^\circ, 10^\circ, 30^\circ, 45^\circ, 60^\circ, 80^\circ$, and 90° are shown by different colors. The results for $\alpha=90^\circ$ correspond to those in Figure 6.3.1 for $U_B=0.333$.....	110
6.3.5. The foam jet characteristics for WSR 75 (the left-hand side columns, i.e. panels with numerals “1”) and the Schmidt number $Sc=18$ at different values of the cross-flow velocity. The results resolve the situation at the high values of the initial foam jet obliquity. Namely, (a) corresponds to $\alpha=70^\circ$, (b)- to $\alpha=80^\circ$, and (c) - to $\alpha=90^\circ$. All the three panels depict variation of the axial velocity along the jet. Different values of the cross-flow velocity U_B shown in the panels correspond to curves of different colors.....	111

SUMMARY

Gypsum is one of the most common and widely used building materials. It has been used for centuries in a variety of construction applications. Its unique ability to convert to a moldable rock-like structure with moderate temperature to a shapeless powder known as stucco, or Plaster of Paris, and then become moldable back to a rock-like stature upon rehydration with water makes it ideal as a building material. It also has the ability to absorb large amounts of heat that enable it to possess high fire resistance properties.

In the early 1900's, processes were developed to sandwich a gypsum core between two sheets of specially finished paper to create plasterboard, commonly known as wallboard or Sheetrock, as branded by its inventors, US Gypsum Company. Its low cost, ease of installation, fire resistance, good acoustical properties, aesthetics and design possibilities have made gypsum wallboard the standard of wall construction for decades.

Modern gypsum wallboard is made in a continuous process on high-speed production lines. Over the decades, means were developed to inject foam into the gypsum slurry which produced the core. This technique was used to reduce weight, improve acoustics and enable desirable handling properties.

The key element of the process is the mixer where stucco, water, and additives are rapidly combined. Gypsum formulation and slurry is an extremely complex fluid exhibiting non-Newtonian shear-thinning behavior, as well as time and temperature dependence to set up. A critical component is the injection or spraying of foam into the moving gypsum slurry as it emerges from the mixer. Due to the inherent complexities of the fluids, the past design approaches have been empirical in nature and based on costly,

time-consuming trial and error methodologies which at best have produced “rules of thumb”. Though workable, current manufacturing processes are both energy and water intensive. Overall, foam injection into a non-Newtonian slurry is in itself extremely complex and has not been extensively studied or modeled before.

The aim of this work is to study the effect of foam mixing with gypsum slurry. This study was conducted in two steps. At first, numerically, injection of foam in stagnant gypsum slurry was studied. Gypsum slurry with two different water stucco ratios (WSR), 68 and 75, was studied. In this study non-Newtonian multiphase behavior resulting from the interaction between foam and gypsum was incorporated. The effect of foam nozzle diameter, Schmidt number and foam injection velocity on mixing of foam and gypsum slurry was studied.

As an extension to this, foam mixing in flowing gypsum slurry was also studied. The effect of foam injection velocity and foam injection angle for two different Schmidt numbers, 18 and 30, and for two different WSR, 68 and 75, were studied.

It needs to be mentioned, the choice of the studying parameter in this work commensurate with practical values that are used in wallboard manufacturing plants.

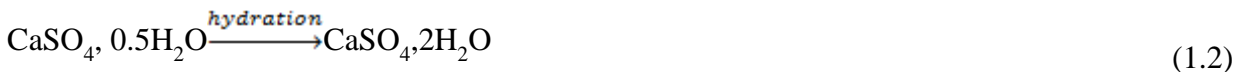
Recently, researchers developed rheological constitutive equations for both gypsum slurry and foam, and, their mixtures at several foam contents as well. This enabled us to pursue modeling of foam-slurry mixtures in conjunction with numerical analysis in the framework of the non-Newtonian hydrodynamics. This approach is proposed and implemented in the present work as a promising path toward valuable insights into the complex behavior of such a system, which was never possible before. This in-depth

understanding can yield optimization of both the mixing process and its final product-gypsum wallboards.

From an industry prospective, potential benefits can be both widespread and significant. Current energy and water intensive processes can be made more sustainable through reduction of the use of these valuable components. Other potential product attribute benefits include: reduction of weight, increasing of strength, reduction of raw material usage, improved uniformity, higher line speed, improved acoustics and better product installation characteristics. These factors all can work together to potentially reduce both product cost and transportation due to reduced weight, while providing a more sustainable proposition having improved life cycle analysis metrics.

1. INTRODUCTION

Gypsum or Calcium Sulphate dihydrate ($\text{CaSO}_4, 2\text{H}_2\text{O}$), commonly known as “Land Plaster”, is one of the Earth’s most abundant material. One of the most interesting aspects of gypsum is the various crystalline formats in which it can exist in nature: white rock (regular gypsum), transparent (selenite), colored (alabaster) or fibrous (Satin Spar). Apart from mining, synthetic gypsum is also produced by “flue gas desulfurization” (FGD) of coal fired power plants (Biondo et al., 1977; Li et al., 1999; Galos et al., 2002, Tesárek et al., 2007). Irrespective of the look, chemically all the gypsum variations are similar. Upon addition of heat to about $150\text{ }^\circ\text{C}$, every gypsum molecule loses 1.5 molecules of water and turns into stucco or Calcium Sulphate hemi hydrate, $\text{CaSO}_4, 0.5\text{H}_2\text{O}$, commonly known as “Plaster of Paris” or stucco Eq. (1.1), which upon addition of water converts back to gypsum Eq. (1.2)



The ability of stucco to convert to gypsum by addition of water renders its capability to mold into any complex shape. In addition to that, owing to the crystalline water, gypsum has a high resistance to fire. Owing to both of these, gypsum is a natural choice of building materials. In fact, the use of gypsum as a building material dates back to the Roman Empire. Gypsum panels, as a part of modern day construction, were invented by Augustine Sackett and Fred Kane in 1894. In 1898, the first patent on Sackett board involving multilayer paper and gypsum was granted. In the year of 1910, United States Gypsum (USG) bought Sackett Plaster Board Company and launched Admant Board where instead of inner layer of felt, gypsum was sandwiched between two paper facings without a wrapped edge. In 1916 gypsum board under

the brand name of “Sheetrock”, was launched by USG where the edges of the board were wrapped. However, the true uptake of gypsum wallboard in the American housing industry came after the Second World War. Rapid and economic production of housing was given the utmost importance in order to provide homes for the thousands of returning soldiers. Exacerbating this was the fact that housing construction was greatly subdued just prior to World War Two due to the Great Depression. These factors combined to create tremendous demand with short supply. Drywall construction techniques provided a much faster and less costly solution to home construction than prior wet methods.

Figure 1.1 shows a schematic of the wallboard manufacturing process. As it can be seen from Figure 1.1, raw natural gypsum rock and/or synthetic gypsum is ground to a smaller particle sized powder called landplaster and mixed with water and different additives (e.g.- starch, glass fiber etc.). This mixture, called gypsum slurry, is then sandwiched between two sheets of paper which is then rough cut to length and dried in a kiln. Upon emerging from the kiln, the boards are cut to finished lengths and bundled. Typical pictures of finished gypsum board is shown in Figure 1.2.

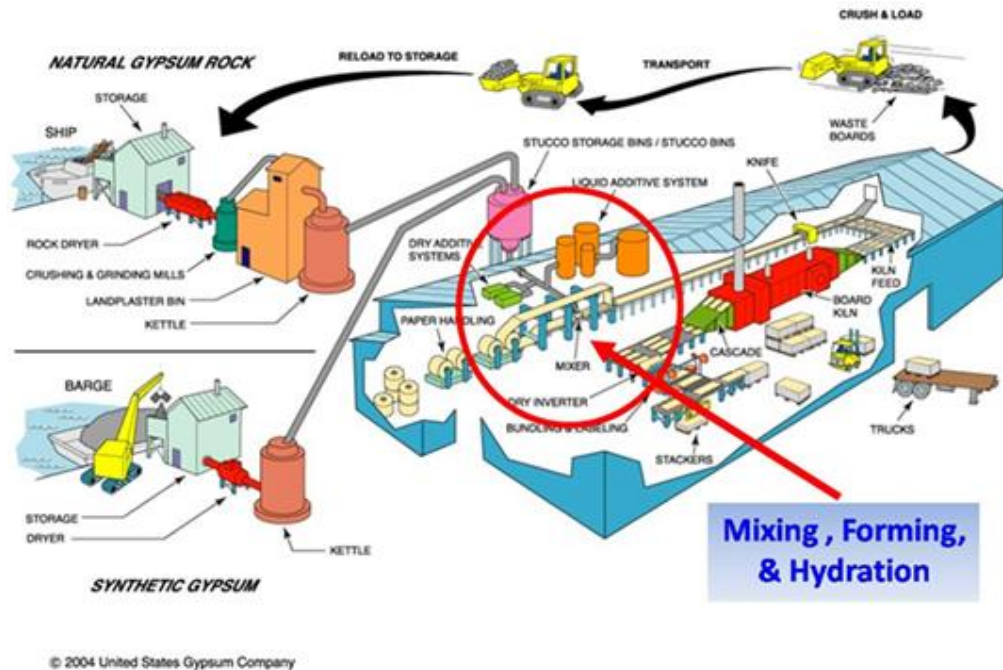


Figure 1.1. Schematic of gypsum wallboard manufacturing process. (Picture courtesy- United States Gypsum Corporation).

Figure 1.2a shows a typical construction site, where gypsum wallboard is being used and transported using a boom truck. In Figure 1.2b it is shown how on a construction site a gypsum wallboard panel is carried by workers. As is evident from the construction site, the installation of wallboard is still a manual process. Accordingly, over last two decades innovation around gypsum wallboard technology has been focused on reducing board weight to facilitate the manual handling of wallboard. This helps in two ways: (a) reduces chances of labor injury, (b) faster installation, which in turn reduces the downtime and increase the profitability. Additionally, reduced weight results in lower shipping cost. A common technique of reducing board weight is to inject foam in gypsum wallboard (cf. Figure 1.2c). In Figure 1.2c, the cross-sectional view of gypsum wallboard is exhibited where the foam structure in a board is visible.

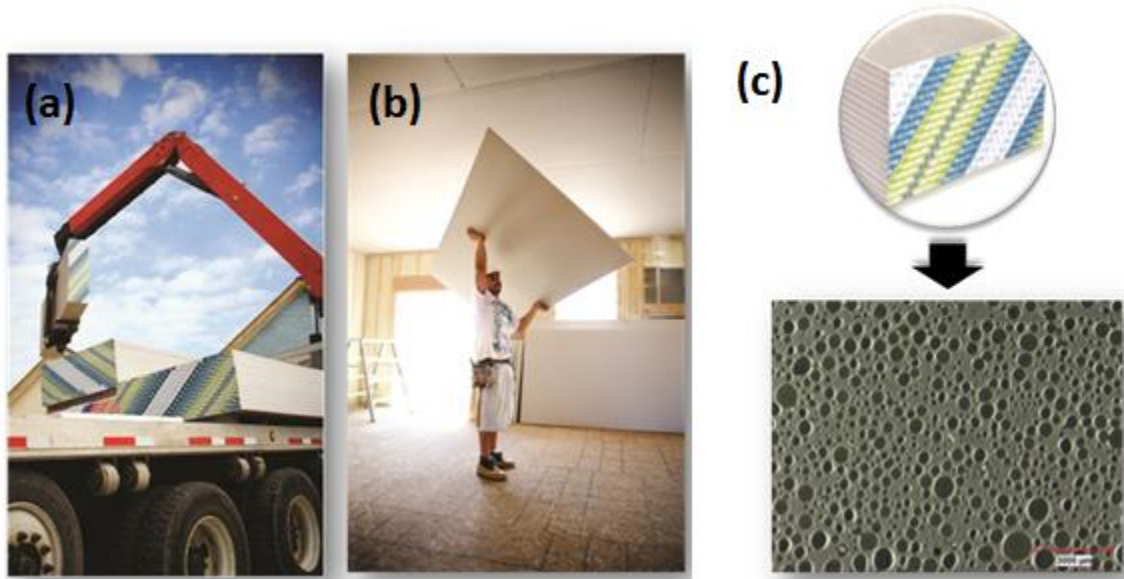


Figure 1.2. (a) Gypsum wallboard at a construction site being carried on a boom truck. (b) Gypsum wallboard at a construction site is being carried by a construction site worker. (c) Stack of gypsum wallboard and the cross-section of gypsum wallboard.

It should be emphasized that in addition to lowering the board weight, gypsum wallboard as a building material needs to meet the requirements of structural integrity, fire protection capability, surface finish, acoustics, cut ability and sag resistance among other properties. This makes the foam mixing process extremely crucial, as without well-engineered bubble structure, the structural requirement at lower weight of gypsum wallboard will not be possible (Sucech, 1997; Wittbold et al., 2011; Blackburn et al.; 2012). The control of foam structure is generally achieved by a combination of the mixing process and the surfactant used to create the foam. So, a detailed understanding of the phenomenon of foam mixing with gypsum slurry is extremely important to optimize the process of wallboard manufacturing at a lower price point.

In this work, the effect of foam mixing with gypsum slurry is systematically studied in a theoretical and numerical framework. This thesis is organized as follows. Chapter 2 provides background and literature review with regard to the work. Chapter 3 describes the research design and objective. In Chapter 4, the interaction of single foam jet with stagnant gypsum slurry is studied numerically. Chapter 5 details the interaction of a foam jet with moving gypsum slurry. Finally, Chapter 6 concludes the overall study.

This proposed approach implemented in the present work serves as a promising path toward valuable insights into the complex behavior of such system, which was never possible before. This in-depth understanding can yield optimization of both the mixing process and its final product, gypsum wallboards.

2. BACKGROUND AND LITERATURE REVIEW

2.1. Practical Motivation

World War II was the most destructive war ever fought and lasted from 1939-1945. The war left behind a trail of destruction, wrecked infrastructure and desolation across the globe. Post World War II there was a huge unmet need for rapid construction and affordable housing. Fueled by this demand to provide housing for civilians and returning soldiers, gypsum wallboard and other lightweight panel based construction methods gained popularity. According to the Gypsum Association (<https://www.gypsum.org/about/gypsum-101/history-gypsum/>), by 1945 during World War II the United States military had alone used 2.5 billion square foot of gypsum board. By 1955, 50% of all housing was built with gypsum wallboard. During this “Postwar Economic Boom” the use of panel-based construction made its foray into commercial building due to its ability to act as an effective fire barrier and its sound insulation properties. In the early 1960’s, United States Gypsum developed shaft wall system, which led to faster adoption of gypsum wallboard into high rise commercial spaces. The John Hancock Tower and Sears Tower (now Willis Tower) are some of the tallest buildings built around that time. Presently, gypsum wallboard is considered to be the most preferred building product. In the year of 2015, the total amount of gypsum wall board sold in USA was 22.3 billion square foot. The overall demand for gypsum wallboard during last 10 years is shown in Figure 2.1.1. The global gypsum wallboard market was pegged to be at a staggering value of \$21.74 billion. (<http://www.grandviewresearch.com/industry-analysis/gypsum-board-market>).

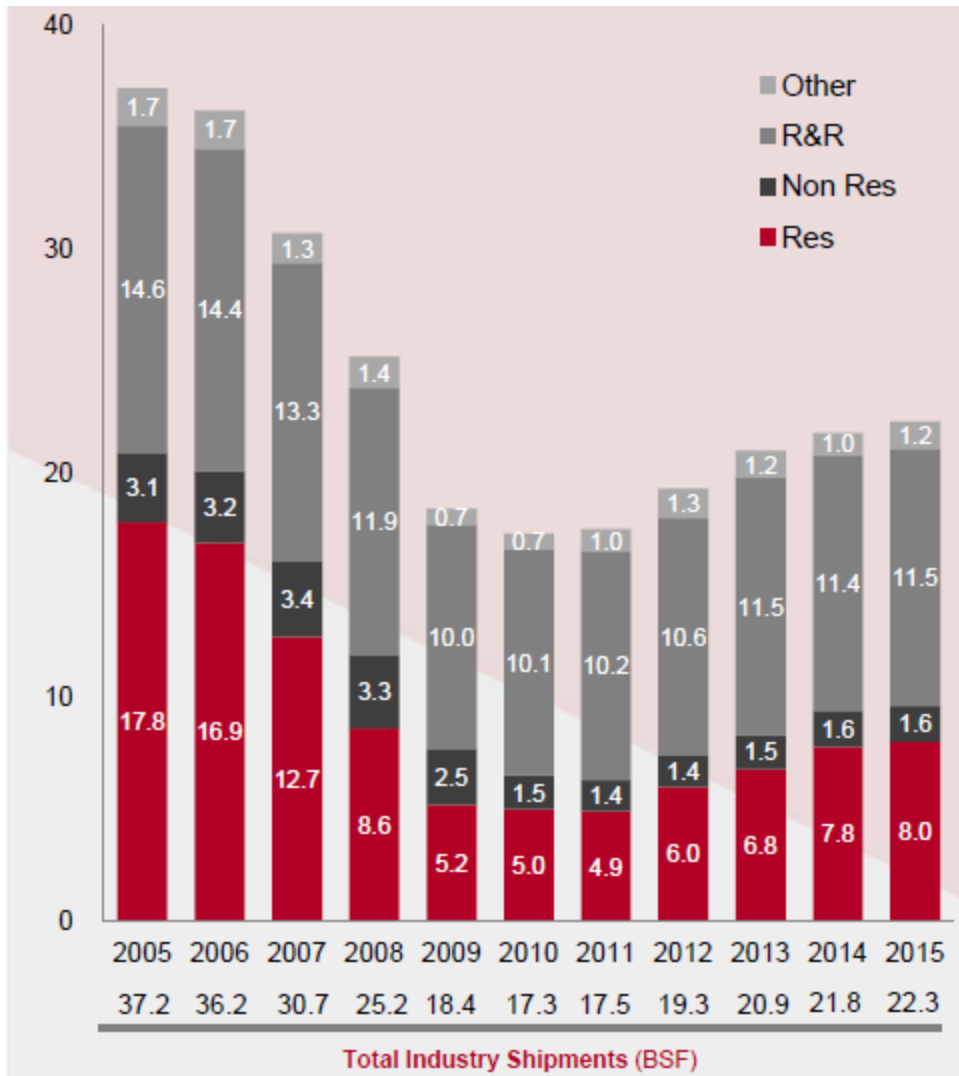


Figure 2.1.1. Total industry shipment during year 2005-2015. In the figure Res, Non Res and R&R stand for residential, non-residential and repair & remodel, respectively.

In addition to gypsum wallboard in construction, there has been significant growth in cement-based panels and precast concrete products in housing. According to recent report by Freedonia (<http://www.freedoniagroup.com/Fiber-Cement.html>), the US demand for fiber

cement-based panels in construction is forecast to grow to 2.9 billion square foot and valued as \$2.2 billion. For precast concrete products, the market size is forecast to grow to \$12.2 billion by 2018 (<http://www.freedoniagroup.com/Precast-Concrete-Products.html>).

As it was mentioned, in modern-day construction, speed of construction is one of the most prime drivers along with functionality, safety and security. A gypsum wallboard-based construction costs approximately \$5 per square foot, whereas a concrete constructions costs in the range of \$25 per square foot. In addition to the speed of construction, another primary driver for cost in construction is fatal and non-fatal injury at a construction site. In Waehrer et al. (2007) a comprehensive cost model including direct medical cost, indirect loss in wages and productivity was built, using the 2002 data from national incidence data from the Bureau of Labor Statistics. The model estimates the loss due to worker's injury to be at a staggering value of \$11.5 billion in total. It was also shown that for construction-site-related injuries, the loss per incident is approximately \$27,000 which is almost twice the value of other industries. The resulting cost was further divided among trades. It was found that the total cost due to injury related to handling of building products was over \$3 billion. These two studies clearly indicate that there is a clear need for lightweight building products.

In addition to the reduction of weight of building products, there has also been a push for reducing the carbon footprint in the production of building products to improve the sustainability. In the year of 1987, World Commission on Environment and Development (WCED) defined the concept of sustainable development as (UN Documents 1987), 'the ability to meet our current needs without compromising the ability of future generation to meet theirs'. This definition directly has huge impact on the construction industry in terms of reducing the amount of raw materials used, energy consumed in making the product and possible recycling.

One of the first steps taken by gypsum industry in the early 1970s was to use the byproduct of coal powered power plants through a process called flue gas desulfurization to create synthetic gypsum (Biondo et al., 1977; Li et al., 1999; Galos et al., 2002, Tesárek et al., 2007). This reduced the dependence on natural gypsum. However, recently due to the shifting trend of utilizing natural-gas-fueled power plants and alternative power sources in lieu of coal, the output of synthetic gypsum from coal-fired power plants is reducing. This may result in shifting the focus on natural gypsum to cater to the market need. In 2013, the domestic production of natural gypsum was estimated to be 16.3 million tons. Texas, Oklahoma, Nevada, California and Indiana together accounted for 62% of the total gypsum production.

Accordingly, as a part of sustainable development there has been an ongoing effort to reduce the weight of gypsum wallboard. It is also important to note that the gypsum wallboard manufacturing process requires significant amounts of water to create the gypsum slurry to enable the panels to be formed on the production line. Hence, the reduction in weight not only reduces the amount of raw materials but also results in lower water demand and thus lower energy requirement in creating the product. In a recent survey by Global Gypsum Magazine July 2016 edition, the total amount of CO₂ released by gypsum wallboard is ~ 24 MT/year. Although this amount may seem to be low, creating a relatively small overall footprint, it stems from the fact that the overall market size of gypsum wallboard is relatively smaller than other industries. However, when one does the calculation for amount of CO₂ emitted/unit mass the footprint can be considered to be more significant.

Similar to gypsum wallboard, cement production also results in significant energy consumption (Zhang et al., 2014). The total amount of CO₂ production attributed to cement production is much larger estimated to be 8% of global CO₂ emission (Olivier et al., 2012).

When the total emission of the cement and concrete industries are taken into account, the emission can be as large as 10% of global average (Flower et al., 2007). To reduce the emissions several steps were taken: (a) application of new technology in the format of geopolymer, calcium aluminate/sulfoaluminate cements, supersulfated slag cement etc. (Schneider et al., 2011; Gartner et al., 2011; Duxson et al., 2007); (b) utilization of energy-efficient furnace, biofuel (Damtoft et al., 2008; Sorrentino et al., 2011); and (c) reduction of clinker (Bleszynski et al., 2002). In spite of all of these actions, the race towards sustainable development still relies on a crucial point which is to reduce the amount of raw materials used by reducing the weight of the product.

In gypsum wallboard, the reduction of weight has been a primary focus of the industry and researchers at large. One of the techniques, followed in Başpınara et al. (2011) was to add light-weight silicate-based macroporous filler in gypsum slurry to create gypsum wallboard. The authors have shown that such a product will be lightweight with improved physical properties and improved fire resistance. However, such a method may be valuable for lab-based application but owing to the sheer enormity of gypsum wallboard manufacturing process, such a route will not be economically viable. As a result of this, a common technique used in gypsum wallboard manufacturing is to add a foam producing agent (soap/surfactant) into the gypsum slurry. Figure 2.1.2 shows a typical foam mixing process in gypsum slurry. In a standard foamed gypsum slurry making process, foam is injected into gypsum slurry coming out of the mixer and before hitting the forming table. There is a plethora of literature discussing utilization of foam mixing in gypsum slurry and its use in reducing gypsum board weight slurry and its use in reducing gypsum board weight (Wittbold et al., 2002; Kawamura et al., 2015). One such bright example in the present-day US marketplace is USG Sheetrock Brand Ultralight Gypsum boards, where the

gypsum wallboard is 35% lighter than standard wallboard for similar strength performance. For such a product, significant amount of research was focused on bubble structure, which relied heavily on foam chemistry and foam mixing dynamics in flowing gypsum slurry.

In the cement and concrete industry, significant emphasis was put towards production of foamed concrete (Tonyan et al., 1992; Hilal et al., 2015; Krämer et al., 2015; Narayanan et al., 2000; Alengaram et al., 2013). Injecting foam in the concrete industry is also a very well-practiced process, and both chemical and mechanical foaming processes were incorporated. The basic focus of such a process has been to reduce the weight of concrete.

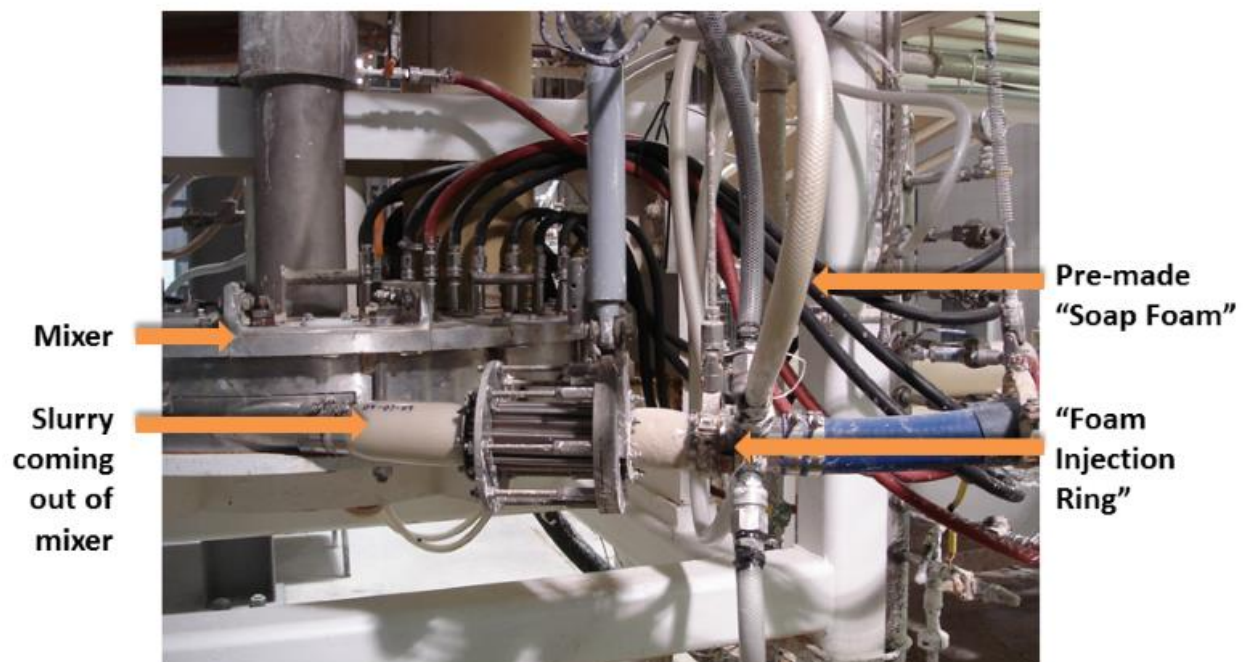


Figure 2.1.2. A typical foam mixer in gypsum wallboard forming line.

However, in all these processes the optimization of the foam mixing process is done by trial and error. The general practice in the construction industry is to optimize the foam mixing

process by improving chemistry of the foaming agent. There is a significant lack of knowledge in elucidating the dynamics of mixing of foam in slurry made from construction material, which are highly non-Newtonian in nature. In the following subsection, an in-depth literature review of the interaction of foam with non-Newtonian fluid is given.

2.2. Interaction of Foam with Non-Newtonian Fluid

All the construction material slurries, gypsum, cement etc., are non-Newtonian in nature. A detailed description of the rheological characterization of complex fluids is given in Section 2.3. It is of the utmost interest to understand the interaction of foam with a non-Newtonian fluid. Several works in the literature were found to be dealing with interaction of foam with non-Newtonian fluid.

In Li et al. (1997), the authors studied the coalescence of bubbles in a non-Newtonian fluid from the viewpoint of chaos theory. As a choice of non-Newtonian fluid they used 1 wt% polyacrylamide (PAAm) water, 1.5 wt% PAAm in water and glycerol and 1.7 wt% carboxymethylcellulose (CMC) in water and glycerol. For their study, they used a single orifice ejecting air bubble into the above-mentioned solution at a constant gas flow rate and studied the trajectory and mutual interaction of the air bubbles produced through the orifice. In this work, it was found that although the bubbles are issued at a constant gas flow rate, as they move up in the non-Newtonian fluid bath, the separation interval between bubbles becomes irregular and the coalescence of bubbles occurs. As the bubbles passed through the fluid, it resulted in residual stress in the fluid. The relaxation of the residual stress is related to the decrease in drag. It was also found that although the ejection of the bubbles was done at periodicity, the periodicity was

lost as the distance from the orifice increased. However, it also needs to be mentioned that such a phenomenon was observed owing to the viscoelastic nature of the solution.

In Herrera-Velarde et al. (2003) the authors found that there is significant discontinuity in the bubble when they are moving in non-Newtonian fluid. The authors studied the flow field around air bubbles rising in PAAm solutions using particle image velocimetry (PIV). It was found that such discontinuity was affected by the viscoelastic properties of the fluid in which the bubbles move. It was also found that such a discontinuity can stem from the wall effect and for a given non-Newtonian fluid there is a critical size of the bubble, beyond which such a discontinuity can be observed. The authors have also studied the flow configuration around the bubble and reported the appearance of “negative-wake” in the trail of the moving bubble. They found that the appearance of a cusp on the bubble above the critical volume plays a significant role in defining the flow field around the bubble. A similar discontinuity in the rise velocity of an air bubble moving in a viscoelastic field was observed by Wild et al. (2003) and Chhabra et al. (2006). A list of such observations is shown in Table 2.2.1 taken from Amirnia et al. (2013). However, there is significant confusion around the discontinuity of velocity of air bubble in non-Newtonian viscoelastic fluids, where the authors did not observe any such discontinuity in studying rise of air bubble in xanthan gum solution.

From the viewpoint of numerical study, different approaches were taken. Zhang et al. (2010) have studied the motion of a single bubble in viscous inelastic non-Newtonian fluid using the level set method. It was found that the power-law index of a non-Newtonian power-law fluid has a considerable effect on the bubble motion. Radl et al. (2007) studied the bubble flow in non-Newtonian fluids using direct numerical simulations in order to compute the mass transfer

coefficient in fermenting media. However, due to the numerical scheme complexity, it was only possible to numerically simulate one bubble.

It can be seen from the literature survey that the current numerical and experimental studies are limited to a single bubble movement in a non-Newtonian fluid. However, for foam mixing with gypsum slurry or any other industrial-scale process such a scenario only provides an initial insight into the process. The novelty of the present work is in the attempt to bridge that gap, whereby a theoretical and numerical model will be described to elucidate the process of foam mixing with gypsum slurry. It is also aimed to differentiate between different non-Newtonian fluids, which will be done in the following subsection.

Table 2.2.1. Summary of previous investigations on the rise and velocity discontinuity of bubbles in non-Newtonian fluids (Courtesy of Amirnia et al. 2013).

Reference	Fluids and conditions	Velocity-volume discontinuity observed?	Proposed mechanism
Astarita and Apuzzo (1965)	Carbopol, CMC, ET497, and J-100	Yes, for ET 497 and J-100. No discontinuity observed for carbopol and CMC.	Jump due to a transition in boundary conditions from no-slip for small bubbles in the Stokes regime to free surface conditions for larger bubbles
Calderbank et al. (1970)	Carbon dioxide bubbles in Polyox solutions	Yes	The bubble rear undergoes a shape change at the critical bubble volume
Leal et al. (1971)	Glass spheres and air bubbles in Polyacrylamide (PAA)	Yes, for air bubbles	Evidence for the hypothesis of Astarita and Apuzzo (1965)
Liu et al. (1995)	Polyox solutions	Yes	Reduction in drag due to the appearance of a cusped tail at a critical capillary number
De Kee et al. (1986)	CMC and PAA	No	
De Kee and Chhabra (1988)	Air, N ₂ , and CO ₂ bubbles in CMC, PAA (Separan AP30), and PAA with surfactants	No	
De Kee et al. (1990)	PAA (Separan AP30)	No	
Rodrigue et al. (1996)	CMC, Gellan gum, Polyethylene oxide, PAA with surfactants.	Yes, for PAA solutions only	Surface modification due to presence of surfactant and elastic forces
Rodrigue et al. (1996)	CMC, Gellan gum, Polyethylene oxide, PAA with surfactants.	Yes, for PAA solutions only	Surface modification due to presence of surfactant and elastic forces
Rodrigue and De Kee (1999)	PAA with added surfactant	Yes	Interfacial instability related to elasticity and surface tension gradients
Margaritis et al. (1999)	Various polysaccharides in solution.	No	
Dewsbury et al. (1999)	Air bubbles and buoyant particles in CMC	No	
Rodrigue and De Kee (2002)	Theoretical analysis of the free-surface problem	Yes	Discontinuity in surface forces. The existence of a cusp is a necessary but not sufficient condition for the occurrence of a discontinuity
Frank et al. (2003)	PAA	No	
Herrera-Velarde et al. (2003)	PAA, no surfactant	Yes. Bubble volume at discontinuity increased with polymer concentration.	Negative flow field around the bubbles appeared above the discontinuity
Funfschilling and Li (2006)	N ₂ bubbles in CMC and PAA solutions	No	
Soto et al. (2006)	Hydrophobically-modified associative polymer solutions.	Yes	Discontinuity results from a competition between elastic and surface tension forces
Kemiha et al. (2006)	PAA	No	Negative wake behind bubbles observed
Soto et al. (2006)	Hydrophobically-modified associative polymer solutions.	Yes	Discontinuity results from a competition between elastic and surface tension forces
Kemiha et al. (2006)	PAA	No	Negative wake behind bubbles observed
Pillapakkam et al. (2007)	Direct numerical simulations to study the role of viscoelasticity.	Yes. Magnitude of the jump varied with the concentration of solution	Shape of bubbles and wake structure changes at a critical volume
Malaga and Rallison (2007)	Numerical calculations of bubble deformation	No	
Pilz and Brenn (2007)	Praestol 2500 (PAA), polyethylene oxide, and Praestol 2540.	Yes. No discontinuity observed at low concentrations.	Relaxation time in elongational flow is important
Sikorski et al. (2009).	Carbopol	No	
Vélez-Cordero et al. (2012)	Boger-type fluids	Yes	Velocity discontinuity accompanied by formation of a small cusp at the rear of bubbles

2.3. Rheological Characterization of Complex Fluids

Fluid mechanics of incompressible liquids always allows one to split the stress tensor $\boldsymbol{\sigma}$ into an isotropic part associated with pressure p , and the generally anisotropic one, which is called the deviatoric stress tensor $\boldsymbol{\tau}$

$$\boldsymbol{\sigma} = -p\mathbf{I} + \boldsymbol{\tau} \quad (2.3.1)$$

where \mathbf{I} is the tensor unit (Batchelor 2002, Lamb 1959, Landau and Lifshitz 1987).

For Newtonian viscous fluids, such as water, the deviatoric stress tensor $\boldsymbol{\tau}$ is related to the strain-rate tensor \mathbf{D} with the rheological equation determined by a single rheological parameter, viscosity μ

$$\boldsymbol{\tau} = 2\mu\mathbf{D}, \quad \mathbf{D} = \frac{1}{2}(\nabla\mathbf{v} + \nabla\mathbf{v}^T) \quad (2.3.2)$$

where \mathbf{D} is the symmetric part of tensor gradient of velocity $\nabla\mathbf{v}$.

The constitutive equation of Newtonian liquids (2.3.2) is motivated by the fact that in simple shear experiments, the shear stress is found being linearly proportional to the shear rate γ , $\tau_{xy} = \mu\gamma$, while μ is a constant, i.e. the physical characteristic of a liquid.

However, gypsum slurries do not belong to the Newtonian fluids family. In simple-shear experiments they reveal a non-linear dependence of the shear stress on the shear rate, namely, $\tau_{xy} = K\gamma^n$, where two physical parameters of a fluid are involved: the consistency index K and the flow behavior index n (Sinha Ray et al. 2011). In particular, gypsum slurries possess $n < 1$, which makes them shear-thinning (or pseudoplastic). Introducing the effective shear viscosity of such fluids as $\mu_{sh} = \tau_{xy}/\gamma$, one finds that

$$\mu_{sh} = K\dot{\gamma}^{n-1} \quad (2.3.3)$$

Since $n < 1$, the shear viscosity of slurries decreases as the shear rate increases.

The three-dimensional generalization of Eq. (2.3) is given by the so-called Ostwald-de Waele, or the power-law rheological equation (Astarita and Marrucci 1974, Bird et al. 1987, Larson 1988)

$$\boldsymbol{\tau} = 2K \left[2\text{tr}(\mathbf{D}^2) \right]^{(n-1)/2} \mathbf{D} \quad (2.3.4)$$

When $n=1$ and $K=\mu$, Eq. (2.3.4) becomes the Newton-Stokes equation, the first Eq. (2.3.2).

Viscoelastic polymeric fluids also exhibit non-Newtonian behavior. The behavior is unusual in that sense that these fluids thicken under elongation and thin down under shear stress owing to the long-chain molecular structure. Viscoelastic fluids have the unique property of stress relaxation, i.e. possess memory effects. One of the common methods for the measurement of viscoelastic properties of polymeric fluids is to find the required time for stress relaxation. In this method, an experiment is performed whereby a constant shear deformation γ_0 is applied. It can be shown that the resulting stress decreases as a function of time. The shear modulus $G(t)$, which is sometimes referred to as the relaxation modulus, is defined as the ratio of the stress $\sigma(t)$ to the applied deformation γ_0 . By further incorporating the Maxwell model, which is appropriate to describe the stress relaxation, the shear modulus can be defined by

$$G(t) \equiv \frac{\sigma(t)}{\gamma_0} = G \exp(-t / \tau) \quad (2.3.5)$$

where τ is the relaxation time of the Maxwell model.

This variation of $G(t)$ with time depends on a multitude of factors, such as the degree of cross-linking, crystallinity of polymer and chain length. Figure 2.3.1 depicts the stress relaxation for a non-crosslinked viscoelastic material and a crosslinked rubbery material. The viscoelastic fluid

exhibits “fading memory” with the stress decreasing to zero, whereas the rubbery material relaxes to a stress of $\gamma_0 G_e$ where G_e is the rubber shear modulus. The effect of relaxation time on the variation of $G(t)$ with time is shown in Figure 2.3.2.

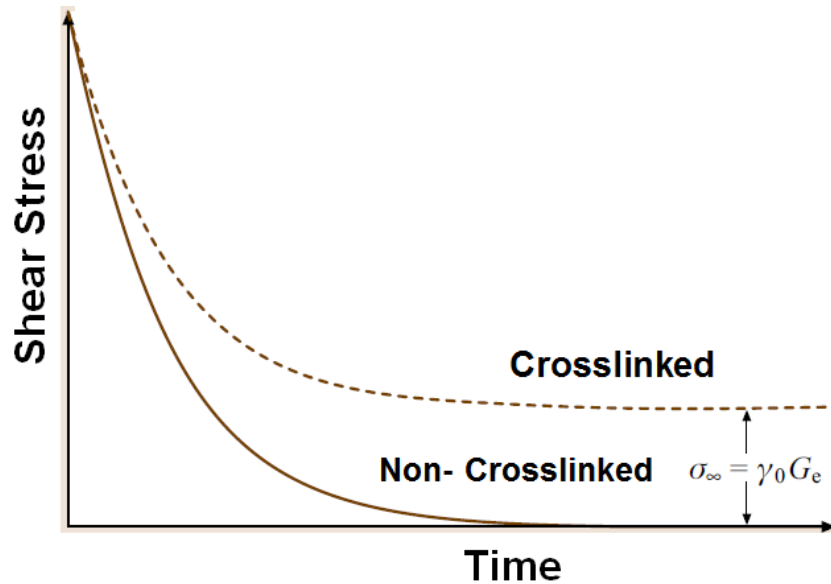


Figure 2.3.1. Stress relaxation for viscoelastic and rubbery materials (te Nijenhuis 2008).

From the Maxwell model, Eq. (2.3.5), it can be seen that $\sigma_{\text{red}} = \sigma(t)/\sigma_0 = \exp(-t/\tau)$ decreases sharply from 1 to 0 in the vicinity of $t = \tau$. Figure 2.3.2(a) shows the dependence of reduced relaxation modulus defined as $G_{\text{red}}(t) = G(t)/G = \sigma(t)/\sigma_0$ on $\log(\text{time})$ for two Maxwell models with $\tau = 1$ and $\tau = 10,000$ s. In general, the stress decrease is not as sharp as is shown in Figure 2.3.2(a). However, viscoelastic fluids typically have a mix of different chain lengths, which means that the relaxation time is not unique. This phenomena is described by the Maxwell-Wiechert model, Figure 2.3.2(b). In this model, the fluid structure is modelled as N

Maxwell elements linked in parallel, each with its own spring constant G_i and relaxation time τ_i for which the shear modulus is expressed as

$$G(t) = \sum_{i=1}^N G_i \exp(-t / \tau_i) \quad (2.3.6)$$

The greater the number of the Maxwell elements the greater is the accuracy in the description of the viscoelastic behavior, Figure 2.3.2(b).

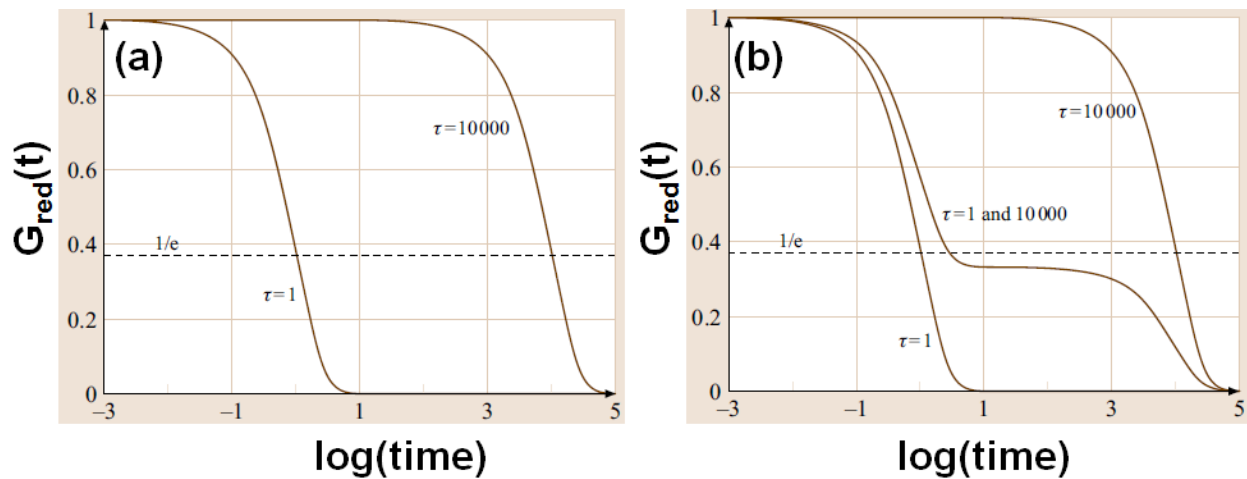


Fig. 2.3.2. (a) Semi-logarithmic plot of the reduced relaxation modulus $G_{red}(t) = G(t)/G = \sigma(t)/\sigma_0$ for two Maxwell elements, with relaxation times of 1 s and 10,000 s, respectively. (b) Semi-logarithmic plot of the relaxation of the reduced stress σ/σ_0 for the Maxwell-Wiechert model, with relaxation times of 1 s and 10,000 s and spring constants G_1 and $G_2 = 0.5G_1$; the results of (a) are also shown (te Nijenhuis 2008).

In addition to stress relaxation, another important feature of viscoelastic fluids is creep. The creep behavior of viscoelastic fluids can be more accurately depicted by utilizing the Burgers model which links the Maxwell model with a Kelvin-Voigt model in series. Following the

Burgers model, a viscoelastic fluid subjected to a constant stress σ_0 exhibits strain $\gamma(t)$ following the expression

$$\gamma(t) = \sigma_0 J(t) \quad (2.3.7)$$

where the time dependence is given by

$$J(t) = J + J_1 [1 - \exp(-t/\tau_1)] + \frac{1}{\eta} \quad (2.3.8)$$

and the compliance of the two springs and retardation time are given, respectively, as

$$J = \frac{1}{G} \quad (2.3.9)$$

$$J_1 = \frac{1}{G_1} \quad (2.3.10)$$

$$\tau_1 = \frac{\eta_1}{G_1} \quad (2.3.11)$$

The discussion above elucidates different properties of non-Newtonian fluids that need to be measured under shear and elongation. For the shear flow measurement, to elucidate the viscoelastic properties of non-Newtonian fluids, several different geometric shapes are used in shear rheometers. Some of the common shapes and the corresponding geometric factors are listed in Table 2.3.1.

Table 2.3.1. Basic geometric shape factors.

Geometry	Geometric Shape Factor
sandwich construction	A/d
cone and plate	$2\pi R^3 / (3\Delta\Theta)$
parallel plates	$\pi R^4 / d$
torsion of a bar with rectangular cross-section	$cd^3 f(c/d) / (16L)$ for $c/d > 1$
torsion of a bar with circular cross-section	$\pi R^4 / (2L)$
rotation between concentric cylinders	$4\pi L r_i^2 r_o^2 / (r_o^2 - r_i^2)$

where

A = area of sample in contact with plane

d = thickness of sample or torsion bar

c = width of torsion bar

$f(c/d)$ = function of c/d with values ranging between 2.25 and 5.33

L = height of cylinder or bar

R = radius of bar or plate

r_i = radius of inner cylinder

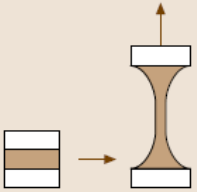
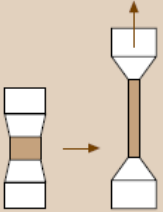
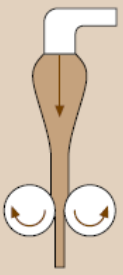
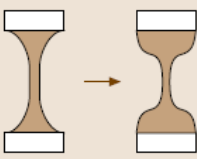
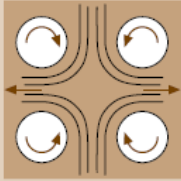
r_o = radius of outer cylinder

$\Delta\Theta$ = small angle between cone and plate

Practical processing of non-Newtonian materials usually involves a combination of shear and extensional flows. The normally large strain rates typified in extensional flow can result in highly non-Newtonian strain and strain rate responses. These dependencies are not sufficiently

described by shear measurements alone and require the extensional flow behavior to be elucidated. Therefore, there is a significant research aim focusing on the extensional flows and extensional rheometers. Development of the extensional measurement instrumentation for polymeric fluids has been impeded by the difficulty of creating a homogeneous extensional flow due to two challenges. First, creating flow over a solid surface generates a shear stress which corrupts the flow field. This can be circumvented by involving deformation in air or a low viscosity outer fluid. Second, the high levels of strain required to stretch the polymer chains sufficiently necessitates a motion apparatus capable of a relatively large travel distance and dynamic velocity range, while providing sensitive position control. These challenges have necessitated distinct extensional rheometer designs tailored to particular polymeric fluid viscosity. These are shown in Table 2.3.2 following McKinley (2008).

Table 2.3.2. Summary of extensional rheometer designs and application ranges.

Instrument type	Geometry	Flow	Shear viscosity range [Pa s]	Limitations
Filament stretching, constant volume, medium viscosity		Uniaxial extension, constant strain rate	1–1000	Sample gripping, limited to medium with high viscosity, elastic instability
Filament stretching, constant volume, high viscosity		Uniaxial extension, constant strain rate	> 1000	Limited to low strain rates, temperature control
Filament stretching, constant length, high viscosity		Uniaxial extension, constant strain rate	> 1000	Limited to low strain rates, temperature control
Fiber spinning		Uniaxial extension	> 1	Low strain, non-uniform strain rates, pre-shear history
Capillary breakup rheometry		Uniaxial extension	0.01 – 1	Inertial and surface tension dominate at low end of viscosity, variable strain rates
Four-roll mill		Uniaxial extension	1–1000	Variable strain rates and strain histories

One of the widely used methods is capillary breakup rheometer applied to study dilute and semi-dilute polymer solutions. Because of its wider applicability, in particular, to gypsum slurries, this approach is briefly discussed next. Stretching a non-Newtonian fluid in a capillary breakup rheometer causes the fluid thread diameter $D(t)$ to thin as (Yarin et al., 2004; Zussman et al., 2007)

$$D(t) = D_0 e^{-t/3\lambda} \quad (2.3.12)$$

where D_0 is the thread diameter after the initial stretch at time $t = 0$, and λ is the relaxation time. This is a typical viscoelastic behavior, which can be followed by the Newtonian one (or just correspond to a Newtonian fluid)

$$D(t) = D_0 - \frac{\sigma}{\mu_{el,t}} t \quad (2.3.13)$$

where σ is the surface tension of the fluid and $\mu_{el,t}$ is the final extensional viscosity.

Other common properties of non-Newtonian fluids include thixotropy, rheopexy and yield stress which can be described as follows. Thixotropy is a characteristic of certain fluids which are gel-like at rest and upon stirring or shaking become more liquefied, and then return to the gel-like state when allowed to remain at rest. This behavior is reversible and higher thixotropic materials become even thinner when sheared. Furthermore, the thixotropic fluids viscosity is higher when at rest and is lessened when stressed. Rheopexy is the exactly opposite effect to thixotropy and is referred to as anti-thixotropy.

According to Barnes (2008), thixotropy is a reversible, time-dependent process where there is a reduction in the apparent viscosity when fluid is subjected to a constant shear rate or shear stress, which then slowly recovers when the shear rate or shear stress is removed. This occurs because of the finite time required for a shear change in the fluid microstructure to take place. A

schematic of the process is shown in the inset of Figure 2.3.3. This results in variation in viscosity during the flow process, as is shown in Fig. 2.3.3. The competition between the flow-induced collisions and stress separation of particles brings the microstructure to a new equilibrium position in a relatively short time. When the flow stops, Brownian motion directs the microstructure particles to more accommodating positions, thus rebuilding the microstructure but in a more time-consuming fashion. Thixotropy reflects the finite time it takes to move from one state of the fluid microstructure to another, and then back again.

It is interesting to note that thixotropic characteristics have been intentionally built into many common commercial products where shear-thinning during application of material is desired, such as paint and wallboard joint treatment.

An understanding of these types of complex rheological behavior can be gained by considering the following explanation. Realizing that all fluids with microstructure can exhibit thixotropy, the driving force for the microstructure change results from the competition in flow stresses between the flow-induced collisions causing breakdown, build-up tension due to the flow congestion and the random thermal agitation of particles due to Brownian motion. This competition eventually moves the particles to a more favorable position. This all works to establish the level of elasticity and viscosity. In polymer fluids when the entanglement density is very high and macromolecular alignment is most random, maximum microstructure order is observed which generally results in higher viscosity and elasticity.

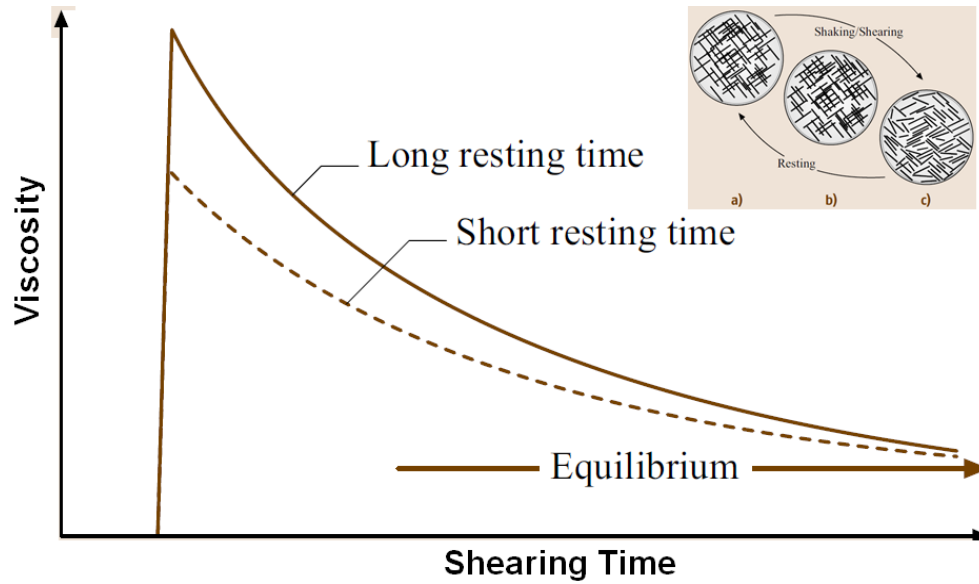


Figure 2.3.3. Shearing a thixotropic liquid after short and long rest times. The inset shows breakdown of an idealized two-dimensional (2D) thixotropic system: (a) completely structured - giving elastic, solid-like behavior; (b) partly structured - giving a viscoelastic response; and (c) completely unstructured - giving a viscous, shear-thinning response (Barnes 2008).

To describe the behavior of these fluids, the change in viscosity can be characterized by the “stretched-exponential” model shown as in Eq. (2.3.14). It makes the simplifying assumption of step change from steady state conditions (Maestro et al., 2002).

$$\eta = \eta_{e,\infty} + (\eta_{e,0} - \eta_{e,\infty}) \left(1 - e^{-\left(\frac{t}{\tau}\right)^r} \right) \quad (2.3.14)$$

where $\eta_{e,0}$ is the initial viscosity when shearing begins, $\eta_{e,\infty}$ is the final viscosity after a very long time, τ is a time constant and r is a dimensionless constant.

This equation can describe both build up and break down in steps dependent on the direction and level of τ and r .

For fluids having a yield stress, the following equation can be used to describe the rebuilding of the shear stress.

$$\sigma_y(t) = \sigma_{y,0} + [\sigma_{y,\infty} - \sigma_{y,0}] \left(1 - e^{-\frac{t}{\tau}}\right) \quad (2.3.15)$$

It can be shown that shear can not only break down or build up particles but also change the internal morphology. Following an extended shearing, loosely packed particles become tightly packed and monodispersed indicating a loss of structure.

From the practical standpoint, most time-dependent microstructure-based theoretical approaches are difficult to attain because the properties of the microstructure elements are widely varied and difficult to measure. Because of this, semi-empirical phenomenological approaches have been developed to characterize such fluids. Some of the widely used semi-empirical models are discussed next.

These so-called “ Indirect Microstructural Theories” (Godfrey et al., 1983; Goodeve et al., 1938; Moore et al., 1959; Cheng et al., 1965; Allesandrini et al., 1982; Baravian et al., 1996) are built around a numerical scalar measure of structure usually referred to by λ where $\lambda = 1$ is a completely built up structure and $\lambda = 0$ represents a completely broken down structure. For a typical non-Newtonian fluid, $\lambda = 1$ relates to zero shear viscosity η_0 and $\lambda = 0$ relates to an infinite shear rate η_∞ . Thixotropy

evolves through the time derivative of the structure measure, $d\lambda/dt$, defined as $g(\dot{\gamma}, \lambda)$. It can be

shown that

$$g(\dot{\gamma}, \lambda) = a(1-\lambda)^b - c\lambda\dot{\gamma}^d \quad (2.3.16)$$

where a , b , c are constants for a particular system. If $g(\dot{\gamma}, \lambda)$ is negative, the system is breaking down to equilibrium, whereas if it is positive the system is building up. When equilibrium is reached, setting $d\lambda/dt = 0$ enables finding the corresponding value of λ at each shear rate. The parameter λ is then related to the stress σ or the viscosity η . A convenient way to achieve this is through the Bingham equation which is the simplest possible expression

$$\sigma = \sigma_y + k \dot{\gamma} \quad (2.3.17)$$

Note that if there is no yield stress σ_y present, then

$$\sigma = k \dot{\gamma} \quad (2.3.18)$$

which is a variant of a Newtonian fluid.

Another approach to describe the relationship between viscosity and the fluid structure is given by de Kee et al., (1983) and Tiu et al. (1974). Here they depict the breakdown characteristics for several food material types through the relationship (Kee et al., 1983; Tiu et al., 1974)

$$\frac{d\lambda}{dt} = -c \dot{\gamma}^d (\lambda - \lambda_{\text{equil}})^n \quad (2.3.19)$$

where c is a constant.

The stress can then be established using a multiple exponential type flow law

$$\sigma(\dot{\gamma}) = \lambda \left[\sigma_0 + \dot{\gamma} \sum_i \eta_i \exp(-t_i \dot{\gamma}) \right] \quad (2.3.20)$$

where η_i and t_i are the parameters for the system. This theory is used to describe the viscosity decay curves.

In addition, J. Mewis and J. Schryvers (1996) derived a model that does not require any parameter such as λ but rather utilizes viscosity as the direct measure of the fluid structure. The rate of change of viscosity instead of the rate of change of the structure is used as the viscosity difference between the current value and the steady-state viscosity. Hence, it was shown that

$$\frac{d\eta}{dt} = K \left[\eta_s \left(\frac{\dot{\gamma}}{\gamma} \right) - \eta \right]^n \quad (2.3.21)$$

where η_s is the steady state viscosity and K and n are constants. This equation is then integrated to obtain

$$\eta = \eta_{e,\infty} - (\eta_{e,\infty} - \eta_{e,0}) \times \left\{ \left[(\eta - 1) K t (\eta_{e,\infty} - \eta_{e,0})^{n-1} + 1 \right]^{n-1} + 1 \right\}^{1/(1-n)} \quad (2.3.22)$$

In the subscripts for η , e refers to equilibrium state, while the second subscript refers to the shear rate at 0 and ∞ .

The present thesis work focuses on the interaction of gypsum slurry with foam. The knowledge of the rheological characteristics of gypsum slurry and foam is extremely important in explaining this interaction. In Yarin et al. (2004), Zussman et al. (2007), Tiwari et. al. (2009) and Sinha-Ray et al. (2011) rheological behavior of non-Newtonian materials, including gypsum slurries, has been studied under shear and elongation conditions. It needs to be mentioned that during processing of wallboard gypsum slurry is conveyed through various flow configurations which can be either shear or elongational in nature or a mix of both. So a unified model explaining all the flow configurations was in focus. Sinha-Ray et al. (2011) have shown that gypsum slurry can be accurately described using the power-law model. The following approach was adopted by Sinha-Ray et al. (2011). For a uniaxial elongational flow within a liquid thread experiencing self-thinning due to surface tension, as shown in Figure 2.3.4, the axial strain rate is

described via the longitudinal velocity gradient, $\partial V / \partial x > 0$, where $V = 0$ at the stagnation point 0, where $x = 0$. This flow is accurately described using the quasi-one-dimensional model in the axial direction, x , where $V = V(x, t)$. The self-thinning of the thread is expressed through the quasi-one-dimensional continuity equation (2.3.23) and the momentum balance equation (2.3.24) according to Yarin (1993, p. 73; Yarin et. al., 2004)

$$\frac{\partial a^2}{\partial t} + \frac{\partial V a^2}{\partial x} = 0 \quad (2.3.23)$$

$$\frac{\partial}{\partial x} \left[\sigma_{xx} a^2 + 2\alpha a \left\{ 1 + \left(\frac{\partial a}{\partial x} \right)^2 \right\}^{1/2} \right] = 0 \quad (2.3.24)$$

where a is the thread radius, σ_{xx} is the normal stress in thread, and α is the fluid surface tension coefficient. Note that since the flow is primarily influenced by the internal stress, the inertial forces can be neglected in the momentum balance equation.

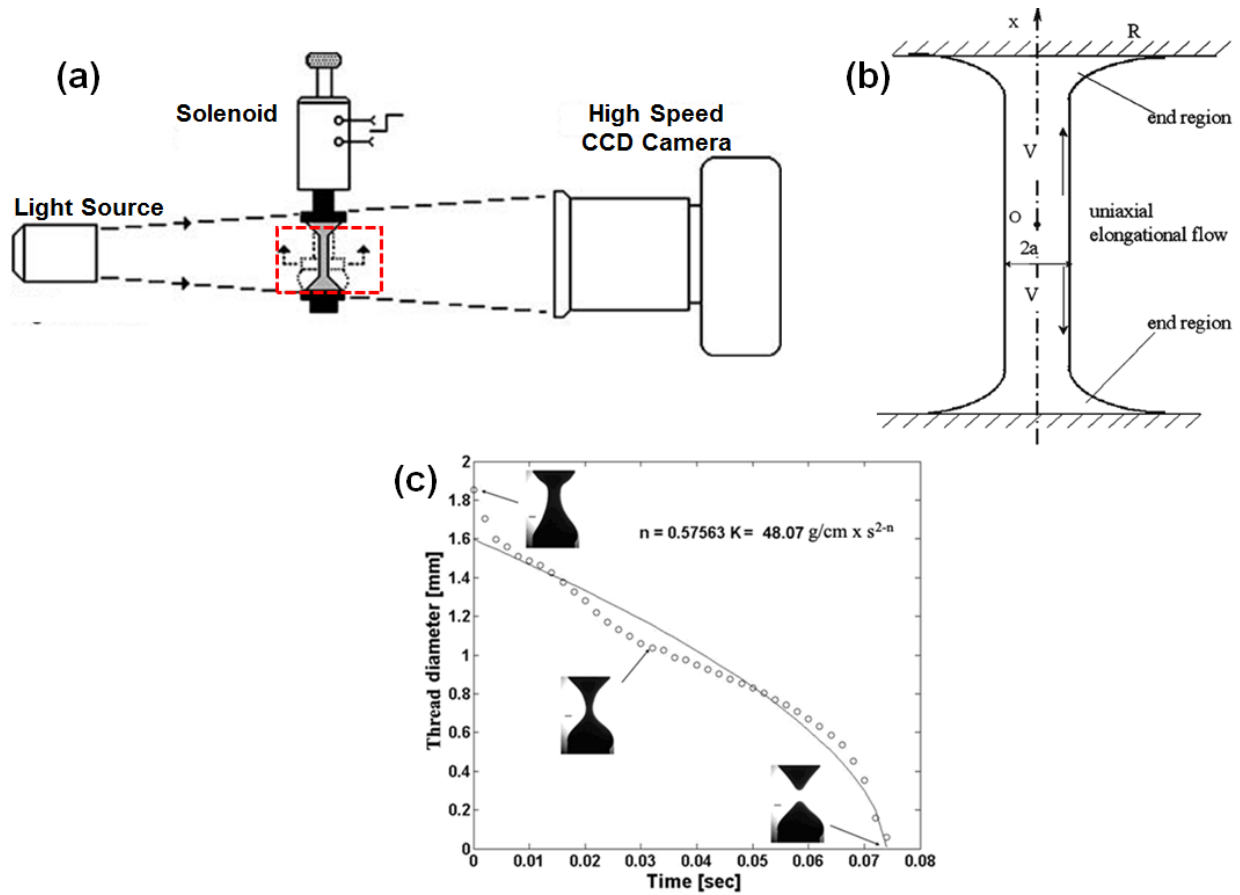


Figure 2.3.4. (a.) Schematic of Elongation Rheometer. (b) Self-thinning of a cylindrical liquid thread, driven by surface tension, namely, by the pressure gradient $\alpha/a > \alpha/R$. (c) Example of the evolution of a self-thinning gypsum thread. In the insets, the snapshots of the gypsum thread in the Elongation Rheometer are shown. (Sinha-Ray 2011).

The experimental procedure consists of suspending a droplet between two closely spaced plates and then at $t = 0$, and quickly separating them to approximately 1 cm, producing a liquid thread as shown in Figure 2.3.4. Since liquid wets the end plates, the radius of the thread in the end region R is much larger than in the middle of the thread. The capillary pressure in the middle area, α/a , is much higher than near the ends, α/R . Accordingly, the capillary pressure gradient squeezes the fluid toward the end plates. Assuming the thread to be uniform, $\partial a/\partial x = 0$,

enables one to derive the strain rate at the centerline in conjunction with the continuity equation (2.3.23) as follows

$$\gamma = \frac{\partial V}{\partial x} = -\frac{2}{a} \frac{da}{dt} \quad (2.3.25)$$

It can be shown that for a power-law fluid the diameter of the thread, d , thins down according to the following equation

$$d = d_0 \left(\frac{t_s - t}{t_s} \right)^n \left(\frac{t_s^n}{d_0 k} \right)^{\frac{1}{3^{(n-1)/2}}} \frac{1}{6n(1+\beta_1)} \quad (2.3.26)$$

From the elongation and shear experiments the rheological parameters of the power law, k and n , found for gypsum slurries become practically identical (Sinha-Ray et al. 2011). Therefore, the power-law model is applicable for gypsum slurries irrespective of the flow situation. Accordingly, in the present dissertation the power law model is employed to describe the rheological characteristics of gypsum slurries.

However, as previously mentioned foam is mixed with gypsum slurry to reduce the weight of gypsum wallboard. In order to numerically simulate practically relevant gypsum slurry flow operations it is extremely important to characterize the rheological properties of foamed gypsum slurry. Jun (2013) studied in his thesis the rheological characteristics of foamed gypsum slurry at different water stucco ratios (WSR). His results can be summarized as follows. The power-law model is still applicable to describe the rheological behavior of foamed gypsum slurries. The resulting values of K and n for different foam content were fitted using the polynomial function. Such fitting is shown in Figure 2.3.5. In the present dissertation, these rheological parameters and functions) are employed in the numerical simulations (cf. Section 3.6).

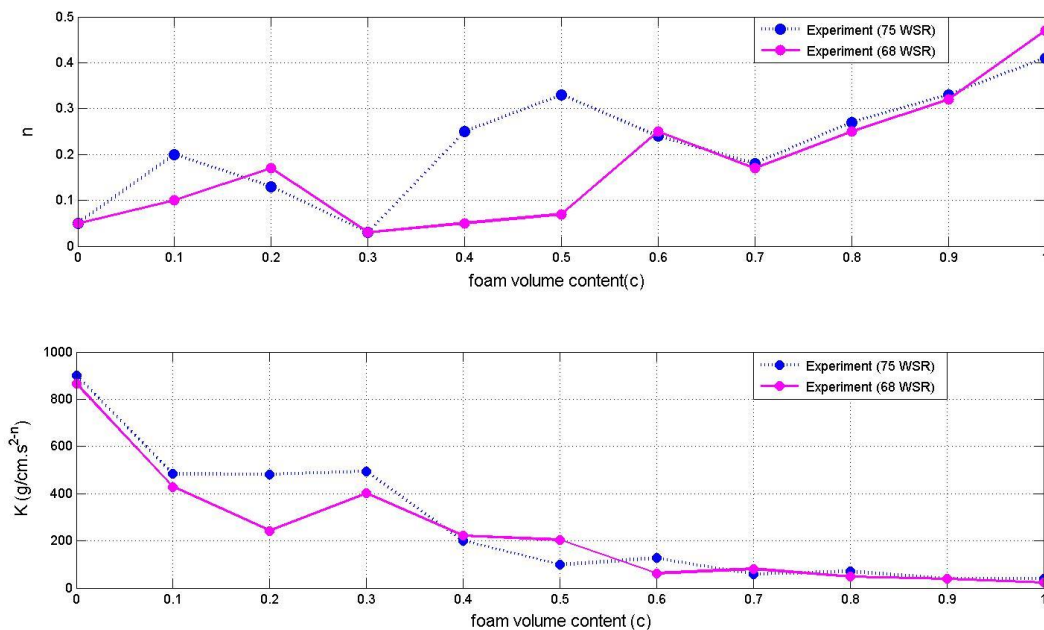


Figure 2.3.5. Experimental values of K and n for foamed gypsum at 68 and 75 WSR with different foam contents. The experimental values are fitted using a polynomial function. (Jun 2013).

2.4. Non-Newtonian Fluid Jets

Significant research efforts aimed the evolution of jet and/or spray in uniform cross-flow from the internal combustion engines point of view. A very detailed review has been published by No et al. (2015). A typical evolution of a jet profile is shown in Figure 2.4.1. In such flow, the mixing of an injected fluid into the fluid flowing in a cross-flow direction depends on the column and surface breakup, penetration height, droplet breakup, jet dispersion and ligament formation. However, the jet evolution profile prediction is mostly empirical in nature. Various functional forms are used to describe the jet profile, namely- the power law, exponential, logarithmic, etc. However, most of these studies suffer from discrepancies owing to the experimental inaccuracies, inaccuracies of the measurement techniques, or the assumptions made during the

modeling. The situation becomes even more complicated, when the injected fluid is non-Newtonian in nature.

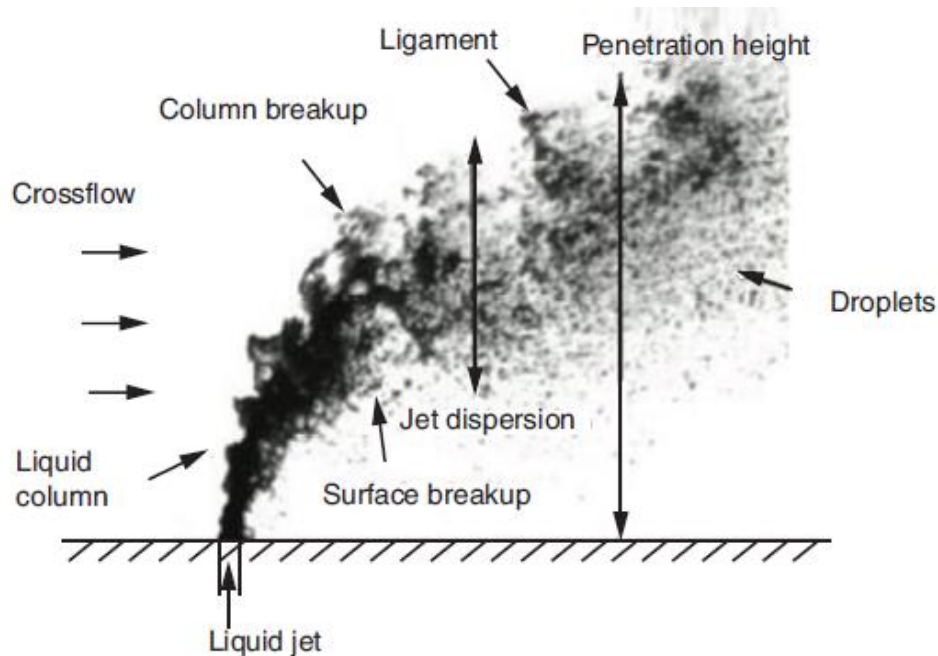


Figure 2.4.1. Evolution of jet profile in cross-flow [Obtained with permission from No et al. (2015)]

In Muñoz-Esparza et al. (2012) the authors numerically investigated the interaction of impinging jets with deformable liquid layers. In order to do so, they utilized the volume of fluid (VOF) method to deal with multiphase flows. The turbulence was modeled using the $k-\epsilon$ model. However, no non-Newtonian behavior of the interacting fluids was studied. The authors studied the deformation of water owing to the impingement by air. In addition to that, although the authors could closely reproduce the experimental results, the computations were prohibitively

time-consuming. It can be expected that the complexity will increase manifold if the interacting fluids were non-Newtonian in nature.

A few early analytical and experimental works on submerged non-Newtonian jets can be found in the following references (Mitwally et al., 1978; Kapur et al., 1962; Gutfinger et al., 1962; Serth et al., 1972; Kumar et al., 1984). Mitwally et al. (1978) in their numerical analysis of laminar power-law fluid flows predicted that if the behavior index $0.5 < n < 1$, the jet will remain laminar over its entire length. However, it is expected that for a submerged laminar jet, owing to the Reynolds number at the exit, the jet may remain laminar or turn into a laminar/turbulent jet. Various regions of such a laminar-turbulent submerged jet are shown in Figure 2.4.2 (Kumar et al., 1984). In the experimental work described in Kumar et al. (1984) the authors showed that the length of the laminar is not affected by the non-Newtonian nature of the fluid for $600 < Re < 1100$. The authors also found that for this range of the Reynolds number there is not much difference in the laminar jet length between the Newtonian and non-Newtonian fluids. However, for $50 < Re < 200$, the laminar length depends on the non-Newtonian nature of the fluid.

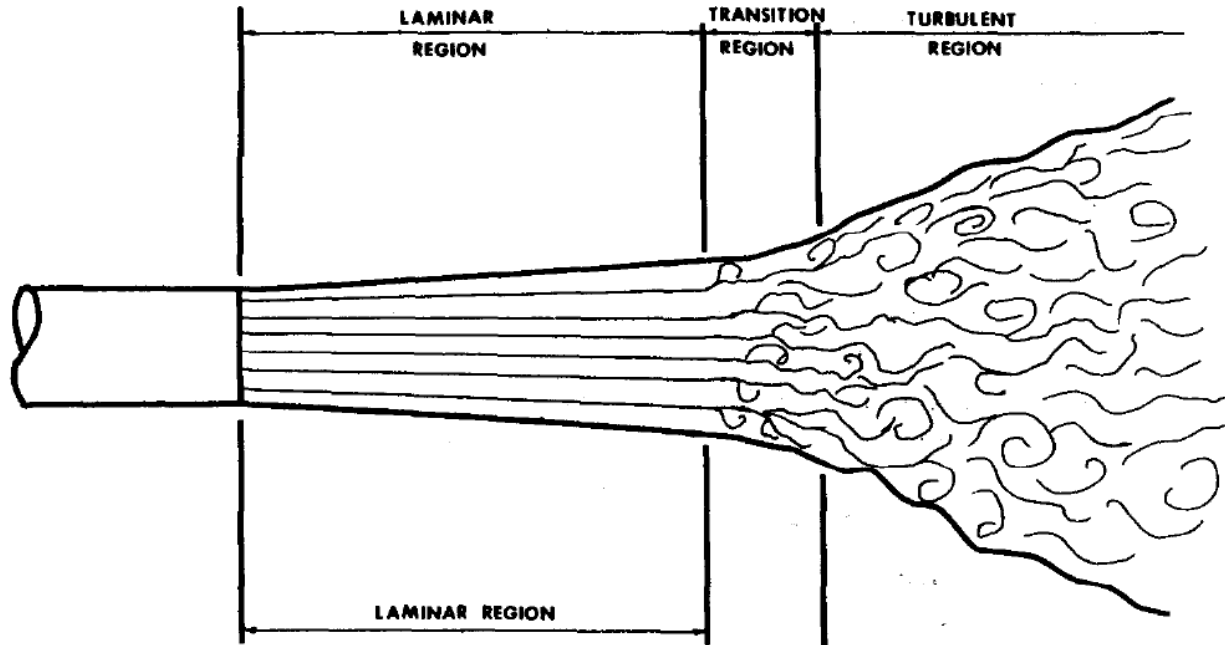


Figure 2.4.2 The evolution of laminar-turbulent jet profile (from Kumar et al.1984).

Filip et al. (1991) have studied the similarity solution for laminar wall jets of power-law fluids on axisymmetric bodies. Wei et al (2014) studied the boundary layer flow for the power-law fluids. They found that the power-law index has a significant effect on the similarity solution. They found that the solution has a positive curvature for $0 < n \leq 1$, whereas for $n > 1$ the solution has a negative curvature. Jordan et al. (1992) studied the evolution of an axisymmetric, laminar submerged polymer jet. The laminar jet was formed by forcing Separan AP30 (the polymer solution) in a large chamber filled with water. The velocity profile was measured using a laser-Doppler anemometer. They further studied the effect of polymer concentration on the jet profile. In their study, they found that the centerline velocity decay and jet spread was not affected greatly by the polymer concentration. For the numerical study, the authors used two different rheological models- (a) the power-law model and (b) the power series

viscosity model. It needs to be mentioned that none of these models capture the viscoelastic nature of the polymer solution. As a result of which, although they could predict the centerline jet velocity, the jet spread could not be predicted accurately. Pavlov (1979) studied the theory of a flat submerged jet of a power-law fluid. Bubnov (1968) also studied numerically the evolution of a submerged jet in a power-law fluid. Hammad (2013) studied the characteristics of velocity and momentum decay in a submerged viscoplastic jet numerically. The rheological model used in this work was the Bingham rheological model. In this work, two different jet profiles – (a) a fully developed pipe jet and (b) a top hat jet profile were studied for the Reynolds numbers of 50, 100 and 200 and for three different yield stresses. It was found that the decrease in the centerline velocity was more rapid for the pipe jet in comparison to the top hat jet. It was also found that the yield stress has a significant effect on the velocity and momentum depths of the submerged jet.

As it was mentioned in the previous subsection, both gypsum slurry and the foam used in wallboard manufacturing are the power-law fluids. However, in the literature survey it was found that there is a lack of reported research work dealing with the dynamics of mixing a foam jet with gypsum slurry. It should to be mentioned that apart from the industrial importance this problem is scientifically intriguing owing to: (a) the massive length scale of operation, and (b) the interaction of the power-law fluids coupled with mass transfer under laminar or turbulent conditions. This thesis aims to bridge this gap by providing a theoretical and numerical framework based on the correct rheological model. It also needs to be mentioned that one of the key aspects of this work is to reduce the computational power required to perform the theoretical analysis. This will help to extend the numerical simulation to an industrial-scale operation. In particular, Chapter 3 outlines the basic structure of the numerical analysis. It also describes the

coordinate transformation scheme used in the numerical code. Chapter 4 describes the base case of a single jet of foam injected into an infinite pool of stagnant gypsum slurry. Chapter 5 tackles the more realistic case of a foam jet injected into a gypsum slurry moving in a direction perpendicular to the impinging foam jet.

3. STRAIGHT FOAM JET INJECTED INTO SLURRY: PROBLEM FORMULATION

3.1. Governing Equations for the Boundary Layer of the Power-Law Two-Phase Matter

To describe the development of an axisymmetric straight submerged jet of foam released into space filled with gypsum slurry and evaluate the mixing rate and uniformity of the resulting mixture, we apply the boundary layer theory of jets (Schlichting 1968).

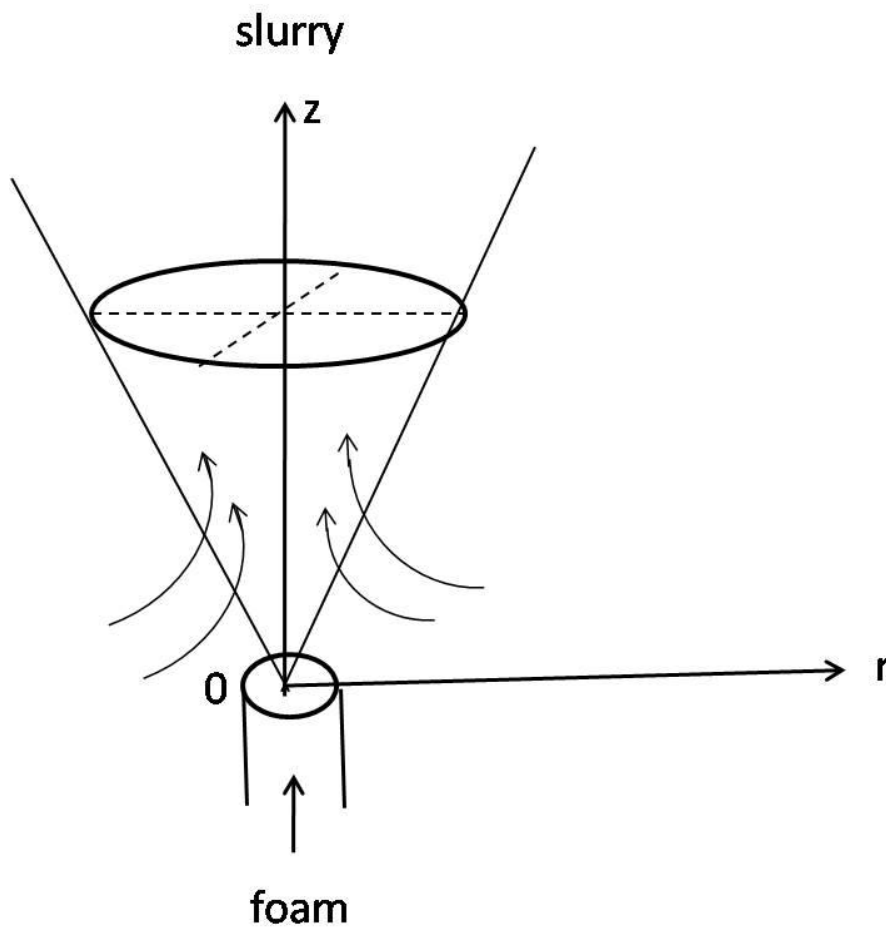


Figure 3.1.1. Sketch of axisymmetric submerged jet of foam issued into slurry.

A steady-state laminar flow with constant pressure and no-cross flow is assumed and the governing equations are formulated. Consider the continuity equation, which reads:

$$\frac{\partial}{\partial r}(\rho r v_r) + \frac{\partial}{\partial z}(\rho r v_z) = 0 \quad (3.1.1)$$

where v_r and v_z are the radial and longitudinal velocity components, $\rho = \rho(\phi)$ is the density of mixture which is a function of the air fraction ϕ where in particular, $\phi = 1$ for pure air and $\phi = 0$ for pure slurry.

The longitudinal (axial) momentum balance equation reads:

$$\rho \left(v_r \frac{\partial v_z}{\partial r} + v_z \frac{\partial v_z}{\partial z} \right) = \frac{1}{r} \frac{\partial}{\partial r} \left(\mu r \frac{\partial v}{\partial r} \right) \quad (3.1.2)$$

where the viscosity $\mu = \mu(\phi)$ is given by the following expression dictated by the rheological constitutive equation (see Section 3.6 below)

$$\mu = K(\phi) \left[\left| \frac{\partial v_z}{\partial r} \right| \right]^{n(\phi)-1} \quad (3.1.3)$$

The foam diffusion equation in the boundary layer approximation is expressed as:

$$\rho \left(v_r \frac{\partial \phi}{\partial r} + v_z \frac{\partial \phi}{\partial z} \right) = \frac{1}{r} \frac{\partial}{\partial r} \left(\rho D r \frac{\partial \phi}{\partial r} \right) \quad (3.1.4)$$

where D is the diffusion coefficient of air in the slurry.

3.2. The Boundary Conditions

Consider the following sketch of the exit conditions at the nozzle

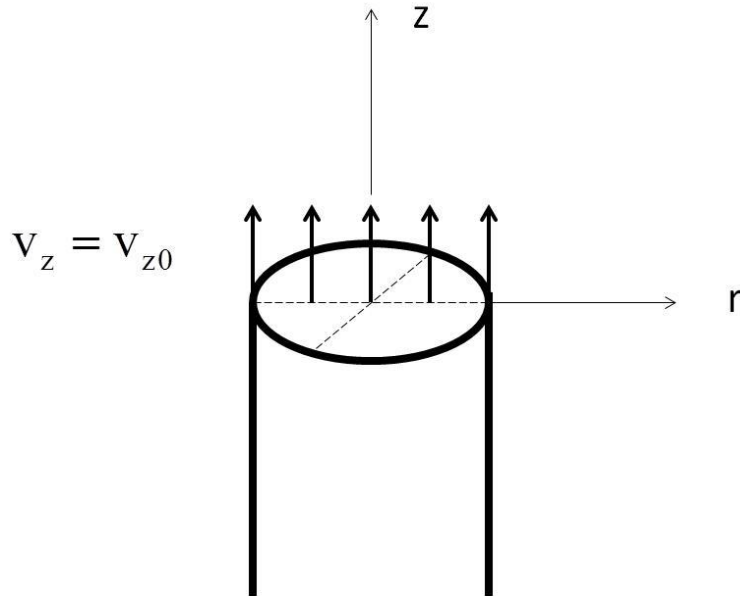


Figure 3.2.1. Nozzle exit conditions.

The boundary conditions are imposed in the cylindrical coordinates given the geometry of the problem. At the nozzle exit $z = 0$ the initial velocity and foam concentration are given

$$v_r = 0 ; v_z = v_{z0} ; \phi = \phi_0 . \quad (3.2.1)$$

At the jet axis $r = 0$ the standard profile smoothness/function finiteness conditions are imposed

$$\frac{\partial v_r}{\partial r} = \frac{\partial v_z}{\partial r} = \frac{\partial \phi}{\partial r} = 0 \Leftrightarrow v_r, v_z, \phi < \infty . \quad (3.2.2)$$

Furthermore, at the asymptotically far edge of the jet $r = \infty$ slurry is at rest and no air is present, which means that

$$v_r = 0; \quad v_z = 0; \quad \text{and} \quad \phi = 0. \quad (3.2.3)$$

This implies that at $r = \infty$, since the longitudinal velocity is a constant (zero), also

$$\frac{\partial v_z}{\partial r} = 0 \quad (3.2.4)$$

as well as because air concentration at infinity is constant (zero), also

$$\frac{\partial \phi}{\partial r} = 0. \quad (3.2.5)$$

The boundary conditions (3.2.2)-(3.2.5) can be visualized in the form of the sketch in Figure 3.2.2. Note also, that these boundary conditions exclude the unphysical profiles sketched in Figure 3.2.3.

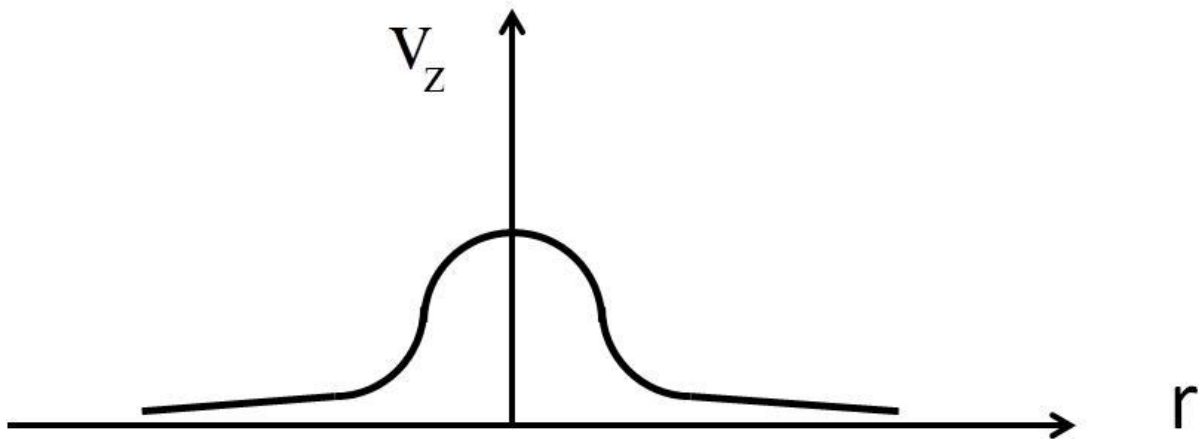


Figure 3.2.2. Velocity boundary conditions.

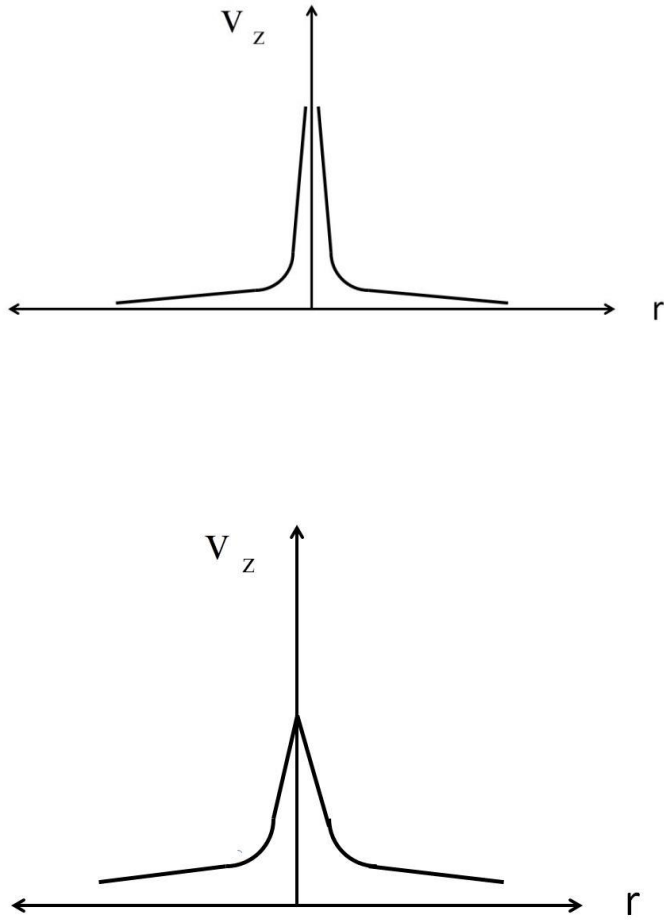


Figure 3.2.3. The unphysical velocity profiles excluded by the boundary conditions (3.2.2).

3.3. The Integral Invariants

The problem formulated in section 3.2 has two integral invariants. The first one is associated with the momentum balance equation, and reads

$$2\pi \int_0^{\infty} r \rho v_z^2 dr = \text{Constant} \quad (3.3.1)$$

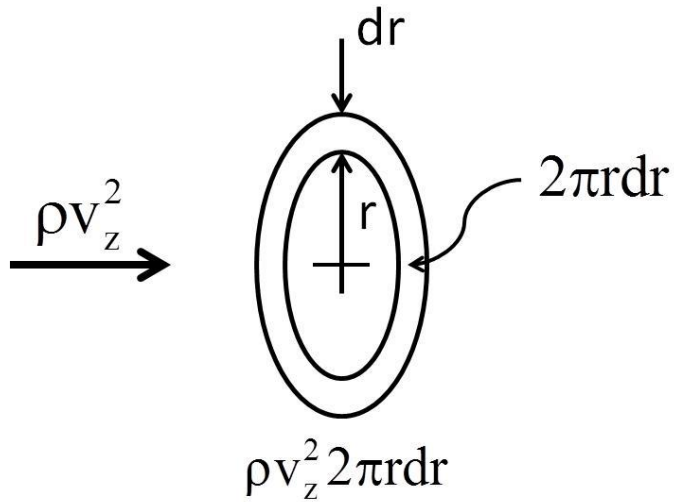


Figure 3.3.1. Sketch of the axial momentum flux in jet.

The invariant (3.3.1) means that the longitudinal momentum flux is constant along the jet, and is illustrated by the sketch in Figure 3.3.1.

The second integral invariant is associated with the foam diffusion equation. It reads

$$2\pi \int_0^{\infty} \rho \phi v_z r dr = \text{Constant} = \eta_0 2\pi \quad (3.3.2)$$

where η_0 is defined as

$$\eta_0 = \int_0^{\infty} \rho \phi v_z r dr. \quad (3.3.3)$$

The second invariant means that the mass flux of foam is constant along the jet.

These integral invariants are obtained from the governing equations and the boundary conditions along the following lines [as an example, the momentum balance equation (3.1.2) is used].

Multiplying Eq. (3.1.2) by r results in the following equation

$$\rho v_r \frac{\partial v_z}{\partial r} + \rho v_z \frac{\partial v_z}{\partial z} = \frac{\partial}{\partial r} \left(\mu r \frac{\partial v_z}{\partial r} \right). \quad (3.3.4)$$

We apply the chain rule of differential calculus to the first two terms of Eq. (3.3.2) which will enable us to develop terms that will eventually simplify the equation.

The first term on the left-hand side in Eq. (3.3.4) is transformed using the chain rule in the following manner

$$\rho v_r \frac{\partial v_z}{\partial r} = \frac{\partial(\rho v_r v_z)}{\partial r} - v_z \frac{\partial(\rho v_r)}{\partial r}. \quad (3.3.5)$$

In a similar manner the second term on the left-hand side in Eq. (3.3.4) is transformed to the following form

$$\rho v_z \frac{\partial v_z}{\partial z} = \frac{\partial(\rho v_z^2)}{\partial z} - v_z \frac{\partial(\rho v_z)}{\partial z}. \quad (3.3.6)$$

Substituting Eqs. (3.3.5) and (3.3.6) into Eq. (3.3.4) results in the following equation

$$\frac{\partial(\rho v_r v_z)}{\partial r} - v_z \frac{\partial(\rho v_r)}{\partial r} + \frac{\partial(\rho v_z^2)}{\partial z} - v_z \frac{\partial(\rho v_z)}{\partial z} = \frac{\partial}{\partial r} \left(\mu r \frac{\partial v_z}{\partial r} \right) \quad (3.3.7)$$

which transforms to the following form

$$\frac{\partial \rho v_r v_z}{\partial r} + \frac{\partial \rho v_z^2}{\partial z} - v_z \left[\frac{\partial (\rho v_r)}{\partial r} + \frac{\partial (\rho v_z)}{\partial z} \right] = \frac{\partial}{\partial r} \left(\mu r \frac{\partial v_z}{\partial r} \right). \quad (3.3.8)$$

However, according to the continuity Eq. (3.1.1), the third term on the left-hand side in Eq. (3.3.8) vanishes and the remaining terms yields the momentum equation in the following, so-called divergent form

$$\frac{\partial}{\partial r} (\rho v_r v_z) + \frac{\partial}{\partial z} (\rho v_z^2) = \frac{\partial}{\partial r} \left(\mu r \frac{\partial v_z}{\partial r} \right). \quad (3.3.9)$$

Integrating Eq. (3.3.9) over the jet cross-section by r from 0 to ∞ , one arrives at the integral momentum balance

$$\int_0^{\infty} \frac{\partial}{\partial r} (\rho v_r v_z) dr + \int_0^{\infty} \frac{\partial}{\partial z} (\rho v_z^2) dr = \int_0^{\infty} \frac{\partial}{\partial r} \left(\mu r \frac{\partial v_z}{\partial r} \right) dr. \quad (3.3.10)$$

Evaluating the integrals in Eq. (3.3.10), we find

$$\rho v_r v_z \Big|_0^{\infty} + \frac{d}{dz} \int_0^{\infty} \rho v_z^2 dr = \mu r \frac{\partial v_z}{\partial r} \Big|_0^{\infty}. \quad (3.3.11)$$

The first term on the left-hand side in Eq. (3.3.11) is obviously equal to zero at the limit $r = 0$. On the other hand, at the limit, $r \rightarrow \infty$ one should account for the fact that solutions of the boundary layer equations for jets are known to exponentially decay as $r \rightarrow \infty$, i.e. denoting either v_z or v_r by f , one can expect their asymptotic behavior at least as

$$f \propto e^{-r} \quad (3.3.12)$$

and therefore,

$$\frac{\partial f}{\partial r} \propto e^{-r}. \quad (3.3.13)$$

Accordingly, applying L'Hopital's rule to evaluate the uncertainties we find that

$$rf \propto re^{-r} = \frac{r}{e^r} = \frac{1}{e^r} \rightarrow \frac{1}{e^\infty} \rightarrow \frac{1}{\infty} \rightarrow 0 \quad (3.3.14)$$

and

$$r \frac{\partial f}{\partial r} \propto re^{-r} = \frac{r}{e^r} = \frac{1}{e^r} \rightarrow \frac{1}{e^\infty} \rightarrow \frac{1}{\infty} \rightarrow 0. \quad (3.3.15)$$

Hence, the first term on the left-hand side in Eq. (3.3.11) vanishes. Similarly, the term on the right-hand side in Eq. (3.3.11) vanishes as well.

Then, the axial momentum balance equation (3.3.11) reduces to

$$\frac{d}{dz} \int_0^\infty \rho r v_z^2 dr = 0. \quad (3.3.16)$$

Since the derivative of a constant is zero, we conclude that

$$\int_0^\infty \rho r v_z^2 dr = \text{Constant} \quad (3.3.17)$$

which results in Eq. (3.3.1).

Now consider the derivation of the second integral invariant (3.3.2) from the foam balance equation (3.1.4). Re-write Eq. (3.1.4) by multiplying by r to obtain

$$\rho v_r \frac{\partial \phi}{\partial r} + \rho v_z \frac{\partial \phi}{\partial z} = \frac{\partial}{\partial r} \left(\rho D r \frac{\partial \phi}{\partial r} \right). \quad (3.3.18)$$

We now apply the chain rule to obtain from the first term on the left-hand side in Eq. (3.3.18) the following

$$\rho v_r \frac{\partial \phi}{\partial r} = \frac{\partial}{\partial r} (\rho v_r \phi) - \phi \frac{\partial (\rho v_r)}{\partial r}. \quad (3.3.19)$$

Again, applying the chain rule, we can rearrange the second term on the left-hand side in Eq. (3.3.18) to the following form

$$\rho v_z \frac{\partial \phi}{\partial z} = \frac{\partial}{\partial z} (\rho v_z \phi) - \phi \frac{\partial (\rho v_z)}{\partial z}. \quad (3.3.20)$$

Substituting Eqs. (3.3.19) and (3.3.20) into Eq. (3.3.18), we obtain,

$$\frac{\partial}{\partial r} (\rho v_r \phi) - \phi \frac{\partial \rho v_r}{\partial r} + \frac{\partial}{\partial z} (\rho v_z \phi) - \phi \frac{\partial \rho v_z}{\partial z} = \frac{\partial}{\partial r} \left(\rho D r \frac{\partial \phi}{\partial r} \right). \quad (3.3.21)$$

which can be transformed to the following form

$$\frac{\partial}{\partial r} (\rho v_r \phi) - \phi \left(\frac{\partial \rho v_r}{\partial r} + \frac{\partial \rho v_z}{\partial z} \right) + \frac{\partial}{\partial z} (\rho v_z \phi) = \frac{\partial}{\partial r} \left(\rho D r \frac{\partial \phi}{\partial r} \right). \quad (3.3.22)$$

The continuity Eq. (3.1.1) shows that the second terms on the left-hand side in the latter equation is equal to zero and it takes the following divergent form

$$\frac{\partial}{\partial r} (\rho v_r \phi) + \frac{\partial}{\partial z} (\rho v_z \phi) = \frac{\partial}{\partial r} \left(\rho D r \frac{\partial \phi}{\partial r} \right). \quad (3.3.23)$$

Integrating Eq. (3.3.23) across the jet cross-section, one obtains the integral balance of foam in the following form

$$\int_0^{\infty} \frac{\partial}{\partial r} (\rho r v_r \phi) dr + \int_0^{\infty} \frac{\partial}{\partial z} (\rho r v_z \phi) dz = \int_0^{\infty} \frac{\partial}{\partial r} \left(\rho D r \frac{\partial \phi}{\partial r} \right) dr. \quad (3.3.24)$$

Evaluating the integrals in Eq. (3.3.24), we obtain

$$\rho r v_r \phi \Big|_0^{\infty} + \frac{d}{dz} \int_0^{\infty} \rho r v_z \phi dr = \rho D r \frac{\partial \phi}{\partial r} \Big|_0^{\infty}. \quad (3.3.25)$$

Using the boundary conditions at the jet axis $r=0$ and at $r \rightarrow \infty$, one obtains

$$\frac{d}{dz} \int_0^{\infty} \rho r v_z \phi dr = 0. \quad (3.3.26)$$

which means that

$$\int_0^{\infty} \rho r v_z \phi dr = \text{Constant}. \quad (3.3.27)$$

The latter equation yields the second integral invariant (3.3.2).

3.4. Dimensionless Form of the Governing Equations

The following scales are used to render the governing equations dimensionless

$$\rho^* \rightarrow \rho_0, \quad r^* \rightarrow r_0, \quad z^* \rightarrow r_0, \quad v_r^*, v_z^* \rightarrow v_{z0}, \quad \mu^* = \mu_0 \quad (3.4.1)$$

where ρ_0 is the air density, r_0 is the nozzle radius, v_{z0} is the initial velocity, and μ_0 is the pure foam viscosity. Note, that in this section the dimensional parameters are denoted by asterisks for convenience, while the dimensionless ones do not have asterisks, in distinction from the notation used in sections 1-3 above. Then, the dimensionless parameters are introduced as following

$$\rho = \frac{\rho^*}{\rho_0}, \quad r = \frac{r^*}{r_0}, \quad v_r = \frac{v_r^*}{v_{z0}}, \quad v_z = \frac{v_z^*}{v_{z0}}, \quad \mu = \frac{\mu^*}{\mu_0}, \quad z = \frac{z^*}{r_0} \quad (3.4.2)$$

Using these scales, we obtain the continuity equation in the following dimensionless form

$$\frac{\partial}{\partial r}(\rho r v_r) + \frac{\partial}{\partial z}(\rho r v_z) = 0 \quad (3.4.3)$$

Then, the dimensionless momentum balance equation takes the following form

$$\rho \left[v_r \frac{\partial v_z}{\partial r} + v_z \frac{\partial v_z}{\partial z} \right] = \frac{1}{\text{Re}} \frac{1}{r} \frac{\partial}{\partial r} \left(\mu r \frac{\partial v_z}{\partial r} \right) \quad (3.4.4)$$

where the Reynolds number, Re , is defined as

$$\text{Re} = \frac{\rho_0 r_0 v_{z0}}{\mu_0} \quad (3.4.5)$$

The dimensionless rheological constitutive equation defining the dependence of viscosity on the air content involved in Eq. (3.4.4) reads

$$\mu = K(\phi) \left(\left| \frac{\partial v_z}{\partial r} \right| \right)^{n(\phi)-1} . \quad (3.4.6)$$

The air diffusion equation, after being rendered dimensionless acquires the following form

$$\rho \left[v_r \frac{\partial \phi}{\partial r} + v_z \frac{\partial \phi}{\partial z} \right] = \frac{1}{\text{Re}} \frac{1}{\text{Sc}} \frac{1}{r} \frac{\partial}{\partial r} \left(\rho r \frac{\partial \phi}{\partial r} \right) \quad (3.4.7)$$

where the additional dimensionless group, the Schmidt number

$$\text{Sc} = \frac{(\mu_0 / \rho_0)}{D} = \frac{v_0}{D} . \quad (3.4.8)$$

appears.

It is convenient to absorb the Reynolds number using the following longitudinal coordinate and radial velocity

$$x = \frac{z}{\text{Re}}, \quad v_r' = v_r \text{Re} \quad (3.4.9)$$

Then, the dimensionless continuity equation (3.4.3) becomes

$$\frac{\partial}{\partial r} (\rho r v_r') + \frac{\partial}{\partial x} (\rho r v_z) = 0 \quad (3.4.10)$$

While the dimensionless longitudinal momentum balance equation acquires the following form

$$\rho \left[v_r' \frac{\partial v_z}{\partial r} + v_z \frac{\partial v_z}{\partial x} \right] = \frac{1}{r} \frac{\partial}{\partial r} \left(\mu r \frac{\partial v_z}{\partial r} \right) \quad (3.4.11)$$

Similarly, the dimensionless air diffusion equation (3.4.7) is transformed as following

$$\rho \left[v_r' \frac{\partial \phi}{\partial r} + v_z \frac{\partial \phi}{\partial x} \right] = \frac{1}{\text{Sc}} \frac{1}{r} \frac{\partial}{\partial r} \left(\rho r \frac{\partial \phi}{\partial r} \right) \quad (3.4.12)$$

3.5. Density of Foam-slurry Mixtures

The mass balance of the foam-slurry mixture reads

$$\rho_0 V_a + \rho_s V_s = \rho^* (V_a + V_s) \quad (3.5.1)$$

where ρ_0 is the pure air density, ρ_s is the pure slurry density which is known, and ρ^* is the dimensional density of the foam-slurry mixture. Here V_a and V_s denote the volumes of air and slurry, respectively.

Dividing Eq. (3.5.1) by $\rho_0 (V_a + V_s)$, we have:

$$\frac{\rho_0 V_a}{\rho_0 (V_a + V_s)} + \frac{\rho_s V_s}{\rho_0 (V_a + V_s)} = \frac{\rho^* (V_a + V_s)}{\rho_0 (V_a + V_s)} \quad (3.5.2)$$

Recall that the basic definition of the foam content ϕ is

$$\phi = \frac{V_a}{V_a + V_s} \quad (3.5.3)$$

and hence

$$(1 - \phi) = \frac{V_s}{V_a + V_s} \quad (3.5.4)$$

The dimensionless density of the foam-slurry mixture is

$$\rho = \frac{\rho^*}{\rho_0} \quad (3.5.5)$$

Using Eqs. (3.5.3)- (3.5.5), one can transform Eq. (3.5.2) to the following final form

$$\rho(\phi) = \phi + \frac{\rho_s}{\rho_0}(1-\phi) \quad (3.5.6)$$

Note that the ratio ρ_s / ρ_0 is a known. Obviously, it is of the order of 10^3 .

3.6. Viscosity of Stucco-Water-Foam Suspensions

When a foam jet is issued in a slurry cross-flow which contains stucco and water at a certain WSR, a multiphase suspension is formed with the three main components: stucco, water and foam. The following expressions for the viscosity dependence in such three-phase suspension on the concentrations of the phases is used. These results were found experimentally by another PhD student, S. Jun in his thesis Jun (2013). They are presented in the form of the dependences of the two material parameters of the Ostwald-de Waele rheological constitutive equation (RCE) used for description of slurry, K and n (the consistency and flow behavior indexes, respectively), on the foam concentration ϕ . The Ostwald-de Waele RCE reads

$$\boldsymbol{\tau} = 2K(\phi) \left[2\text{tr}(\mathbf{D}^2) \right]^{[n(\phi)-1]/2} \mathbf{D} \quad (3.6.1)$$

with $\boldsymbol{\tau}$ being the deviatoric stress tensor and \mathbf{D} being the rate-of-stress tensor.

The following polynomial interpolation functions with foam volume content ϕ proposed by Jun (2013) are used in the numerical simulations in this Chapter as a variable are listed below

$$n(\phi) = a_0 \phi^6 + a_1 \phi^5 + a_2 \phi^4 + a_3 \phi^3 + a_4 \phi^2 + a_5 \phi + a_6 \quad (3.6.2)$$

$$K(\phi) = b_0 \phi^7 + b_1 \phi^6 + b_2 \phi^5 + b_3 \phi^4 + b_4 \phi^3 + b_5 \phi^2 + b_6 \phi + b_7 \quad (3.6.3)$$

where the coefficients involved in these formulas for two types of slurries (with WSR of 68 and WSR 75) are listed in Table 3.6.1.

TABLE 3.6.1

The coefficients involved in the empirical Eqs. (3.6.2) and (3.6.3).

	75 WSR	68 WSR		75 WSR	68 WSR
a ₀	-150.8	5.065	b ₀	-279879	0
a ₁	464.0	4.355	b ₁	1119110	41912
a ₂	-534.9	-33.25	b ₂	-1792230	-156380
a ₃	283.8	37.44	b ₃	1457320	225770
a ₄	-67.81	-15.32	b ₄	-626658	-157420
a ₅	6.008	2.143	b ₅	134280	54116
a ₆	0.04987	0.042	b ₆	-12805	-8844.2
			b ₇	903.18	871.50

Equation (3.1.3) follows from the rheological constitutive equation (3.6.1) in the boundary-layer approximation for the jet flow under consideration.

4. STRAIGHT FOAM JET INJECTED INTO SLURRY: NUMERICAL METHOD

4.1. Coordinate Transformation for Numerical Solution

The presence of the physical domain in the jet which is infinite in the radial direction, makes it practically impossible to reproduce the main features of the problem, the invariants (3.3.1) and (3.3.2), numerically. This difficulty can be avoided using the coordinate transformation of the physical plane $0 \leq z \leq \infty$, $0 \leq r \leq \infty$ into a finite strip in the artificial plane $0 \leq \xi \leq \infty$, $0 \leq \eta \leq \eta_0$, as sketched in Figure 4.1.1. Such coordinate transformation can be achieved following the ideas described in Dzhaugashtin et al. (1977, 1978, 1979, 1981) and Yarin (1984). Namely, the following new longitudinal and transversal coordinates ξ and η are introduced

$$\xi = x, \quad \eta(r, x) = \int_0^r \rho \phi v_z r dr \quad (4.1.1)$$

which results in the integration domain in the form of a semi-infinite (along the jet) strip sketched in Figure 4.1.1. Indeed, the upper limit of the transversal coordinate η of Eq. (4.1.1) is set up by the integral invariant of the problem (3.3.3).

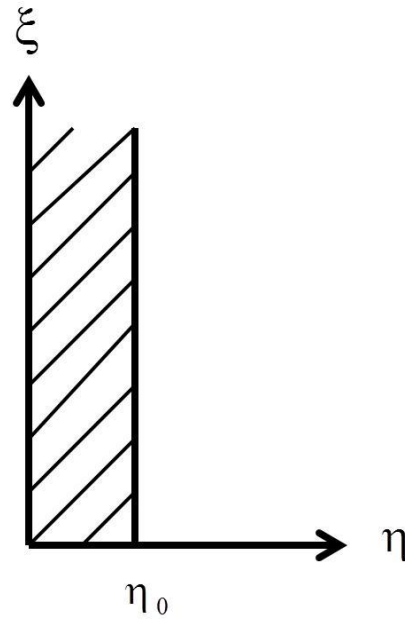


Figure 4.1.1. Integration domain in new coordinates.

The coordinate transformations are given by the following formulas

$$\frac{\partial}{\partial x} = \frac{\partial}{\partial \xi} + \frac{\partial \eta}{\partial x} \frac{\partial}{\partial \eta} . \quad (4.1.2)$$

$$\frac{\partial}{\partial r} = \frac{\partial \eta}{\partial r} \frac{\partial}{\partial \eta} \quad (4.1.3)$$

Taking account of the second Eq. (4.1.1), we find

$$\frac{\partial \eta}{\partial r} = \rho \phi_{v_z r} \frac{\partial}{\partial \eta} \quad (4.1.4)$$

Substituting Eq. (4.1.4) into (4.1.3), we find that

$$\frac{\partial}{\partial r} = \rho v_z r \frac{\partial}{\partial \eta} \quad (4.1.5)$$

In addition, from Eq. (3.4.12) with the help of the continuity equation (3.4.10), we obtain the former equation in the divergent form, namely

$$\frac{\partial}{\partial r} (\rho v_r \dot{\phi}) + \frac{\partial}{\partial x} (\rho v_z \phi) = \frac{1}{Sc} \frac{\partial}{\partial r} \left(\rho r \frac{\partial \phi}{\partial r} \right) \quad (4.1.6)$$

Integrating this equation by r from 0 to r , we obtain

$$\rho v_r \dot{\phi} \Big|_0^r + \frac{\partial}{\partial x} \int_0^r \rho v_z \phi dr = \frac{\rho r}{Sc} \frac{\partial \phi}{\partial r} \Big|_0^r \quad (4.1.7)$$

Using the boundary conditions at the jet axis $r=0$, namely the last Eq. (3.2.2), and recalling the definition of η in the second Eq. (4.1.1), we arrive at the following expression

$$\rho v_r \dot{\phi} + \frac{\partial \eta}{\partial x} = \frac{\rho r}{Sc} \frac{\partial \phi}{\partial r} \quad (4.1.8)$$

which means that

$$\frac{\partial \eta}{\partial x} = \frac{\rho r}{Sc} \frac{\partial \phi}{\partial r} - \rho v_r \dot{\phi} \quad (4.1.9)$$

Therefore, combining together Eqs. (4.1.2), (4.1.4) and (4.1.9), one obtains the final version of the coordinate transformation

$$\frac{\partial}{\partial x} = \frac{\partial}{\partial \xi} + \left[\frac{\rho r}{Sc} \frac{\partial \phi}{\partial r} - \rho v_r \dot{\phi} \right] \frac{\partial}{\partial \eta} \quad (4.1.10)$$

$$\frac{\partial}{\partial r} = \rho\phi v_z r \frac{\partial}{\partial \eta} \quad (4.1.11)$$

Transform Eq. (3.4.11) to the new coordinate ξ and η using the transformation formulas (4.1.10) and (4.1.11). Then, we have

$$\rho v_r \rho \phi v_z r \frac{\partial v_z}{\partial \eta} + \rho v_z \left[\frac{\partial v_z}{\partial \xi} + \frac{\partial v_z}{\partial \eta} \left(\frac{\rho r}{Sc} \frac{\partial \phi}{\partial r} - \rho v_r \phi \right) \right] = \frac{1}{r} \rho \phi v_z r \frac{\partial}{\partial \eta} \left[\mu r \rho \phi v_z r \frac{\partial v_z}{\partial \eta} \right] \quad (4.1.12)$$

Combining similar terms, we obtain from Eq. (4.1.12) the following form of the momentum balance equations which will be used in the numerical simulations

$$\frac{\partial v_z}{\partial \xi} = \phi \frac{\partial}{\partial \eta} \left[\mu r^2 \phi v_z \frac{\partial v_z}{\partial \eta} \right] - \frac{\rho r}{Sc} \frac{\partial \phi}{\partial r} \left[\frac{\partial v_z}{\partial \eta} \right] \quad (4.1.13)$$

Similarly, transform the foam convection-diffusion equation (3.4.12) to the new coordinate ξ and η using the transformation formulas (4.1.10) and (4.1.11). Accordingly, we obtain

$$\rho v_r \rho \phi v_z r \frac{\partial \phi}{\partial \eta} + \rho v_z \left[\frac{\partial \phi}{\partial \xi} + \left(\frac{\rho r}{Sc} \frac{\partial \phi}{\partial r} - \rho v_r \phi \right) \frac{\partial \phi}{\partial \eta} \right] = \frac{1}{Sc} \frac{1}{r} \rho \phi v_z r \frac{\partial}{\partial \eta} \left[\rho r \rho \phi v_z r \frac{\partial \phi}{\partial \eta} \right] \quad (4.1.14)$$

Then, combining the similar terms, we obtain the foam convection-diffusion equation to the following form which will be used in the numerical simulations

$$\frac{\partial \phi}{\partial \xi} = \frac{1}{Sc} \phi \frac{\partial}{\partial \eta} \left[\rho^2 r^2 \phi v_z \frac{\partial \phi}{\partial \eta} \right] - \left[\frac{\rho r}{Sc} \frac{\partial \phi}{\partial r} \right] \frac{\partial \phi}{\partial \eta}. \quad (4.1.15)$$

The system of the two conjugate equations (4.1.13) and (4.1.15) is to be solved numerically to determine the fields of the longitudinal velocity v_z and the air content ϕ .

Note, that according to Eqs. (3.1.3) and (4.1.11) the viscosity function takes the following form in the new coordinates

$$\mu = K(\phi) \left[\rho \phi v_z r \frac{\partial v_z}{\partial \eta} \right]^{n(\phi)-1} \quad (4.1.16)$$

The return to the physical coordinates x and r is achieved using the first Eq. (3.1.3) and Eq. (4.1.11) as

$$x = \xi, \quad r^2 = 2 \int_0^\eta \frac{d\eta}{\rho \phi v_z} \quad (4.1.17)$$

Note that the second Eq. (4.1.17) is obtained using Eq. (4.1.11) in the following way.

$$1 = \frac{\partial r}{\partial r} = \rho \phi v_z r \frac{\partial r}{\partial \eta} \quad (4.1.18)$$

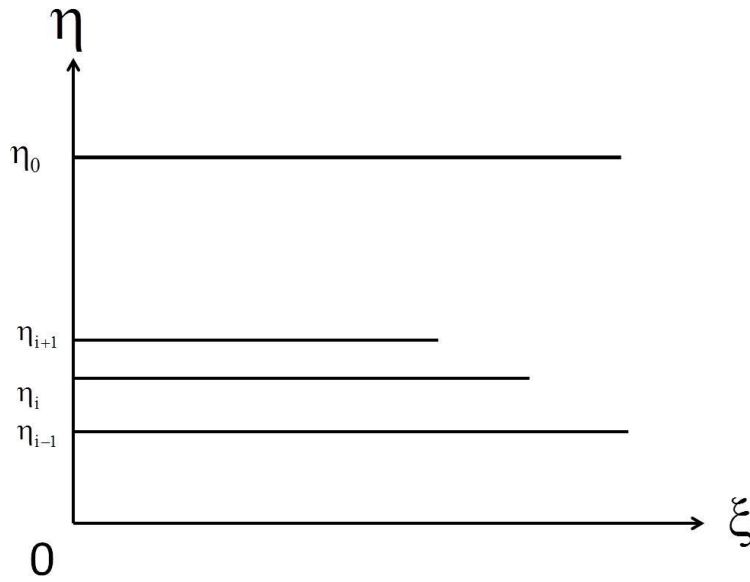
The fact that

$$\rho \phi v_z r \frac{\partial r}{\partial \eta} = 1 \quad (4.1.19)$$

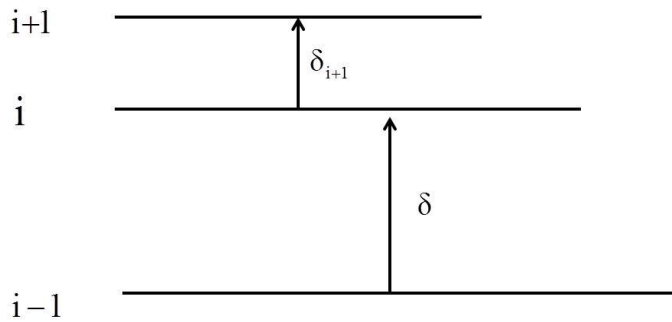
allows one to rewrite Eq. (4.1.19) in the integral form of the second Eq. (4.1.17). Note, also that the numerical integration of Eqs. (4.1.13) and (4.1.15) fully determines the dependences of the functions ρ , ϕ and v_z on ξ and η . Therefore, the evaluation of the integral in the second Eq. (4.1.17) is possible, and thus is possible the return from the new coordinates used for numerical simulations ξ and η to the physical ones x and r . Accordingly, the functions $v_z(\xi, \eta)$ and $\phi(\xi, \eta)$ are transformed to the functions $v_z(x, r)$ and $\phi(x, r)$.

4.2. Numerical Solution Algorithm

Equations (4.1.2) and (4.1.3) are solved numerically by using the method of straight lines. Namely, the derivatives in η are discretized on the straight lines shown in Figure 4.2.1 located at intervals δ_i .



(a)



(b)

Figure 4.2.1 Semi-discretization of the partial differential equations.

Then, the first and second derivatives in η of all functions f involved in the partial differential equations of the problem take the following form

$$\left(\frac{\partial f}{\partial \eta}\right)_i = S_i f_{i+1} - R_i f_{i-1} + Z_i f_i \quad (4.2.1)$$

$$\left(\frac{\partial^2 f}{\partial \eta^2}\right)_i = V_i f_{i+1} + W_i f_{i-1} - F_i f_i \quad (4.2.2)$$

where the coefficients are related to the inter-line increments δ_i by the following relations

$$S_i = \frac{\delta_i}{\delta_{i+1}(\delta_i + \delta_{i+1})} \quad (4.2.3)$$

$$R_i = \frac{\delta_{i+1}}{\delta_i(\delta_i + \delta_{i+1})} \quad (4.2.4)$$

$$Z_i = \frac{\delta_{i+1} - \delta_i}{\delta_i \delta_{i+1}} \quad (4.2.5)$$

$$V_i = \frac{2}{\delta_{i+1}(\delta_i + \delta_{i+1})} \quad (4.2.6)$$

$$W_i = \frac{2}{\delta_i(\delta_i + \delta_{i+1})} \quad (4.2.7)$$

$$F_i = \frac{2}{\delta_i \delta_{i+1}} \quad (4.2.8)$$

The non-equidistant locations of the straight lines is convenient, since this allows one to have denser coverage in the areas where function gradients are expected to be the largest, i.e. at the outer zones of the jets in the η -coordinate.

As a result of such semi-discretization, the partial differential equations Eqs. (4.1.13) and (4.1.15) become the ordinary differential equations for the function values f_i on the straight lines.

Namely, they reduce to the following system of the conjugate ordinary differential equations in ξ

$$\frac{dv_{zi}}{d\xi} = P_i \left(\frac{\partial^2 v_z}{\partial \eta^2} \right)_i + \phi_i \left(\frac{\partial Q}{\partial \eta} \right)_i \left(\frac{\partial v_z}{\partial \eta} \right)_i - \frac{(\rho^2 r^2 \phi v_z)_i}{S_c} \left(\frac{\partial \phi}{\partial \eta} \right)_i \left(\frac{\partial v_z}{\partial \eta} \right)_i \quad (4.2.9)$$

$$\frac{d\phi_i}{d\xi} = L_i \left(\frac{\partial^2 \phi}{\partial \eta^2} \right)_i + \frac{\phi_i}{S_c} \left(\frac{\partial M}{\partial \eta} \right)_i \left(\frac{\partial \phi}{\partial \eta} \right)_i - \frac{(\rho^2 r^2 \phi v_z)_i}{S_c} \left(\frac{\partial \phi}{\partial \eta} \right)_i^2 \quad (4.2.10)$$

where the following notation is introduced for brevity

$$P = \mu \rho r^2 \phi^2 v_z \quad (4.2.11)$$

$$Q = \mu \rho r^2 \phi v_z \quad (4.2.12)$$

$$L = \frac{\rho^2 r^2 \phi^2 v_z}{S_c} \quad (4.2.13)$$

$$M = \rho^2 r^2 \phi v_z \quad (4.2.14)$$

4.3. Treatment of the Boundary Conditions in Numerical Simulations

In the new coordinates ξ and η care should be taken in reformulating the boundary conditions (3.2.2) and (3.2.3). The corresponding straight lines and their numbering are shown in Figure 4.3.1.

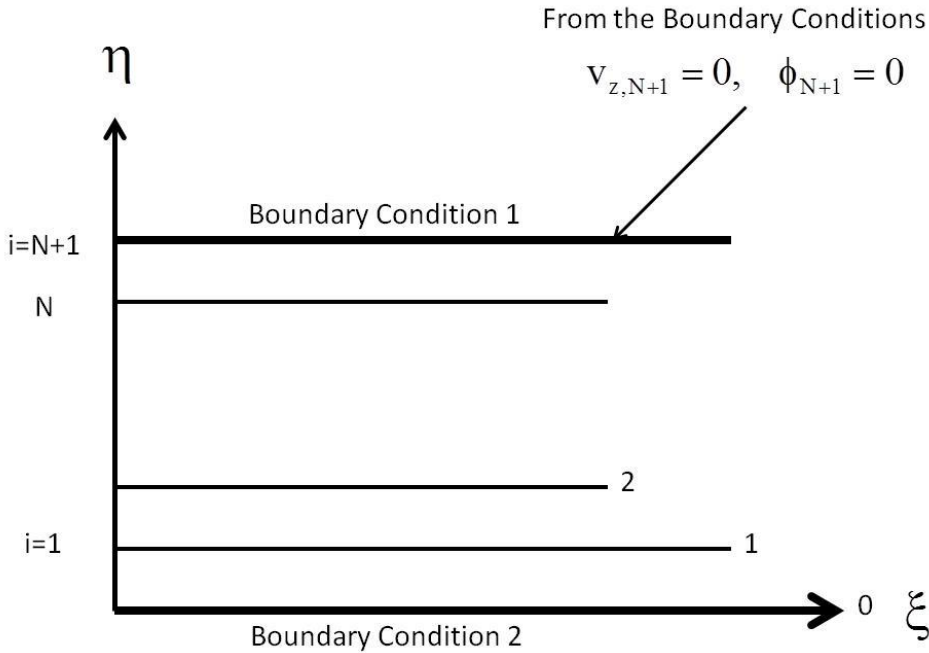


Figure 4.3.1. Posing boundary conditions in the $\xi\eta$ -plane.

The axial boundary conditions imply the following Taylor series to be valid near the jet axis

$$v_z = A + r^2 B, \quad \phi = C + r^2 D \quad (4.3.1)$$

Given the second Eq. (4.1.17) that means that

$$r^2 \approx 2 \frac{1}{\rho_0 \phi_0 v_{z0}} \int_0^\eta d\eta = 2 \frac{1}{\rho_0 \phi_0 v_{z0}} \eta \quad (4.3.2)$$

The latter equation shows that

$$r^2 \propto \eta \quad (4.3.3)$$

Accordingly, Eqs. (4.3.1) yield

$$v_z = A + B'\eta, \quad \phi = C + D'\eta \quad (4.3.4)$$

Applying Eqs. (4.3.3) and (4.3.4) at lines 1 and 2, we obtain

$$v_{z1} = A + B'\eta_1 \leftarrow \text{on Line 1} \quad (4.3.5)$$

$$v_{z2} = A + B'\eta_2 \leftarrow \text{on Line 2} \quad (4.3.6)$$

Solving the system of two Eqs. (4.3.5) and (4.3.6), we find the relation of the longitudinal velocity and air content in the jet with the velocity values at the neighboring straight lines, where the numerical integration is applied

$$v_{zo} = \frac{\eta_2 v_{z1} - \eta_1 v_{z2}}{\eta_2 - \eta_1} \quad (4.3.7)$$

Proceeding likewise for the second Eq. (4.3.4), we find

$$\phi_1 = C + D'\eta_1 \leftarrow \text{on Line 1} \quad (4.3.8)$$

$$\phi_2 = C + D'\eta_2 \leftarrow \text{on Line 2} \quad (4.3.9)$$

and thus

$$\phi_0 = \frac{\eta_2 \phi_1 - \eta_1 \phi_2}{\eta_2 - \eta_1} \quad (4.3.10)$$

On the other hand, the boundary conditions at the outer edge of the integration domain

$$v_{z,N+1} = 0, \quad \phi_{N+1} = 0 \quad (4.3.11)$$

These latter boundary conditions are imposed at $\eta = \eta_0$. The value of η_0 is established using the integral invariant (3.3.27) and the initial conditions at the nozzle exit, which are sketched in Figure 4.3.2.

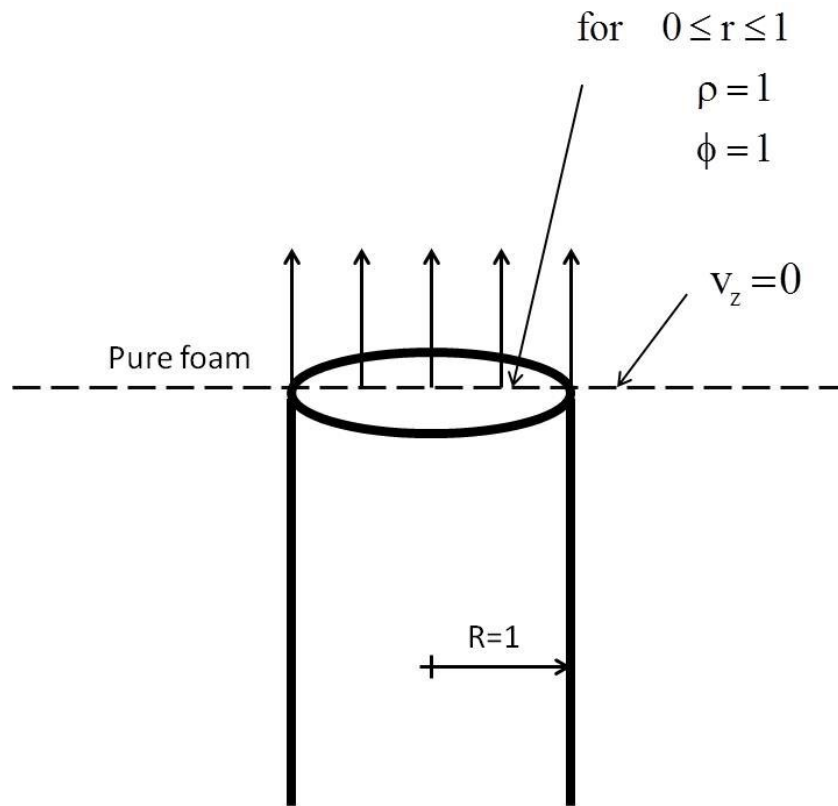


Figure 4.3.2. The initial conditions at the nozzle exit.

The initial conditions depicted in Figure 4.3.2 are imposed at $0 \leq r \leq 1$; $\xi = 0$, where they read

$$\rho = 1; \quad \phi = 1; \quad v_z = 1 \quad (4.3.12)$$

with foam injection being effectively air injection.

Also, we have (see Figure 4.3.2)

$$r > 1, \quad v_z = 0 \quad (4.3.13)$$

Substituting the initial conditions (4.3.12) and (4.3.13) into the integral invariant (3.3.27), we obtain

$$\eta_0 = \int_0^{\infty} \rho \phi v_z r dr = \frac{1}{2} \quad (4.3.14)$$

The initial and boundary conditions, as well as the flow domain in the new coordinates ξ and η used to integrate numerically the system of the ordinary differential equations (4.2.9) and (4.2.10) are summarized in Figure 4.3.3. Since these are parabolic equations, they do not require any boundary conditions at $\xi = \infty$.

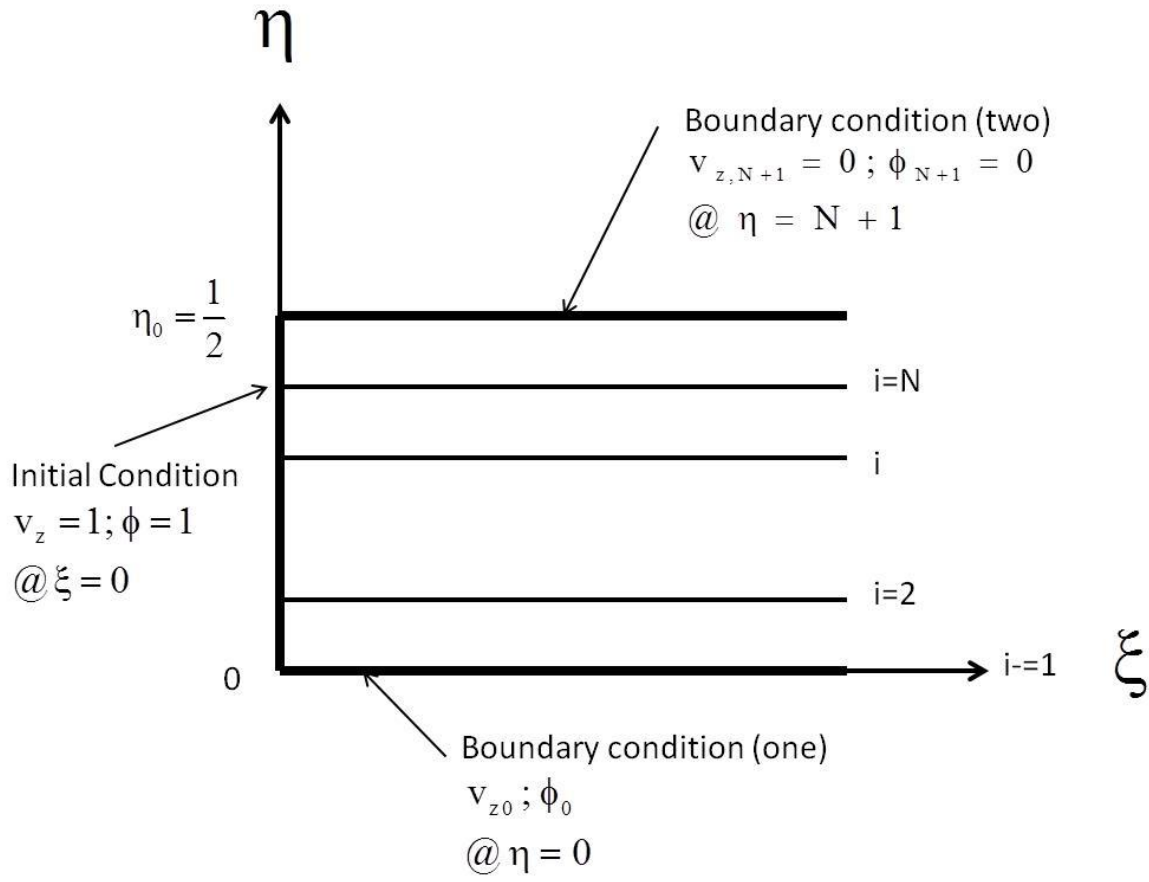


Figure 4.3.3. The integration domain and the initial and boundary conditions.

5. NUMERICAL RESULTS FOR STRAIGHT FOAM JETS ISSUED INTO SLURRY

5.1. The results for WSR 68

A novel computer code was developed, which realized the algorithm described in the previous sections. Several numerical results obtained using this code will be discussed below.

In order to generate a comprehensive set of results which could elucidate the peculiarities of flow development in foam jets issued into slurry, a systematic array of data had to be generated from the computer program. For this purpose a FORTRAN computer code (see Appendix 1) was developed. Then, realistic data ranges were determined. Certain variables were held constant while others changed incrementally, one at a time. This produced an extensive series of result files for each variable. These result files were then loaded into Tecplot 8.0 graphics software to produce a series of four different line graphs and two different field plots. This methodology provides a wealth of data that enables us to gain an understanding of the flow of the foam jet issued into the slurry under many varying geometries, different types of rheological behavior and flow conditions. The logic for analysis follows.

The input files for our computer program called described in detail in Appendix 1 are as shown in the following Table 5.1. Variables relating to the mesh of the numerical analysis program are held fixed, while flow and rheological factors are variable.

Table 5.1 Input files for the FORTRAN code described in detail in Appendix 1.

Vzo	Ro	Sc	RSRO	WSR	N	TOP	PT	NXXG	NYYG	SINGLE
vary	vary	vary	100	68	40	206	5	40	40	1

The meaning of the input parameters listed is the following:

Vzo, the initial velocity- two main cases were analyzed: 500 and 1000 cm/s.

Ro, the initial radius of the jet was varied from 1/16 in. (.15875 cm) to 3 ¼ in. (8.225 cm).

Sc, the Schmidt number was varied in the range of 2.8 to 46.4. The program was stable in the entire domain.

WSR, the water stucco ratio, was either 68 or 75. These are the typical values for which the rheological constitutive equation was established, see section 3.6.

N was the number of straight lines used in the numerical analysis. It was set at either 20 or 40, with no significant differences in the results, which proves the finite-difference approximation of the partial differential equations governing the problem.

TOP regulated the length of the interval along the jet axis ξ which one can achieve. A typical value used is listed in Table 5.1. It should be emphasized that the value of TOP is not equal to the value of ξ .

PT regulated the frequency at which the detailed velocity and foam content profiles in the jet were plotted. A typical value used is listed in Table 5.1.

The three additional input parameters NXXG , NYYG and SINGLE regulated the plotting features and are auxiliary.

After a set of input variables are loaded, the computer program generates resultant data files containing the final computed variable sets as indicated below.

<u>Resultant Data File</u>	<u>Computed Variable</u>	<u>Computed Variable Set</u>
km1	Effective Viscosity, μ	μ versus the radial coordinate r in a cross-section
km2	Half Jet Width	Half Jet Width versus the axial coordinate z in the jet
km4	Fraction Foam to Slurry, ϕ	ϕ versus the radial coordinate r in a cross-section
km5	Axial Velocity, v_z	v_z versus the radial coordinate r in a cross-section
km471	ϕ Foam Content Field	on the plane Orx
km472	v_z Velocity Field	on the plane Orx

Each run of the computer program generated the four above-mentioned line graph arrays and the two above-mentioned field arrays.

A representative set of results is discussed below first. Then, some additional results are introduced.

The first representative set of data is for:

(i) Variation of the resulting parameters with the pipe radius R_0 and two values of the Schmidt number : $Sc=18$, (c) $Sc=30$

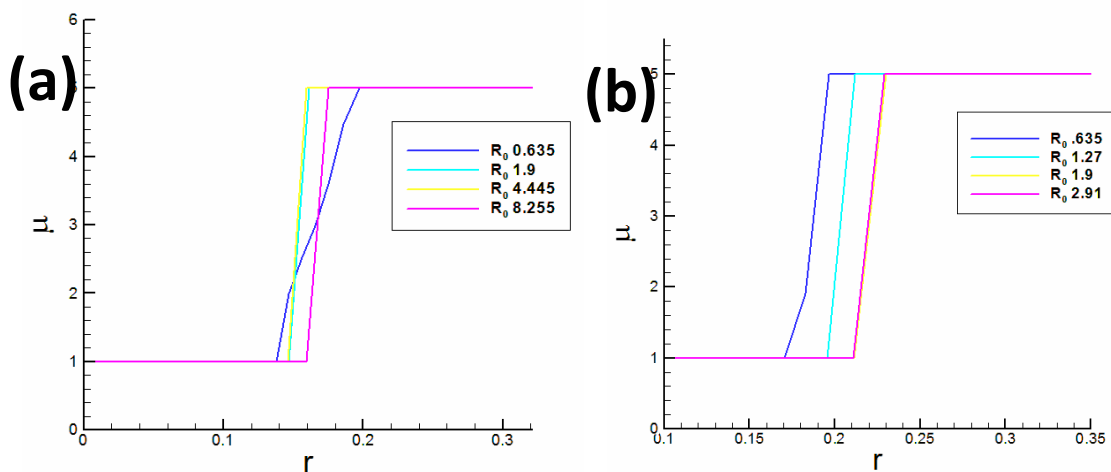


Figure 5.1.1. Dependence of the effective viscosity on R_0 (the values shown in the panels are in centimeters). (a) $Sc=18$, (b) $Sc=30$. The value of $x=0.04$. WSR 68.

Figure 5.1.1 shows the variation of the effective viscosity as function of the nozzle radius. Panel (b) in Figure 5.1.1 shows that the effective viscosity changes from the foam viscosity to the mixture viscosity as r increases. This effective viscosity change is fairly independent of nozzle radius. As the Schmidt number Sc number increases (lower diffusion transfer relative to the momentum transfer), it is observed that the viscosity change from foam viscosity to the mixture viscosity occurs over a wider range of r .

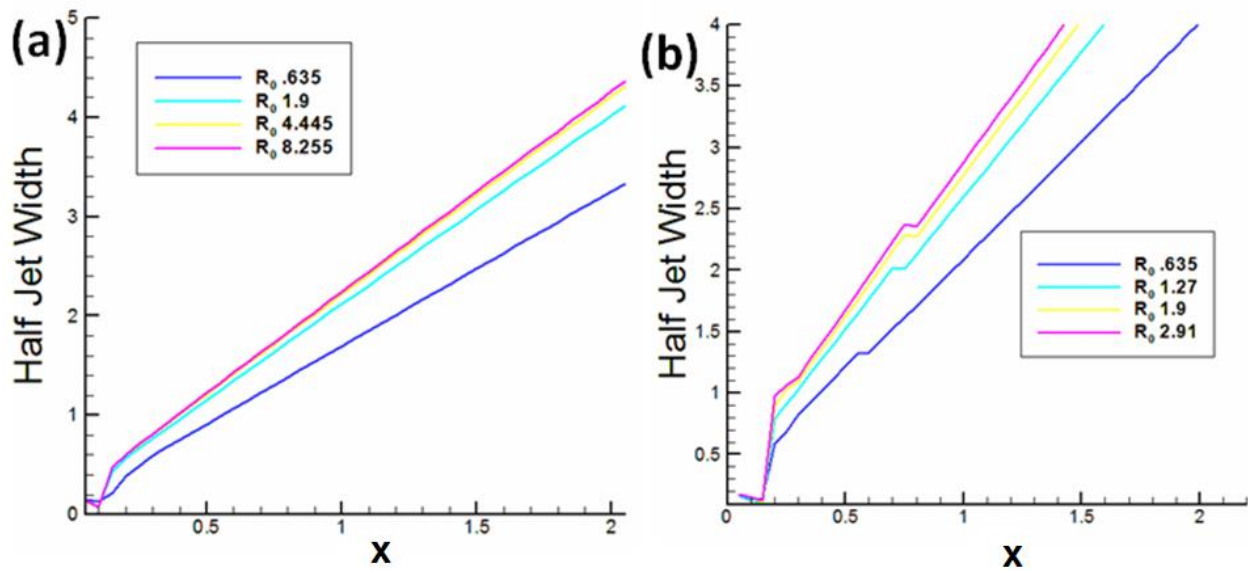


Figure 5.1.2. Dependence of half-jet width on the nozzle radius R_0 (the values shown in the panels are in centimeters). (a) $Sc=18$, (b) $Sc=30$. WSR 68.

Figure 5.1.2 shows the dependence of the half-jet width as a function of the axial distance z for several values of the nozzle radius R_0 and the Schmidt number Sc . As panel (b) in Figure

5.1.2 shows, the half-jet width is an almost linear function of the axial distance x . As the nozzle radius increases, the slope of the half-jet width decreases, indicating a wider mixing zone. Also, as the Schmidt number Sc increases (lower diffusion transfer relative to the momentum transfer), there is a significant increase in the half-jet width at any given R_0 . Similarly to Figure 5.1.1, this indicates that the mixing zone increases as diffusion rate decreases.

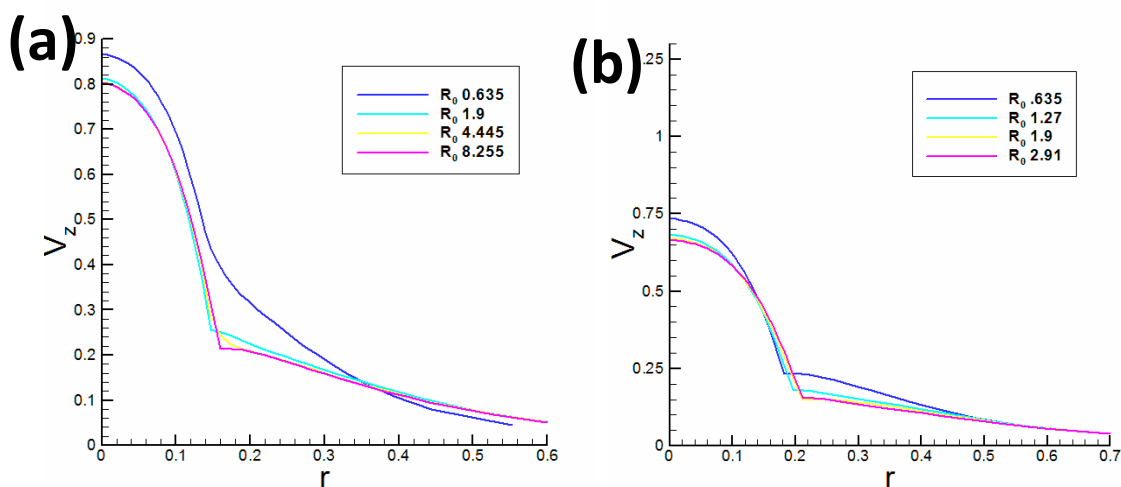


Figure 5.1.3. Dependence of the longitudinal velocity profile on the nozzle radius R_0 (the values shown in the panels are in centimeters). (a) $Sc=18$, (b) $Sc=30$. The value of $x=0.04$. WSR 68.

Figure 5.1.3 shows the dependence of velocity as a function of the radial distance, r . Panel (b) shows that the velocity is maximal at the jet axis $r = 0$ and decreases as the radial distance increases. As the Schmidt number Sc increases (lower diffusive transfer relative to the momentum transfer), the axial velocity at the center decreases. The results show that the momentum transfer from the foam to the mixture occurs over a similar range of relative radii r and is practically independent of the pipe radius. Note, that the kinks visible on the velocity

profiles result from the abrupt increase in the effective viscosity in the outer region of the jet where the shear rates are low, and thus the power-law fluid possesses a high viscosity, in distinction from the central region of the jet.

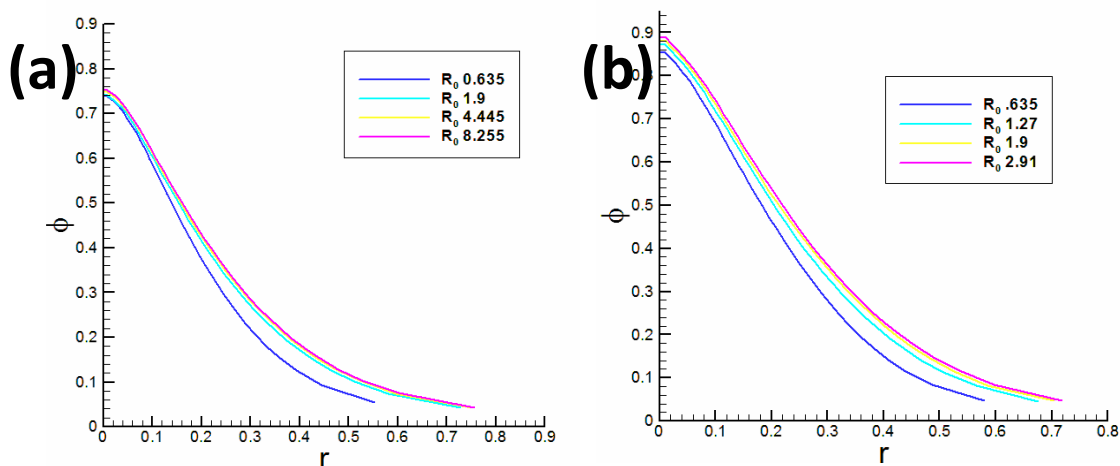


Figure 5.1.4. Profiles of the foam content ϕ at different values of the nozzle radius (the values shown in the panels are in centimeters). (a) $Sc=18$, (b) $Sc=30$. The value of $x=0.04$. WSR 68.

Figure 5.1.4 shows the dependence of the air/foam content as a function of the radial distance r . Panel (b) shows that the foam content is maximal at the jet axis and smoothly decreases in the radial direction in distinction from the longitudinal velocity profiles shown in Figure 5.1.3. The smoothness of the foam content profiles results from the fact that the air diffusion coefficient is constant, in distinction from the effective viscosity. An increase in the Schmidt number only slightly affects the foam content profiles. These results show that the effective foam mixing zone is comparable under different conditions and practically independent of the nozzle radius R_0 .

The results of the numerical simulations allow parametric study of the effects of the Schmidt number, the initial velocity at the nozzle exit v_{z0} , etc. They also allow full reconstruction of the foam content in the entire jet domain, as is shown in Figure 5.1.5.

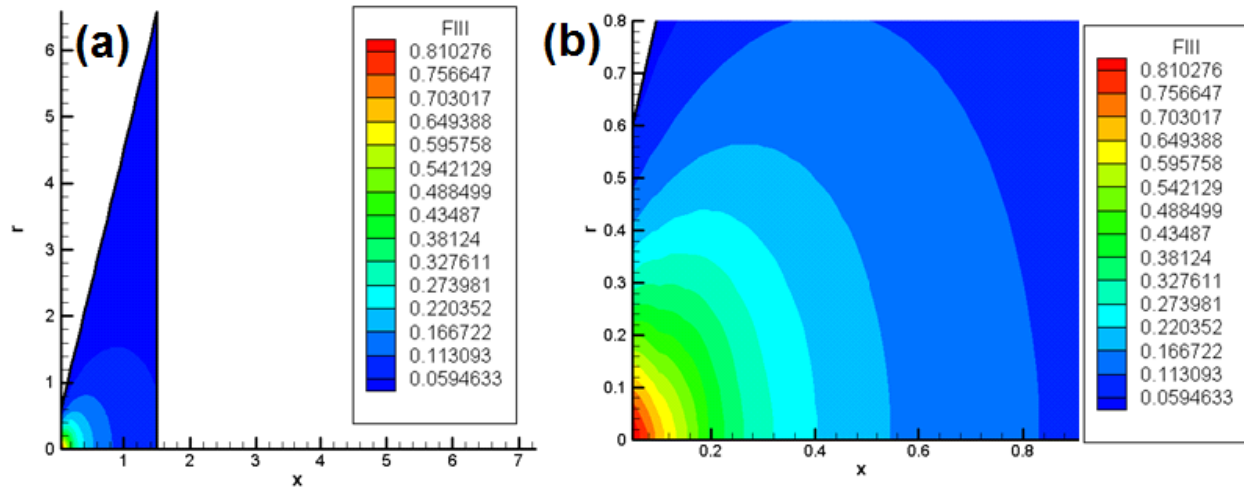


Figure 5.1.5. Foam content in the submerged jet. The following values of the parameters were used: $v_z=1000$, $R_0=1.9$ cm, $Sc= 30$. The panel (a) shows the global view, whereas panel (b) shows the zoomed-in views of the central part of the jet. WSR 68.

The second representative set of data is for:

(ii). Variation of the resulting parameters with the Schmidt number Sc and the two values of the initial velocity of the foam jet: (a) $v_{z0} = 500$, (b) $v_{z0} = 1000$

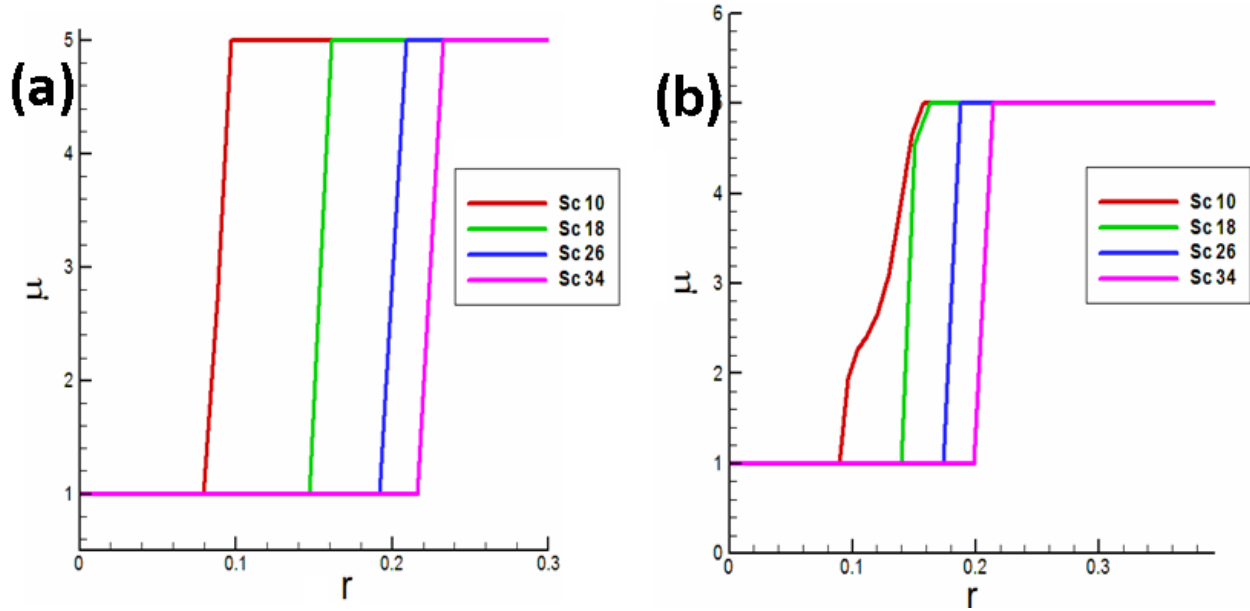


Figure 5.1.6. Dependence of the effective viscosity on the radial coordinate in the jet cross-section at different values of the Schmidt number. (a) $v_{z0} = 500$ cm/s, (b) $v_{z0} = 1000$ cm/s. The value of $x = 0.04$. WSR 68.

Figure 5.6 shows that as the Schmidt number Sc number increases (which means a reduction in the diffusion transfer relative to the momentum transfer), the viscosity change from the foam viscosity to the mixture viscosity occurs over a wider range of r , which is consistent with the observations in item (i).

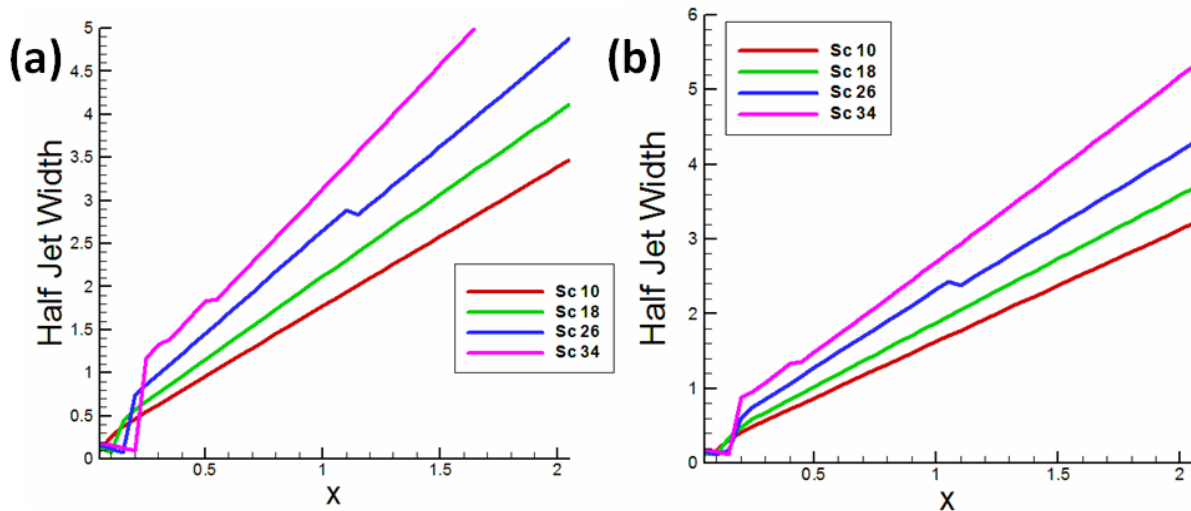


Figure 5.1.7. Dependence of half jet width for different values of the Schmidt number Sc . Panel (a) $v_{z0} = 500$ cm/s, panel (b) $v_{z0} = 1000$ cm/s. WSR 68.

Figure 5.1.7 shows that as the Schmidt number Sc increases (the diffusion coefficient decreases), the half-jet width increases for both values of the initial velocity of the foam jet. The effect of the Schmidt number noticed here is similar to the one observed in item (i).

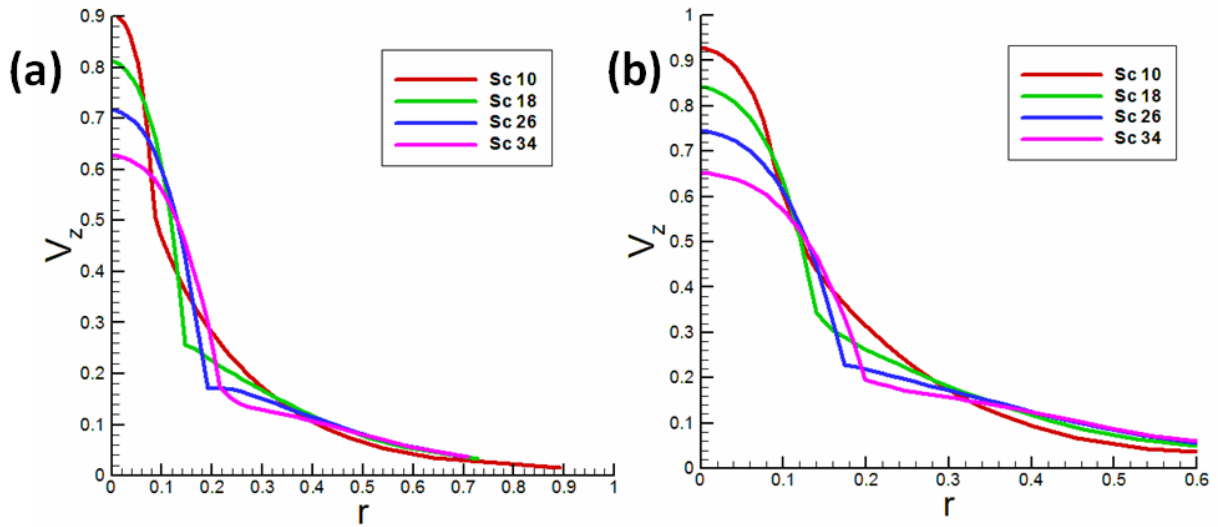


Figure 5.1.8. The axial velocity profiles at different values of the Schmidt number and for the following two values of the initial velocity of the foam jet: (a) $v_{z0} = 500$ cm/s, (b) $v_{z0} = 1000$ cm/s. The value of $x = 0.04$. WSR 68.

Figure 5.1.8 depicts the dependence of the longitudinal velocity in the jet as on the radial distance, r . The velocity is maximal at the jet axis $r = 0$ and decreases as the radial distance increases. For the larger Schmidt numbers Sc (lower diffusion coefficients), the axial velocity at the center diminishes. This behavior is associated with the complex dependence of the effective viscosity μ on the foam content ϕ described in section 3.6. The kinks in the velocity profiles result from an abrupt increase in the effective viscosity in the outer region when the content approaches that of pure slurry.

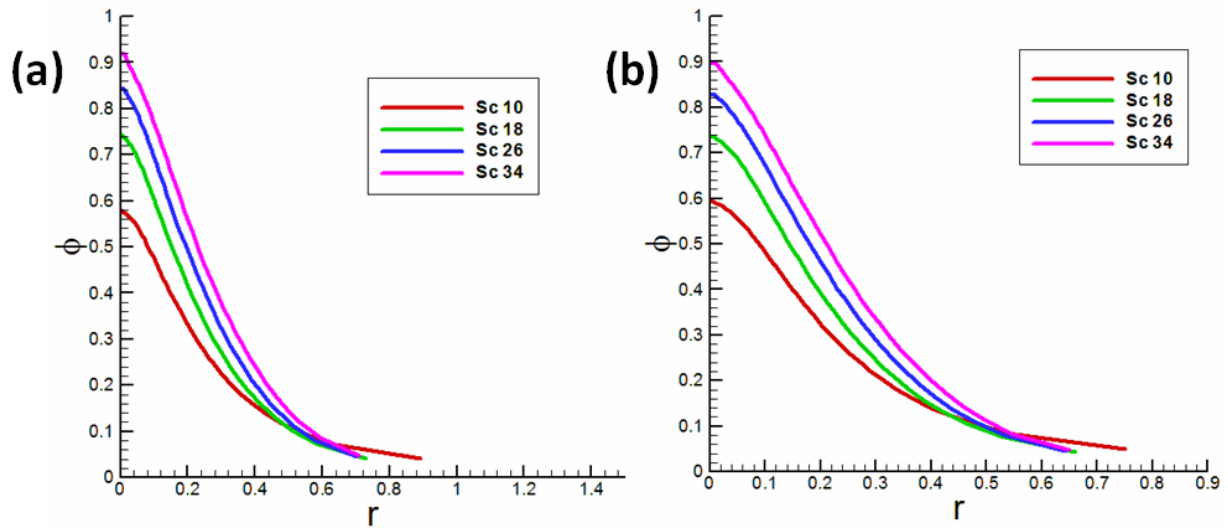


Figure 5.1.9. Dependence of the foam content on the radial coordinate in the jet cross-section predicted at different values of the Schmidt number Sc at two values of the initial velocity of the foam jet: (a) $v_{z0} = 500$ cm/s, (b) $v_{z0} = 1000$ cm/s. The value of $x=0.04$. WSR 68.

Figure 5.1.9 depicts the dependence of the air/foam content as a function of the radial distance r in the same cross-section of the jet at different values of the Schmidt number. At the higher values of the Schmidt number (weaker air diffusion), the foam content at the jet axis is higher, i.e. the foam mixing process is poorer.

The third representative set of data is for:

(iii). Variation with of the resulting parameters with the initial velocity of the foam jet v_{z0}

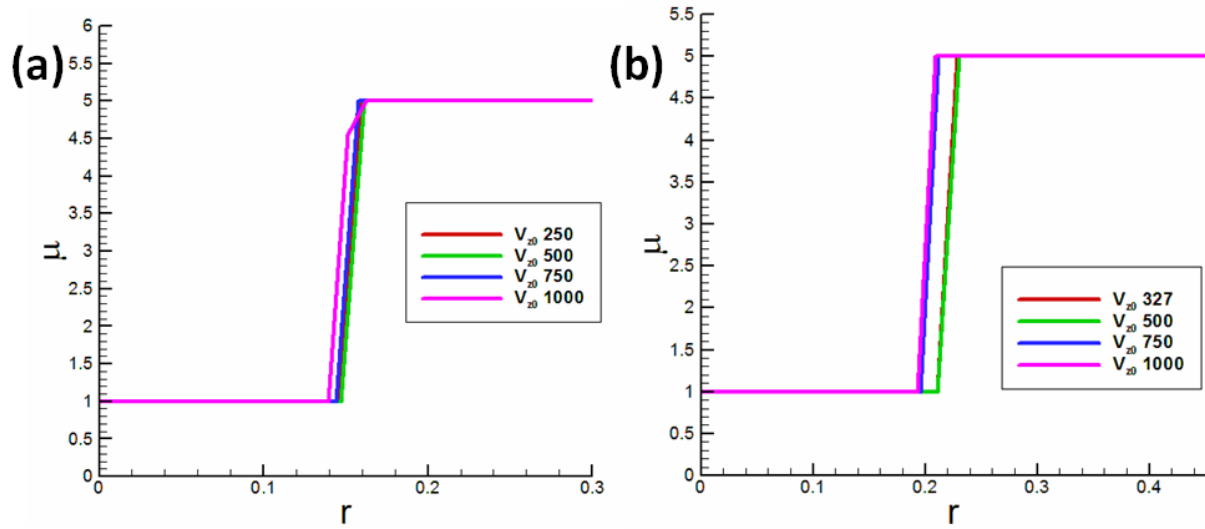


Figure 5.1.10. Profiles of the effective viscosity at different values of the initial foam jet velocity v_{z0} (shown in the insets in cm/s). (a) $Sc=18$, (b) $Sc=30$. The value of $x=0.04$. WSR 68.

Figure 5.1.10 reveals that the effect of the initial velocity of the foam jet on the effective viscosity profile is relatively small for both values of the Schmidt number Sc .

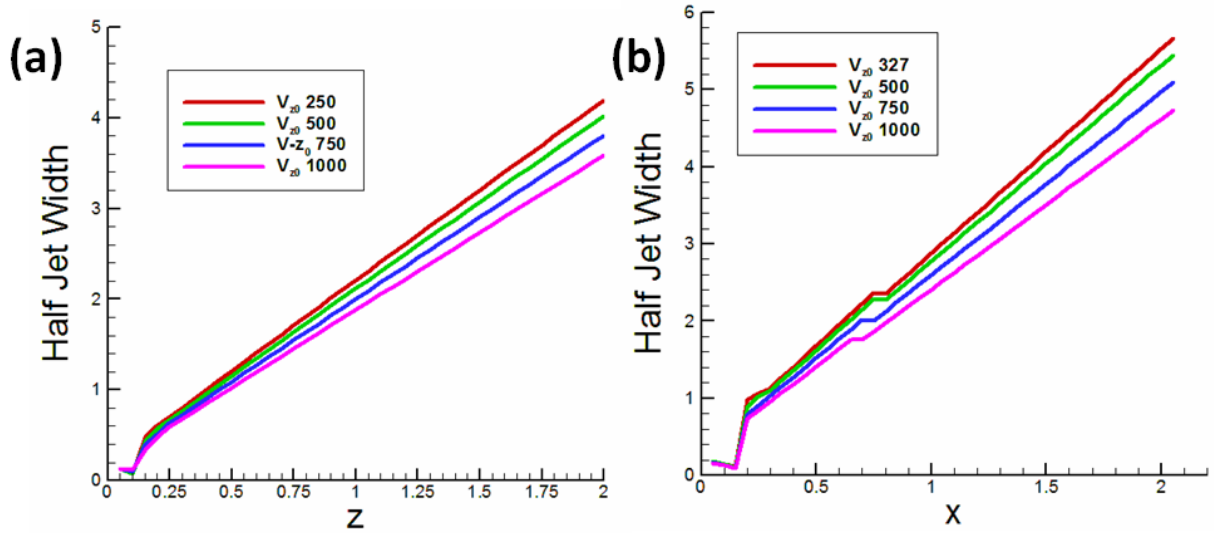


Figure 5.1.11. Variation of the half jet width at different values of the initial foam jet velocity v_{z0} (shown in the insets in cm/s). (a) $Sc=18$, (b) $Sc=30$.

Figure 5.1.11 shows that as the initial foam jet velocity v_{z0} increases, the half-jet width slightly decreases for both values of the Schmidt number. The kinks are determined by a very strong nonlinear dependence of the effective viscosity of slurry with foam on the foam content according to the Ostwald – de Waele power law described in detail in section 3.6.

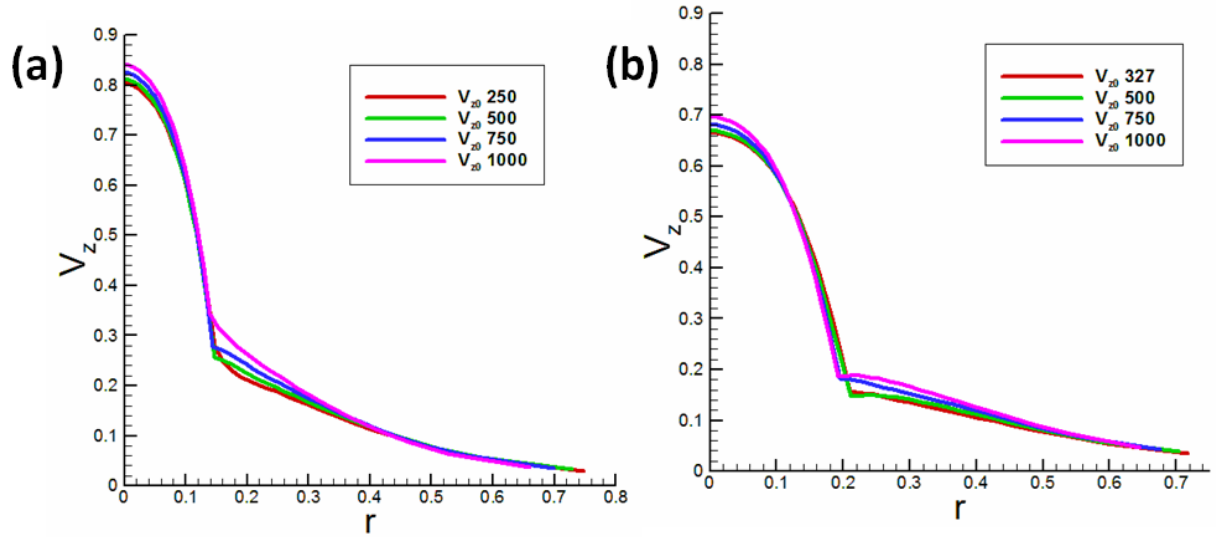


Figure 5.1.12. Longitudinal velocity profiles at different values of the initial foam jet velocity v_{z0} (shown in the insets in cm/s). (a) $Sc=18$, (b) $Sc=30$. The value of $x=0.04$. WSR 68.

Figure 5.1.12 shows the dependence of the profiles of the longitudinal velocity in the jet in a fixed cross-section. As expected, the velocity is maximal at the jet axis $r = 0$ and decreases as the radial distance increases for all values of v_{z0} for both values of the Schmidt number Sc . The kinks in the velocity profiles result from an abrupt increase in the effective viscosity in the outer region when the content approaches that of pure slurry, as well as from a strong nonlinear dependence of the effective viscosity of slurry with foam on the foam content according to the Ostwald – de Waele power law described in detail in section 3.6.

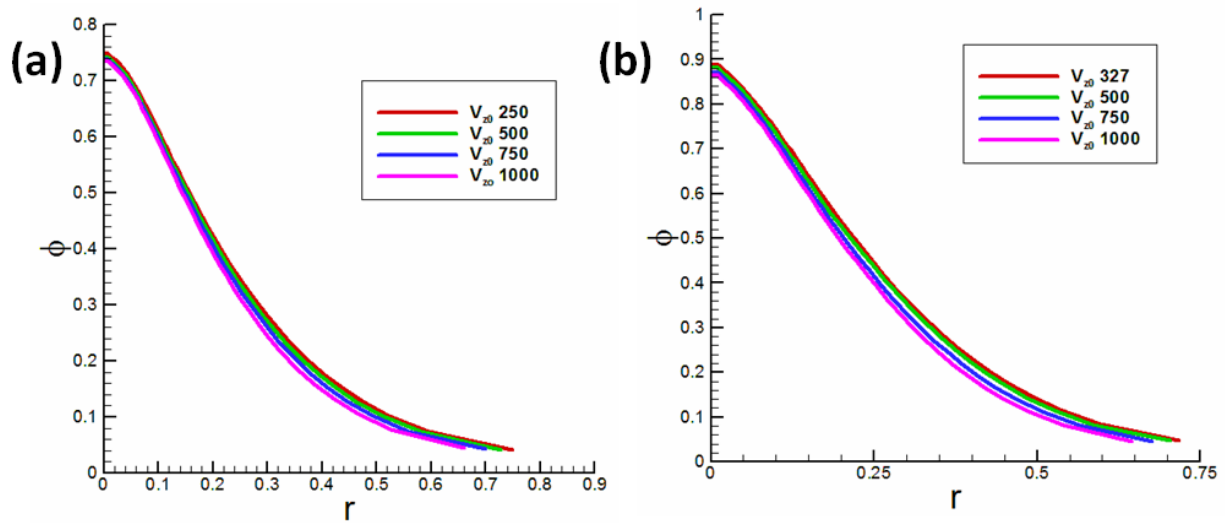


Figure 5.1.13. Dependence of the foam content on the radial coordinate in the jet cross-section predicted at different values of the initial foam jet velocity v_{z0} (shown in the insets in cm/s). (a) $Sc=18$, (b) $Sc=30$. The value of $x=0.04$. WSR 68.

Figure 5.1.13 depicts the profiles of the air/foam content in the same cross-section of the jet at different values of the initial foam jet velocity v_{z0} . It should be emphasized that the results show that the initial velocity of the foam jet has practically no effect on these profiles, i.e. on the rate of foam mixing.

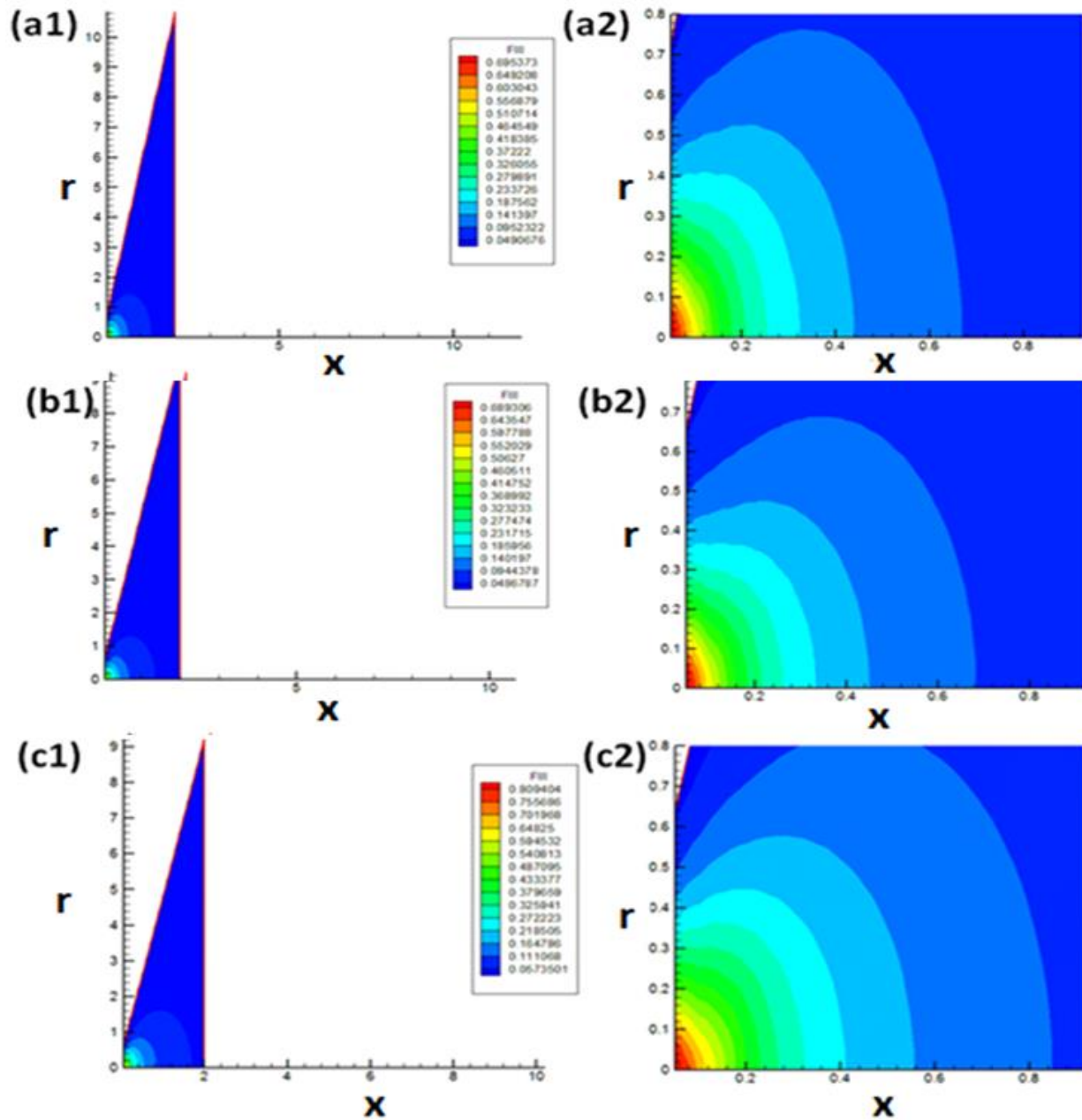


Figure 5.1.14. Foam content in the submerged jet. The panels (a1), (b1) and (c1) show the global views, whereas panels (a2), (b2) and (c2) show the zoomed-in views of the central part of the jet.

Specifically, for panels (a1)-(a2) $v_z=500$ cm/s, $R_0=1.9$ cm, $Sc= 18$; for panels (b1)-(b2) $v_z=1000$ cm/s, $R_0=1.9$ cm, $Sc= 18$; for panels (c1)-(c2) $v_z=1000$ cm/s, $R_0=1.9$ cm, $Sc= 30$. WSR 68.

Figure 5.1.14 compares three fields of foam content in straight submerge foam jets issued into stagnant slurry. Foam spreading and mixing with slurry is a strongly nonlinear process determined by the effective viscosity dependence of the shear rate and foam content. Therefore, a simplistic interpretation of the comparison of the predicted foam content fields is hardly possible, albeit the overall tendency is intuitively clear: the dominant factor is the value of the Schmidt number, which is determined by the value of the diffusion coefficient of foam in slurry. The smaller is the diffusion coefficient (the higher is the Schmidt number), the higher is the axial foam concentration in a given cross-section of the jet, and thus the poorer the mixing process. The effect of the shear stresses on the effective viscosity are much less pronounced, since there is no significant difference between the fields depicted in panels (a) and (b), even though the initial foam jet velocity doubled from (a) to (b). The corresponding longitudinal velocity fields are depicted in Figure 5.1.15.

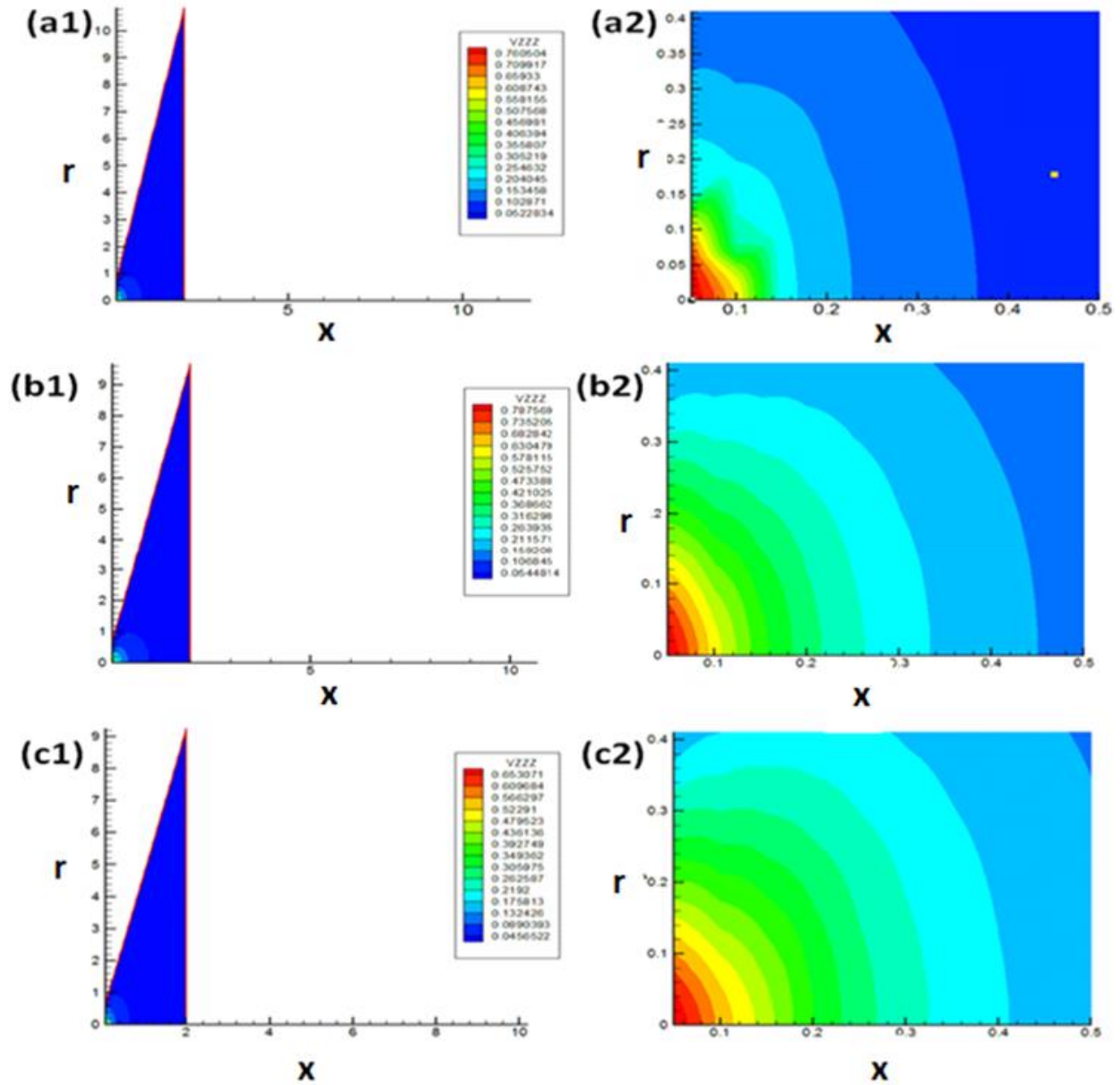


Figure 5.1.15. The longitudinal velocity field in the submerged jet. The panels (a1), (b1) and (c1) show the global views, whereas panels (a2), (b2) and (c2) show the zoomed-in views of the central part of the jet. Specifically, for panels (a1)-(a2) $v_z=500$ cm/s, $R_0=1.9$ cm, $Sc= 18$; for panels (b1)-(b2) $v_z=1000$ cm/s, $R_0=1.9$ cm, $Sc= 18$; for panels (c1)-(c2) $v_z=1000$ cm/s, $R_0=1.9$ cm, $Sc= 30$. WSR 68.

5.2. The effect of WSR: WSR 75 in comparison with the results for WSR 68

The results in the present section compare the predictions for WSR 75 and WSR 68 with all the other parameters being the same, to elucidate the effect of the WSR value on the flow development and foam mixing with slurry. Figure 5.2.1 provides such a comparison for the profiles of the longitudinal velocity in the jet, Figure 5.2.2 – for the profiles of the foam content in the jet, Figure 5.2.3 - for the profiles of the effective viscosity in the jet, and Figure 5.2.4 compares the half widths of the jets at WSR 75 and WSR 68.

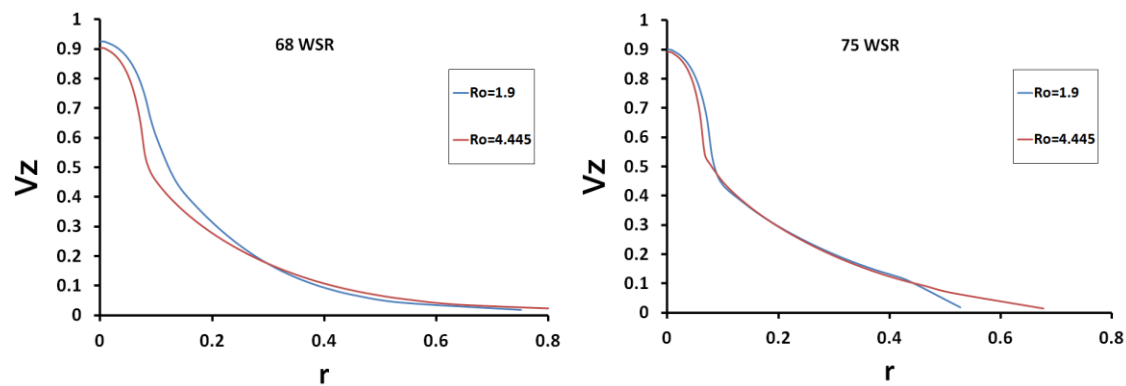


Figure 5.2.1. Longitudinal velocity profiles in the jet for the Schmidt number of $Sc=10$. The value of $x=0.04$. The initial velocity of the foam jet $v_{z0}=500$ cm/s. The results for WSR 68 are shown in the left panel, and for WSR 75-in the right panel.

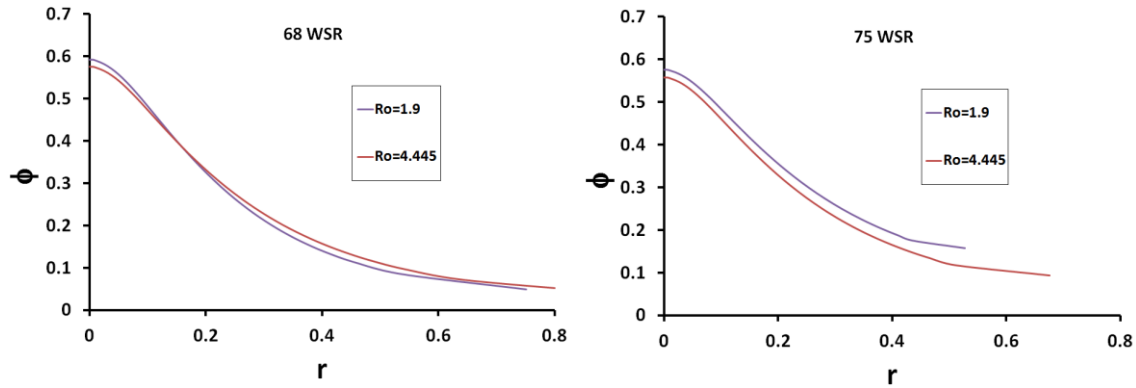


Figure 5.2.2. Foam content profiles in the jet for the Schmidt number of $Sc=10$. The value of $x=0.04$. The initial velocity of the foam jet $v_{z0}=500$ cm/s. The results for WSR 68 are shown in the left panel, and for WSR 75-in the right panel.

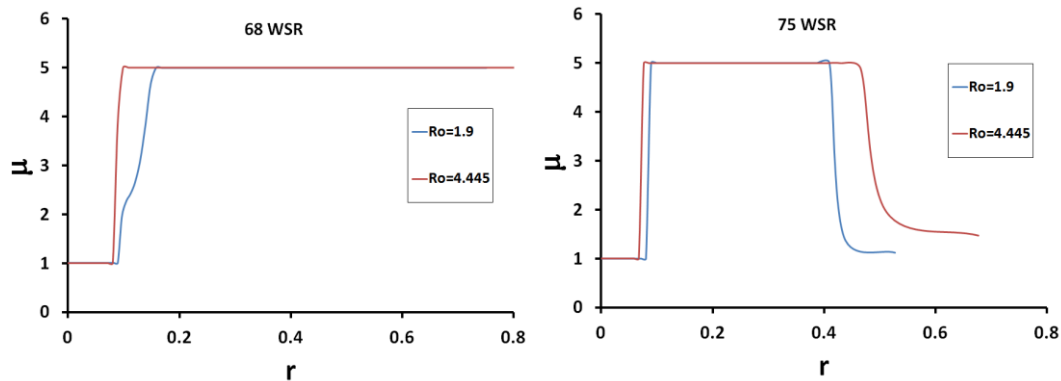


Figure 5.2.3. The effective viscosity profiles in the jet for the Schmidt number of $Sc=10$. The value of $x=0.04$. The initial velocity of the foam jet $v_{z0}=500$ cm/s. The results for WSR 68 are shown in the left panel, and for WSR 75-in the right panel.

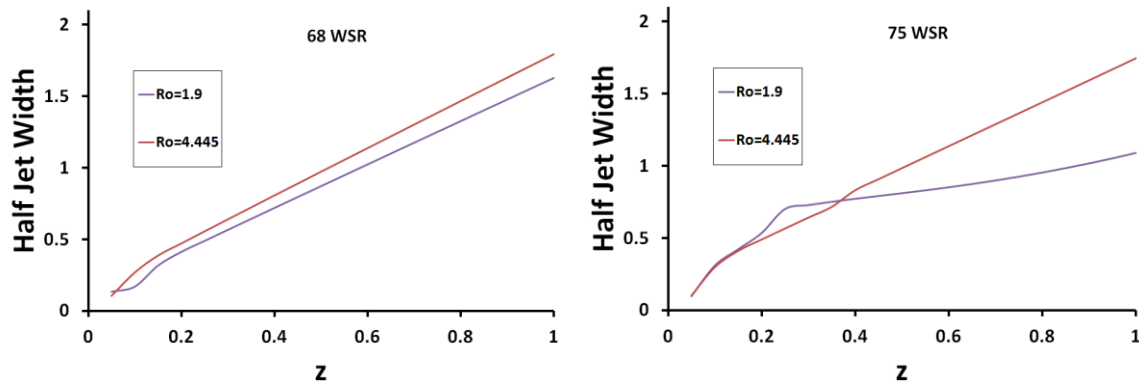


Figure 5.2.4. Half-widths of the jet for the Schmidt number of $Sc=10$. The initial velocity of the foam jet $v_{z0}=500$ cm/s. The results for WSR 68 are shown in the left panel, and for WSR 75-in the right panel.

The next set of comparisons of the results with WSR 75 and WSR 68 is presented in Figures 5.2.5-5.2.8. In distinction from Figures 5.1.2-5.1.4 where the initial foam jet velocity v_{z0} was fixed but the nozzle radius R_0 varied, in Figures 5.2.5-5.2.8 the nozzle radius R_0 is fixed, while the initial foam jet velocity v_{z0} varies. It should be emphasized that Figures 5.2.2 and 5.2.6 reveal that foam mixing at WSR 75 is more efficient than at WSR 68. Indeed, the axial (at $r=0$) values of ϕ in the former case are lower than in the latter one.

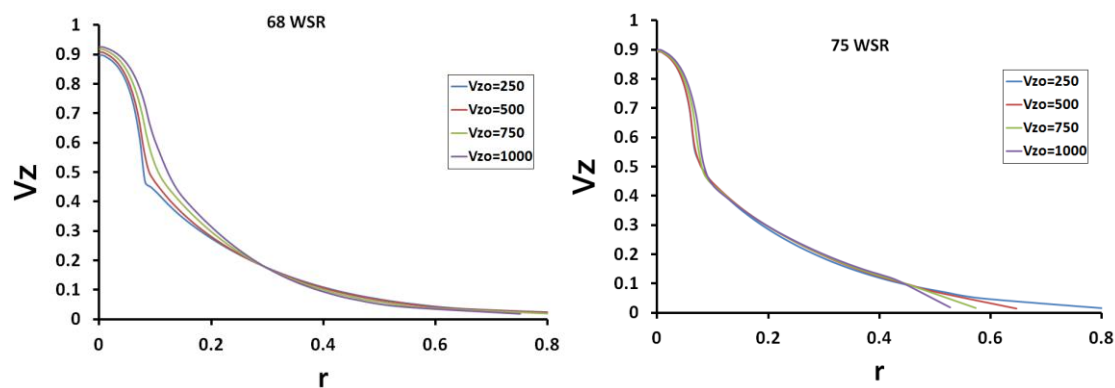


Figure 5.2.5. Longitudinal velocity profiles in the jet for the Schmidt number of $Sc=10$. The value of $x=0.04$. The radius the nozzle issuing the jet was $R_0=1.9$ cm. The results for WSR 68 are shown in the left panel, and for WSR 75-in the right panel.

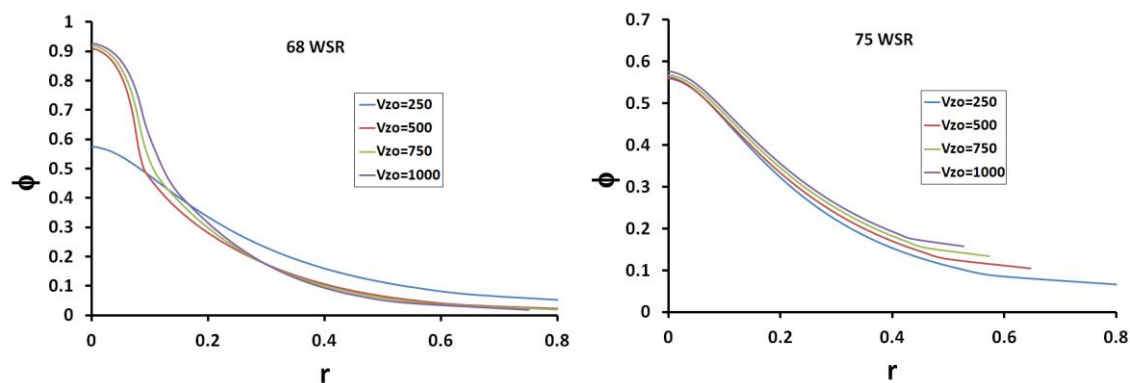


Figure 5.2.6. Foam content in the jet for the Schmidt number of $Sc=10$. The value of $x=0.04$. The radius the nozzle issuing the jet was $R_0=1.9$ cm. The results for WSR 68 are shown in the left panel, and for WSR 75-in the right panel.

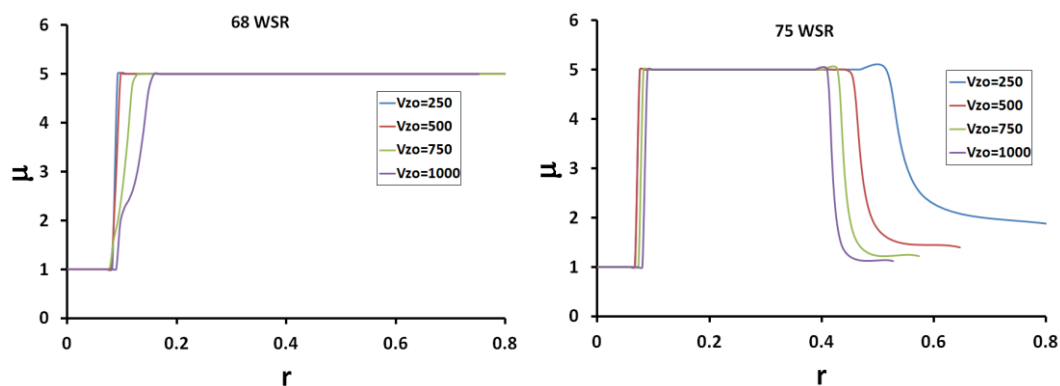


Figure 5.2.7. The effective viscosity profiles in the jet for the Schmidt number of $Sc=10$. The value of $x=0.04$. The radius the nozzle issuing the jet was $R_0=1.9$ cm. The results for WSR 68 are shown in the left panel, and for WSR 75-in the right panel.

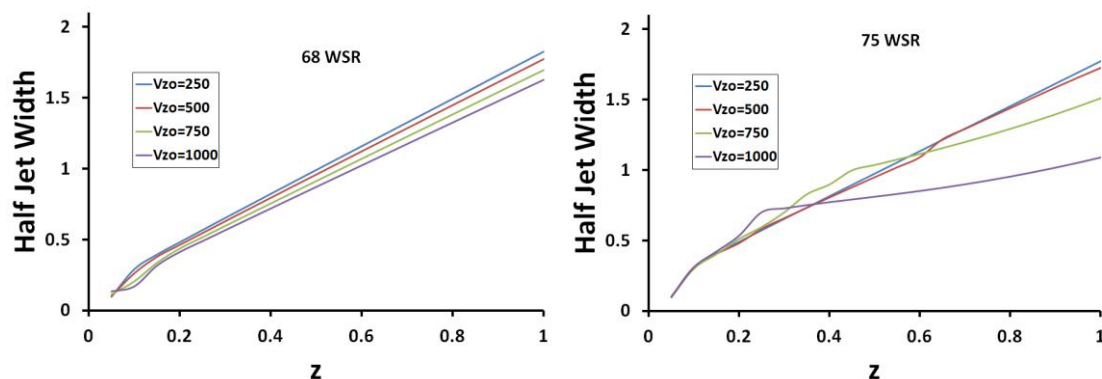


Figure 5.2.8. Half-widths of the jets. The Schmidt number of $Sc=10$. The radius the nozzle issuing the jet was $R_0=1.9$ cm. The results for WSR 68 are shown in the left panel, and for WSR 75-in the right panel.

The pairwise comparisons of the results for WSR 75 and WSR 68 in the same nels are shown in Figures 5.2.9-5.2.11. In particular, Figure 5.2.9 depicts the longitudinal velocity profiles and the foam content profiles in the two types of jets. As mentioned before, the foam mixing in the WSR 75 jet is more effective, because the axial value of ϕ is reduced in this case, while the foam content in the outer region of the jet is higher, which means that more foam has proliferated outwards (see Figure 5.2.9, right panel). Figure 5.2.10 shows the corresponding profiles of the effective viscosity in the jets. It is interesting to note that the effective viscosity in the WSR 75 jet sharply drops in the outer area of the jet. This is explained by the foam proliferation into that area, which diminishes the effective viscosity. On the contrary, the WSR 68 jet has a high-viscosity plateau in the outer region, which means that it still consists there from pure slurry. The half-widths of the jets at WSR 75 and WSR 68 are shown in Figure 5.2.11.

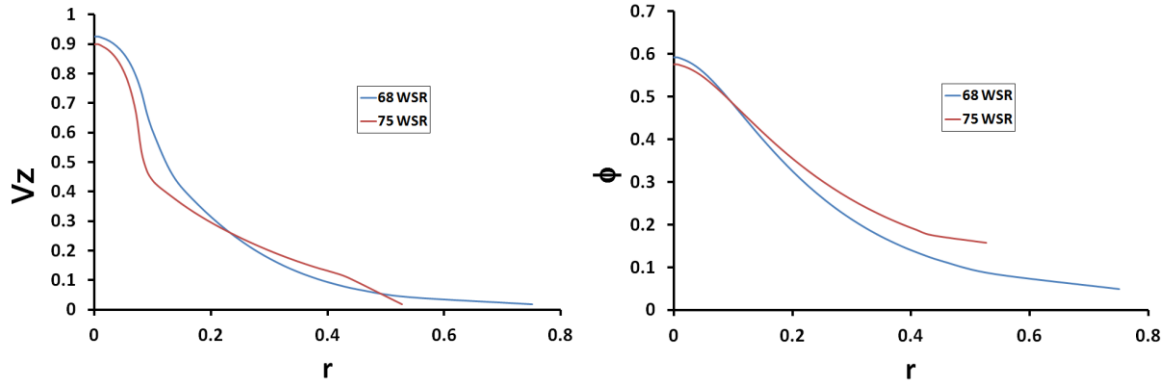


Figure 5.2.9. Longitudinal velocity profiles (left) and the foam content profiles (right) in the jet for the Schmidt number of $Sc=10$. The value of $x=0.04$. The radius the nozzle issuing the jet was $R_0=1.9$ cm.

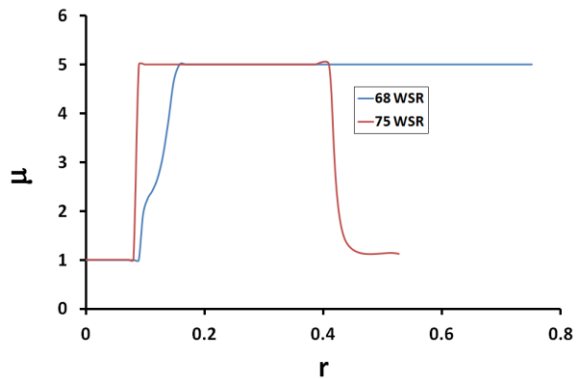


Figure 5.2.10. The effective viscosity profiles in the jet for the Schmidt number of $Sc=10$. The value of $x=0.04$. The radius the nozzle issuing the jet was $R_0=1.9$ cm.

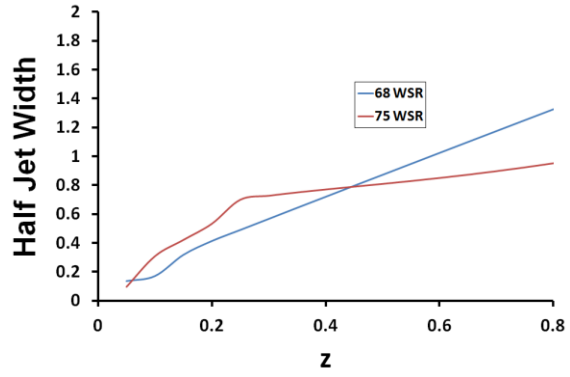


Figure 5.2.11. Half-widths of the jets. The Schmidt number of $Sc=10$. The radius the nozzle issuing the jet was $R_0=1.9$ cm.

6. FOAM JET ISSUED IN CROSS-FLOW OF SLURRY

6.0. Introduction

This Chapter is devoted to foam injection under different conditions into flowing gypsum slurry. In particular, the effects of foam injection angle, velocity of slurry flow, the Schmidt number and water stucco ratio (WSR) are elucidated.

6.1. Governing Equations for the Foam Jet in Cross-Flow of Slurry

Consider a foam jet issued into a cross-flow of gypsum slurry. A steady-state laminar flow evolves into a thin jet which can be treated in the boundary layer approximation (Prandtl 1952, Loitsyanskii 1966, Schlichting 1968, van Dyke 1964). This means, in particular, that pressure field in the jet can be considered to be uniform, and the jet is thin enough to admit transformation of the elliptic equations into the parabolic ones, of the boundary layer type. The sketch of the flow is shown in Figure 6.1.1.

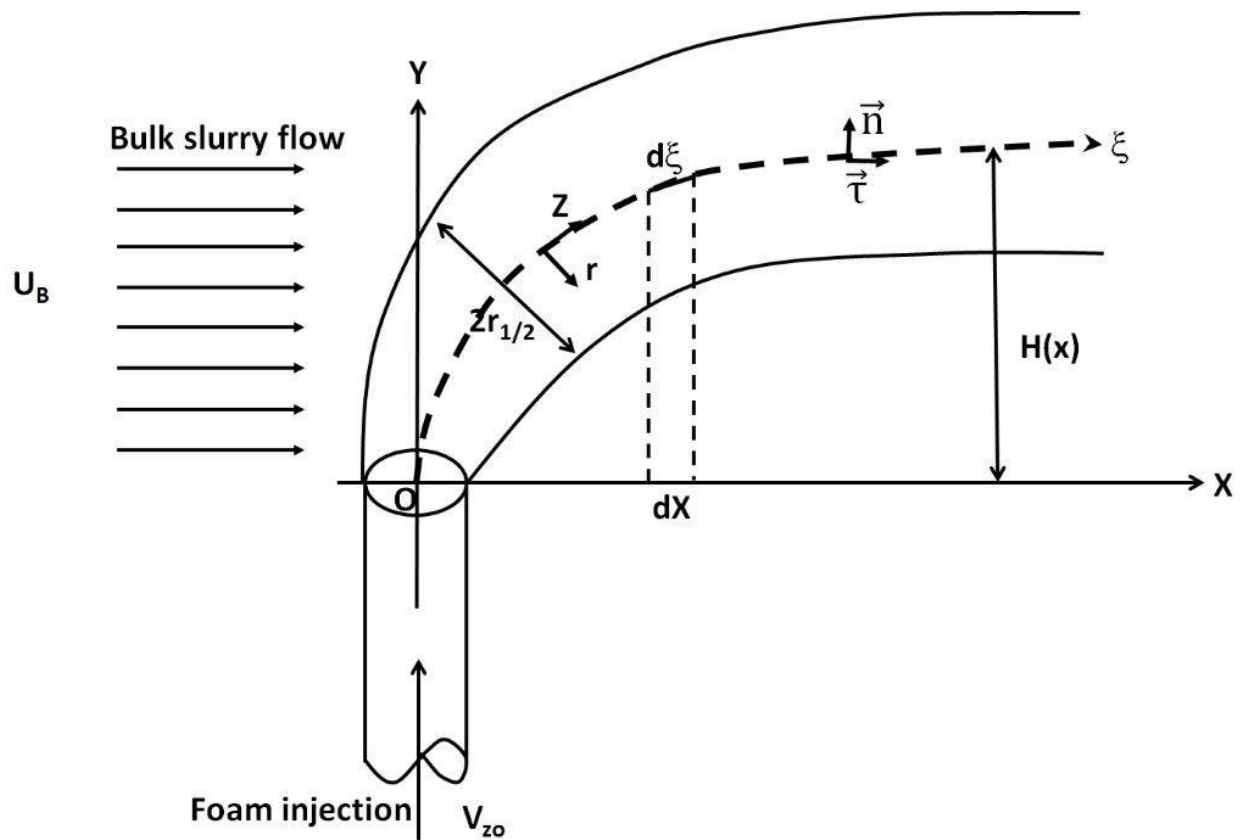


Figure 6.1.1. Sketch of foam jet issued in cross-flow of slurry.

The velocity of the bulk flow of slurry unperturbed by the jet is assumed to be uniform and directed parallel to the Ox axis in Figure 6.1.1

$$\mathbf{U} = U_B \mathbf{i} \quad (6.1.1)$$

where \mathbf{U} is the unperturbed slurry velocity vector, U_B is its magnitude, and \mathbf{i} is the unit vector of the Ox direction.

To derive the overall equation of foam jet in cross-flow, consider the momentum flux \mathbf{M} carried by the jet

$$\mathbf{M} = \boldsymbol{\tau} \int_0^{\infty} \rho v_z^2 2\pi r dr \quad (6.1.2)$$

where $\boldsymbol{\tau}$ is the unit tangent vector of the curved jet axis, ρ is the local density of the foam-slurry mixture, v_z is the flow velocity profile in the jet cross-section, and r is the radial coordinate in the jet cross-section.

It is assumed that the curvature of the jet axis is not large, and the velocity profile can be locally approximated in the first approximation by the one in the corresponding axisymmetric jet considered in the previous Chapters.

The second law of Newton for the jet in cross flow reads

$$\frac{d}{d\xi} \left[2\pi \boldsymbol{\tau} \int_0^{\infty} \rho v_z^2 r dr \right] = \mathbf{F}_D \quad (6.1.3)$$

where ξ is the arc length reckoned along the jet axis, and \mathbf{F}_D is the drag force acting on a unit length of the jet.

The axis of the jet in cross-flow depicted in Figure 6.1.1 is a planar curve. Therefore, according to the Frenet-Serret formula of the differential geometry (Korn & Korn 2000)

$$\frac{d\boldsymbol{\tau}}{d\xi} = \mathbf{n}k \quad (6.1.4)$$

where k is the curvature axis and \mathbf{n} is the unit normal to the jet axis.

Differentiating the in the left-had-side of Eq. (6.1.3) and using Eq. (6.1.4), one arrives at the following equation

$$\frac{\boldsymbol{\tau}}{\lambda} \frac{d}{dX} \left[\int_0^{\infty} \rho v_z^2 r dr \right] + \mathbf{n}k \int_0^{\infty} \rho v_z^2 r dr = \frac{\mathbf{F}_D}{2\pi} \quad (6.1.5)$$

where the jet stretching factor is

$$\lambda = \sqrt{1 + \left(\frac{dH}{dX}\right)^2} \quad (6.1.6)$$

and the curvature is expressed as

$$k = \frac{d^2H/dX^2}{\left[1 + (dH/dX)^2\right]^{3/2}} \quad (6.1.7)$$

In Eqs. (6.1.6) and (6.1.7) $H=H(X)$ is the shape of the jet axis (see Figure 6.1.1).

Projecting Eq. (6.1.5) onto the normal direction, one obtains

$$k \int_0^\infty \rho v_z^2 r dr = \frac{\mathbf{F}_D \cdot \mathbf{n}}{2\pi} \quad (6.1.8)$$

which yields after substituting Eq. (6.1.7), the following equation

$$\frac{d^2H/dX^2}{\left[1 + (dH/dX)^2\right]^{3/2}} \int_0^\infty \rho v_z^2 r dr = \frac{\mathbf{F}_D \cdot \mathbf{n}}{2\pi} \quad (6.1.9)$$

The drag force acting on the jet can be approximated using the drag coefficient C_D as

$$\mathbf{F}_D = \frac{C_D}{2} \rho_s (\mathbf{U} - v_{z,\max} \boldsymbol{\tau}) |\mathbf{U} - v_{z,\max} \boldsymbol{\tau}| 2r_{1/2} \quad (6.1.10)$$

where $r_{1/2}$ is the equivalent radius of the jet, ρ_s is the slurry density, and $v_{z,\max}$ is the maximal velocity in the jet cross-section (the axial velocity).

Figure 6.1.1 shows that

$$\mathbf{i} = \boldsymbol{\tau} \cos \alpha - \mathbf{n} \sin \alpha \quad (6.1.11)$$

where the angle α is defined by the following geometric relation

$$\cos \alpha = \frac{1}{\sqrt{1 + (dH/dX)^2}} \quad (6.1.12)$$

Then, Eqs. (6.1.1) and (6.1.12) yield

$$\mathbf{U} = U_B [\boldsymbol{\tau} \cos \alpha - \mathbf{n} \sin \alpha] \quad (6.1.13)$$

Using Eq. (6.1.13), one obtains for the relative velocity in the expression for the drag force Eq. (6.1.10)

$$\mathbf{U} - v_{z,\max} \boldsymbol{\tau} = (U_B \cos \alpha - v_{z,\max}) \boldsymbol{\tau} - U_B \mathbf{n} \sin \alpha \quad (6.1.14)$$

Accordingly,

$$|\mathbf{U} - v_z \boldsymbol{\tau}| = \sqrt{U_B^2 - 2U_B v_{z,\max} \cos \alpha + v_{z,\max}^2} \quad (6.1.15)$$

Combining Eqs. (6.1.10), (6.1.14) and (6.1.15), one obtains that

$$\mathbf{F}_D = \frac{C_D}{2} \rho_s [(U_B \cos \alpha - v_{z,\max}) \boldsymbol{\tau} - U_B \mathbf{n} \sin \alpha] \sqrt{U_B^2 - 2U_B v_{z,\max} \cos \alpha + v_{z,\max}^2} 2r_{1/2} \quad (6.1.16)$$

Therefore,

$$\mathbf{F}_D \cdot \mathbf{n} = -\frac{C_D}{2} \rho_s U_B^2 \sin \alpha \sqrt{1 - 2 \frac{v_{z,\max}}{U_B} \cos \alpha + \left(\frac{v_{z,\max}}{U_B}\right)^2} 2r_{1/2} \quad (6.1.17)$$

Using Eqs. (6.1.12) and (6.1.17), the dynamic equation (6.1.9) can be recast as a system of two ordinary differential equations

$$\frac{dH}{dX} = f \quad (6.1.18)$$

$$\frac{df}{dX} = -\frac{C_D}{2} \rho_s U_B^2 (1+f^2) f \frac{\sqrt{1 - 2(v_{z,\max}/U_B)/\sqrt{1+f^2} + (v_{z,\max}/U_B)^2}}{2\pi \int_0^\infty \rho v_z^2 r dr} 2r_{1/2} \quad (6.1.19)$$

Solutions of the system (6.1.18) and (6.1.19) are subjected to the following boundary conditions

$$X = 0, \quad H = 0 \quad (6.1.20)$$

$$X = 0, \quad f = \tan \alpha_0 \quad (6.1.21)$$

where α_0 is the initial angle of inclination of the foam jet axis when it is injected into cross-flow.

Render the problem (6.1.18)-(6.1.21) dimensionless using the following scales: the initial velocity of the foam jet at the injection cross-section v_{z0} – for v_z , $v_{z,\max}$ and U_B , the initial radius of the foam jet at the injection cross-section r_0 – for X , H , r and $r_{1/2}$, density of the foam jet in the injection cross-section ρ_0 – for ρ_s . Note that the tangent of the jet axis slope $f = \tan \alpha = dH/dX$ (see Figure 6.1.2) is dimensionless by its definition, Eq. (6.1.18).

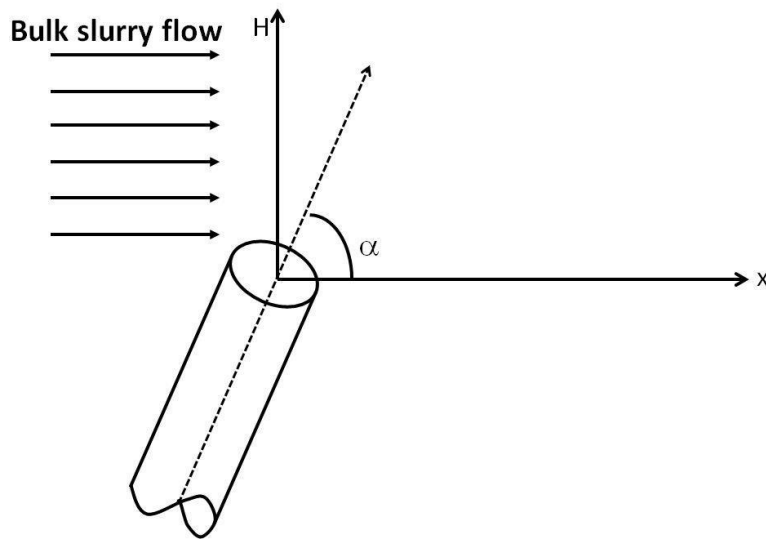


Figure 6.1.2. The jet axis slope.

In the following dimensionless equations overbars over all the dimensionless parameters are omitted for brevity. Then, the dimensionless analog of the problem (6.1.18)-(6.1.21) takes the form

$$\frac{dH}{dX} = f \quad (6.1.22)$$

$$\frac{df}{dX} = -\frac{C_D}{2} \frac{\rho_s}{\rho_0} U_B^2 (1+f^2) f \frac{\sqrt{1-2(v_{z,\max}/U_B)/\sqrt{1+f^2} + (v_{z,\max}/U_B)^2}}{2\pi \int_0^\infty \rho v_z^2 r dr} 2r_{1/2} \quad (6.1.23)$$

$$X=0, \quad H=0 \quad (6.1.24)$$

$$X=0, \quad f = \tan \alpha_0, \quad \text{for } 0 < \alpha_0 < \frac{\pi}{2} \quad (6.1.25)$$

The case of $\alpha_0=\pi/2$ is a singular case. It requires a special asymptotic consideration.

Namely, Eq. (6.1.23) takes the following asymptotic form in the case of small X and Z

$$\frac{df}{dZ} = -C_D \frac{\rho_s}{\rho_0} U_B^2 \frac{\sqrt{1+(1/U_B)^2}}{1/2} f^2 = -2f^2 \frac{\rho_s}{\rho_0} C_D U_B \sqrt{U_B^2+1} \quad (6.1.26)$$

where use has been done of the fact that

$$Z = \int_0^X \sqrt{1 + \left(\frac{dH}{dX}\right)^2} dX \quad (6.1.27)$$

and thus

$$\frac{dX}{dZ} = \frac{1}{\sqrt{1+f^2}} \quad (6.1.28)$$

Equation (6.1.26) also uses the fact that in the initial cross-section of the foam jet the dimensionless integral

$$\int_0^{\infty} \rho v_z^2 r dr = \frac{1}{2} \quad (6.1.29)$$

and

$$r_{1/2} = 1 \quad (6.1.30)$$

Note that in the case of $\alpha_0 = \pi/2$, according to Eq. (6.1.25) in the initial cross-section of the jet $f = \infty$. Therefore, Eqs. (6.1.23), (6.1.28)-(6.1.30) reduced to the asymptotic form (6.1.26) valid at the very beginning of the foam jet in this case.

Denote

$$A = \frac{1}{\pi} \frac{\rho_s}{\rho_0} C_D U_B \sqrt{U_B^2 + 1} \quad (6.1.31)$$

Then, Eq. (6.1.26) takes the following form

$$\frac{dF}{dZ} = -AF^2 \quad (6.1.32)$$

The latter equation is integrated as

$$-\frac{1}{f} = -AZ + \text{const} \quad (6.1.33)$$

Note that at $Z=0$,

$$f = \infty \quad (6.1.34)$$

and thus the integration constant in Eq. (6.1.33) is zero. Then, Eq. (6.1.33) yields the asymptotic behavior of f as

$$f = \frac{1}{AZ} \quad (6.1.35)$$

This asymptotic expression allows one to shift the boundary conditions in the singular case of $\alpha_0 = \pi/2$ to the following ones at a certain small $Z = Z_0 \ll 1$

$$Z = Z_0, \quad H = Z_0 \quad (6.1.36)$$

$$Z = Z_0, \quad f = \frac{1}{AZ_0} \quad (6.1.37)$$

Note that Eq. (6.1.36) follows from the fact that as Eqs. (6.1.22) and (6.1.28) show, in the asymptotical case under consideration $dH/dZ = f/f = 1$, and thus $H = Z$ at the beginning of the jet issued with $\alpha_0 = \pi/2$, i.e. normally to slurry cross-flow. Then, the boundary conditions (6.1.24) and (6.1.25) of the case $0 < \alpha_0 < \pi/2$ are replaced by the boundary conditions (6.1.36) and (6.1.37) in the case $\alpha_0 = \pi/2$.

The corresponding FORTRAN code was developed to describe foam jets issued into slurry cross-flow. It is listed in Appendix 2.

6.2. Results and Discussion

The present section discusses the results of the numerical solution of the problem (6.1.22) and (6.1.23) with the boundary conditions (6.1.24) and (6.1.25) in the case $0 < \alpha_0 < \pi/2$, or with the boundary conditions (6.1.36) and (6.1.37) in the case of $\alpha_0 = \pi/2$, supplemented with the

numerical solution of the problem (4.2.9) and (4.2.10) used to find the velocity and density distribution along the jet. Several basic parameters governing the flow in the foam jet or in the slurry cross-flow are varied and the corresponding parameters of the jet, especially the shape of its centerline, are predicted.

6.3. Results and Discussion

Normal Injection of Foam into Slurry Cross-flow: The Effect of the Cross-Flow Velocity at the Schmidt Number $Sc=18$

This subsection is devoted to the results of the numerical simulations of foam jets injected into slurry cross-flow in the case of the Schmidt number $Sc=18$ at different value of the cross-flow velocity U_B . Two water-to-slurry ratio (WSR) values of 68 and 75 are considered and the cross-flow velocity is varied in a wide range. The case of the normal injection of the foam jet is considered in all the case, i.e. $\alpha_0=\pi/2$ and the boundary conditions given by Eqs. (5.1.36) and (6.1.37). Figure 6.3.1 compares the results for WSR 75 (the left-hand side columns) with those for WSR 68 (the right-hand side columns). Panels (a1) and (a2) in Figure 6.3.1 depict the results for the foam concentration at the jet axis ϕ_1 along its arc length for several dimensionless cross-flow velocities of the slurry: from $U_B=0.1$ to $U_B=10$. The results show that at the beginning of all jets the foam concentration at the jet axis dramatically decreases, which manifests the fact that mixing of foam with slurry is very intensive when the angle of inclination of the foam jet to the slurry cross-flow is large, i.e. the foam mixing is mostly convective in that part of the jet. On the other hand, in the case of WSR 75 where water content is higher than in the case of WSR 68, the foam concentration at the jet axis ϕ_1 relatively rapidly plateaus and then even begins to increase.

This phenomenon is related to the fact that convective mixing of dilute slurry flux with foam ceases more rapidly in the intermediate part of the jets in the case of lower gradients of the effective viscosity, the jets mostly turn to the cross-flow direction faster (see panel c1 in Fig. 6.3.1). Then, the situation arises where a still slower moving foam jets become surrounded by a faster moving slurry. As a result, the cross-sections of the foam jets contract, the foam axial concentration begins to increase, and the axial velocity of the foam jet v_{z1} also begins to increase, as is seen in panel (b1) in Fig. 6.3.1.

Comparing the results for the case of WST 68 in the right-hand side column in Fig. 6.3.1, one can see that neither the axial foam concentration ϕ_1 , nor the axial foam velocity v_{z1} increase along the jet. This is because the viscosity gradients are so high in this case that the foam jet is continuously “teared” by the surrounding slurry, which facilitates convective mixing. As a result, under the conditions of the continuous convective mixing the axial foam concentration ϕ_1 and the axial foam velocity v_{z1} continue to decrease monotonously along the jet arc length

Figure 6.3.1 shows that for both WSR values, the higher the bulk slurry velocity, U_B , the faster the foam jet turns direction. This effect results from a higher drag force acting on a foam jet from the slurry side at higher values of U_B .

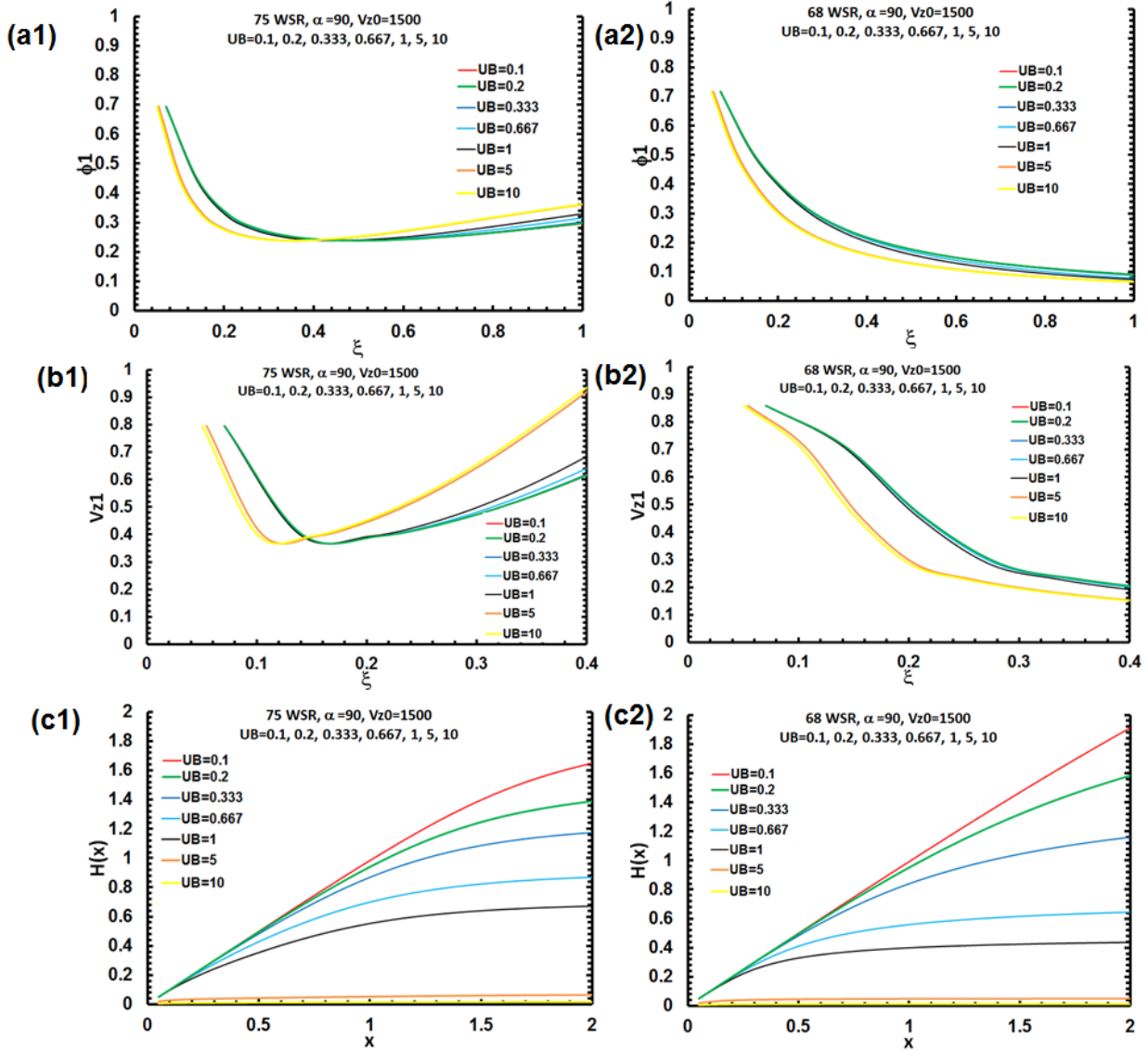


Figure 6.3.1. The foam jet characteristics for two values of the water-to-slurry ratio (WSR): WSR 75 (the left-hand side columns, i.e. panels with numerals “1”) and WSR 68 (the right-hand side columns, i.e. panels with numerals “2”) in the case of the normal injection of the foam jet, i.e. $\alpha_0 = \pi/2$ at the Schmidt number $Sc = 18$. Panels “a” show the variation of air volume fraction along the arc length of the jet. Panels “b” show the variation of the centerline velocity along the arc length of the jet. Panels “c” show shapes of the jet centerline. Different values of the cross-flow velocity U_B shown in the panels correspond to curves of different colors.

Normal Injection of Foam into Slurry Cross-flow: The Effect of the Cross-Flow Velocity at the Schmidt Number $Sc=30$

In this section the same range of the cross-flow velocities U_B is considered, with the value of the Schmidt number being changed. An increase in the Schmidt number from $Sc=18$ to $Sc=30$ is equivalent to a decrease in the diffusion coefficient of air in slurry. Because of that air/foam spreading in slurry is dramatically suppressed. That, in turn, sustains high viscosity gradients even in the case of WSR 75, As a result the foam jet issued into the WSR 75 slurry experiences a significant “tearing” action from the slurry side. This suppresses several effects observed in the case of $Sc=18$ in the previous section, namely, the increase in the axial foam concentration ϕ_1 and the axial foam velocity v_{z1} in the intermediary parts of the jets, as well as makes it more difficult for jets to align with the slurry flow. The results for WSR 75 and WSR 68 become more similar to each other, as Figure 6.3.2 shows.

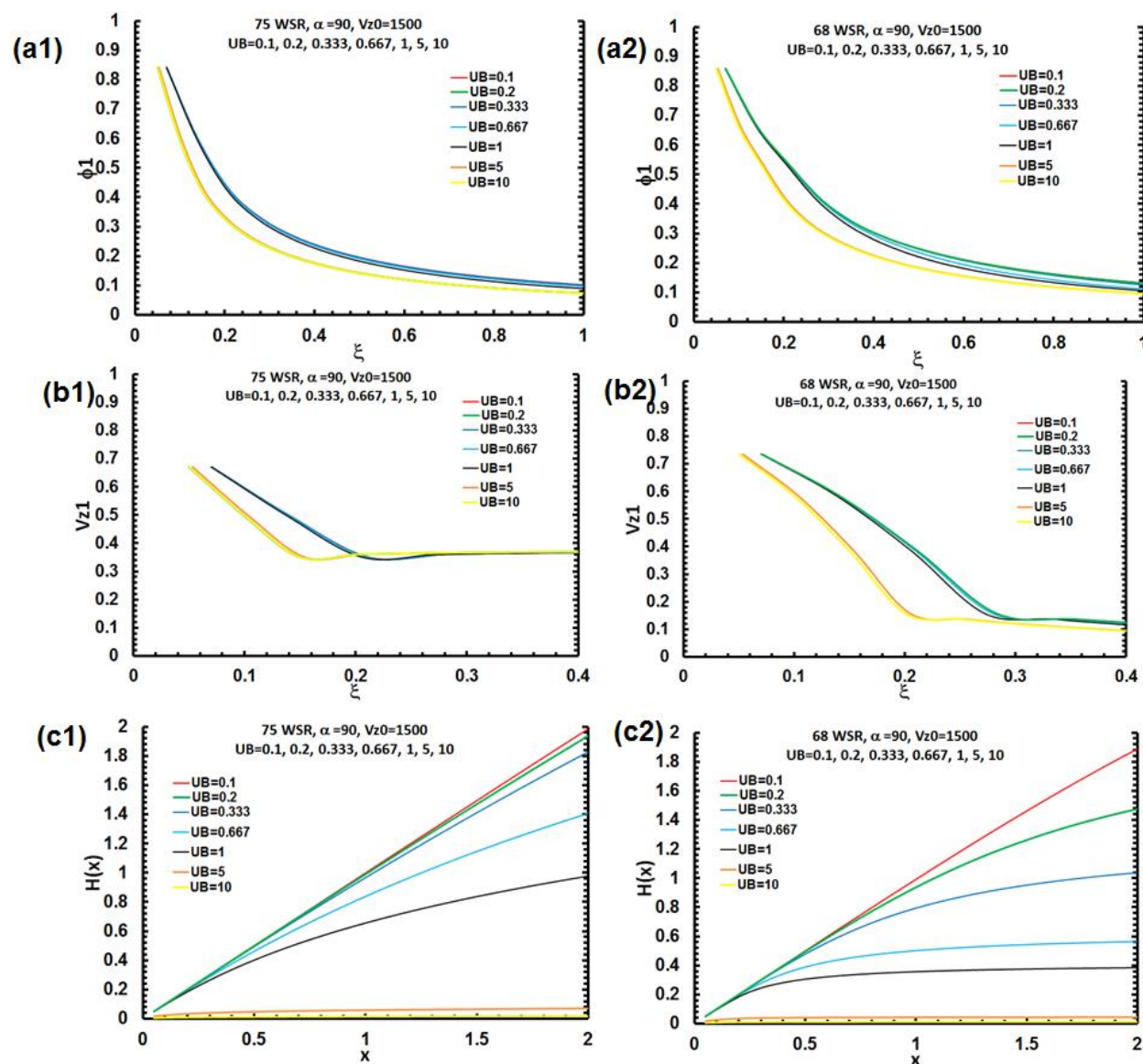


Figure 6.3.2. The foam jet characteristics for two values of the water-to-slurry ratio (WSR): WSR 75 (the left-hand side columns, i.e. panels with numerals “1”) and WSR 68 (the right-hand side columns, i.e. panels with numerals “2”) in the case of the normal injection of the foam jet, i.e. $\alpha_0 = \pi/2$ at the Schmidt number $Sc = 30$. Panels “a” show the variation of air volume fraction along the arc length of the jet. Panels “b” show the variation of the centerline velocity along the arc length of the jet. Panels “c” show shapes of the jet centerline. Different values of the cross-flow velocity U_B shown in the panels correspond to curves of different colors.

In all the cases shown in Figures 6.3.1 and 6.3.2 the faster decrease of the foam concentration at the jet axis ϕ_1 along the jet means a better mixing. Note, however, that this is not achieved only due to a higher diffusion coefficient (a lower Schmidt number) but always due to the interplay with the convective effects.

Effect of Variation of Angle of Foam Injection: The Case of the Schmidt Number $Sc=18$

In Figure 6.3.3 panels (a) show the axial foam concentration ϕ_1 , panels (b) show the shapes of the jet axes, and panels (c) show the axial foam velocity v_{z1} . The most noticeable observations are seen in panels (c) in this figure. Namely, the higher is the injection angle of the foam jet, the longer it takes it to align with the cross-flow. Accordingly, the highest axial concentration of foam corresponds to the jets issued at higher angles of obliquity, i.e. foam mixing is delayed in such jets.

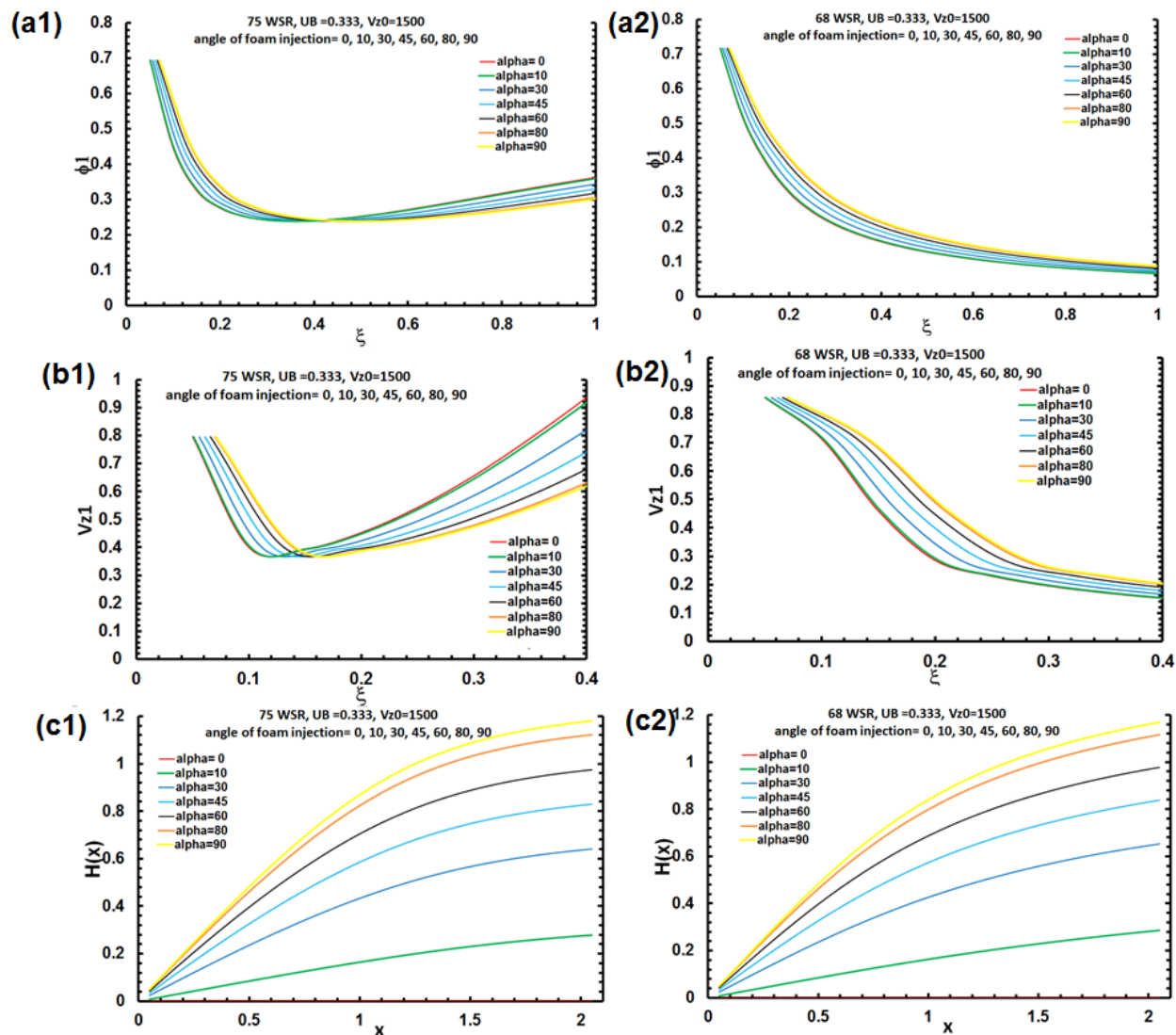


Figure 6.3.3. Effect of variation of the slurry injection angle α on the foam jet flow characteristics for two values of the water-to-slurry ratio (WSR): WSR 75 (the left-hand side columns, i.e. panels with numerals “1”) and WSR 68 (the right-hand side columns, i.e. panels with numerals “2”). The cross-flow velocity $U_B=0.333$. The Schmidt number $Sc=18$. The results for the injection angles $\alpha=0^\circ, 10^\circ, 30^\circ, 45^\circ, 60^\circ, 80^\circ$, and 90° are shown by different colors. The results for $\alpha=90^\circ$ correspond to those in Figure 6.3.1 for $U_B=0.333$.

Effect of Variation of Angle of Foam Injection: The Case of the Schmidt Number 30

The effect of the foam jet obliquity (i.e. its initial angle of inclination relative to the slurry cross-flow) is illustrated in Figure 6.3.4. It resembles that depicted in Figure 6.3.3, i.e. the larger is the initial angle of obliquity, the longer it takes to mix uniformly the foam and the slurry. Note, that this information has direct consequences for design of wallboard production lines, namely, choosing their length scales.

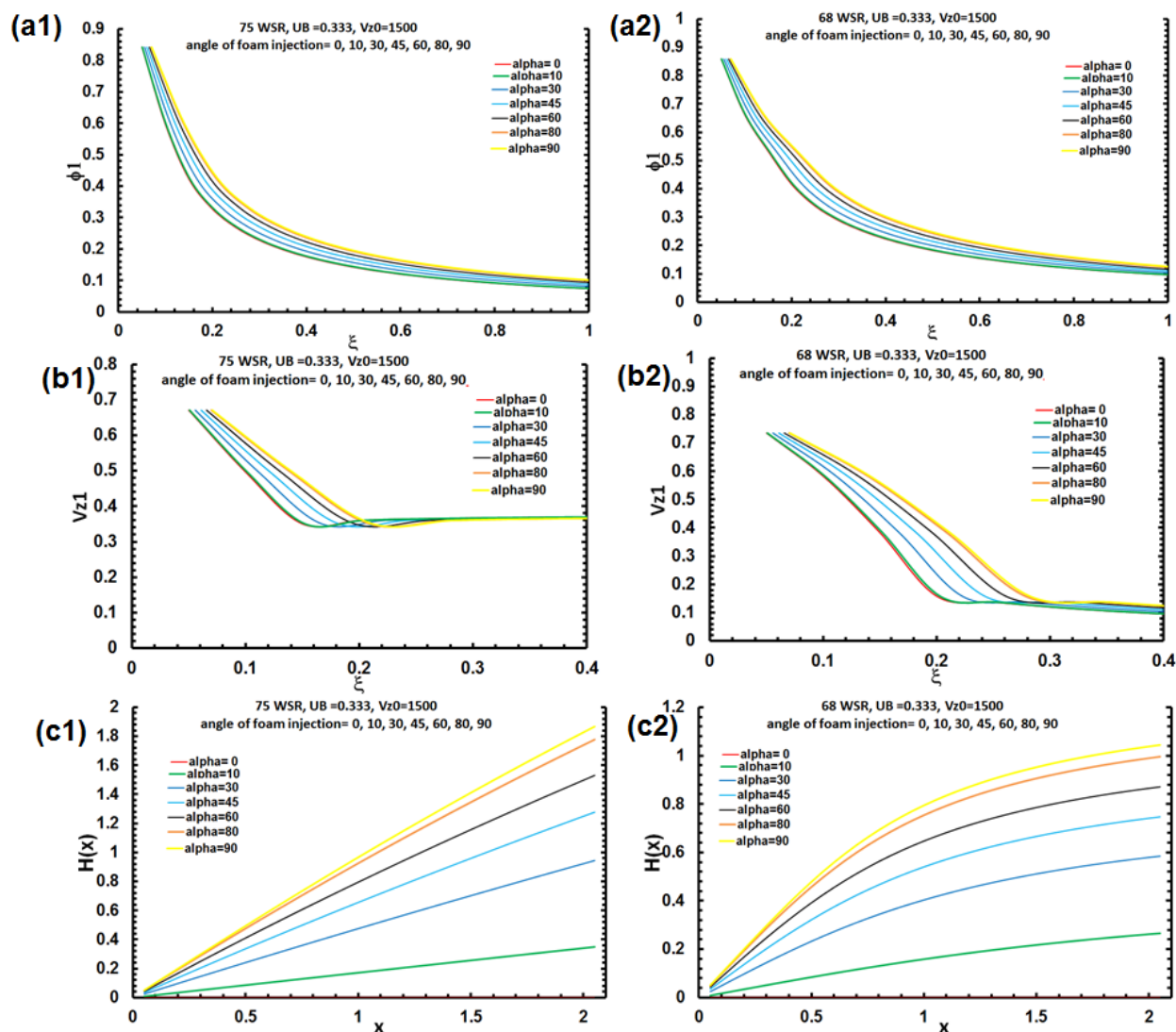


Figure 6.3.4. Effect of variation of the slurry injection angle α on the foam jet flow characteristics for two values of the water-to-slurry ratio (WSR): WSR 75 (the left-hand side

columns, i.e. panels with numerals “1”) and WSR 68 (the right-hand side columns, i.e. panels with numerals “2”). The cross-flow velocity $U_B=0.333$. The Schmidt number $Sc=30$. The results for the injection angles $\alpha=0^\circ, 10^\circ, 30^\circ, 45^\circ, 60^\circ, 80^\circ,$ and 90° are shown by different colors. The results for $\alpha=90^\circ$ correspond to those in Figure 6.3.1 for $U_B=0.333$.

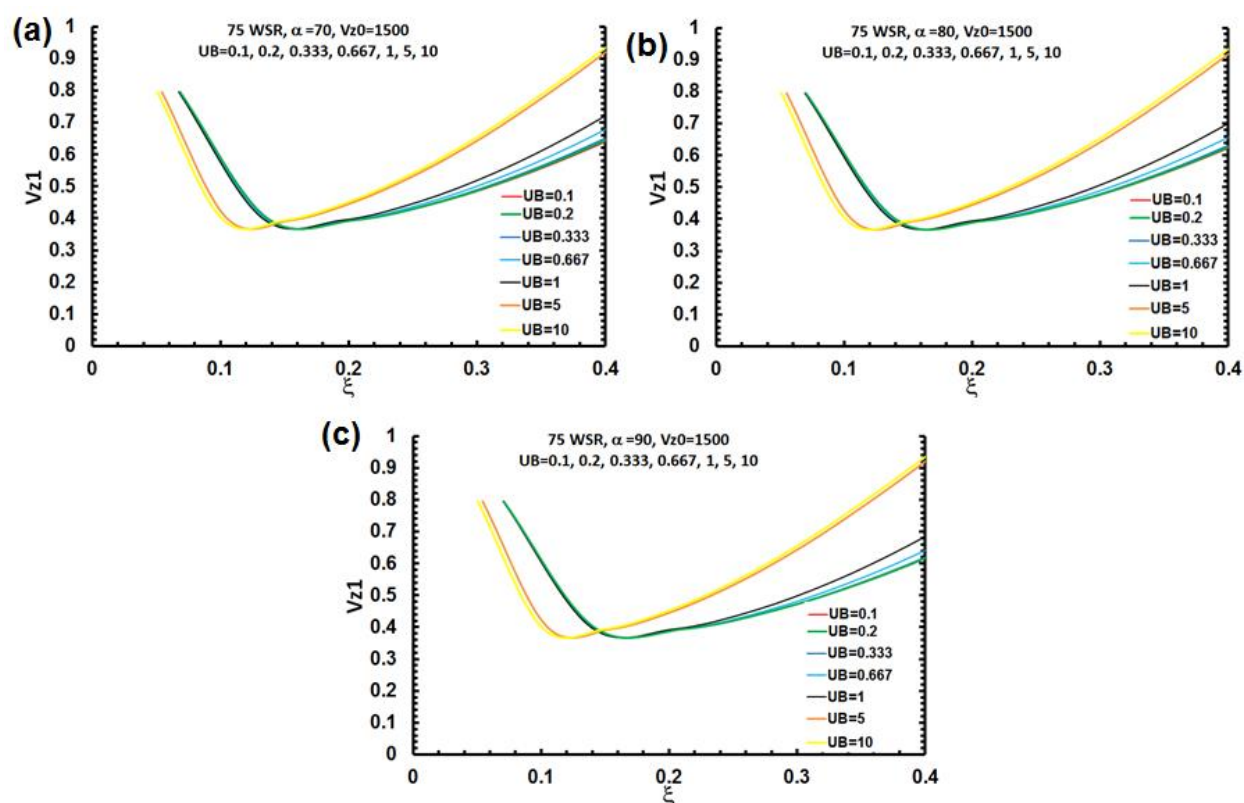


Figure 6.3.5. The foam jet characteristics for WSR 75 (the left-hand side columns, i.e. panels with numerals “1”) and the Schmidt number $Sc=18$ at different values of the cross-flow velocity. The results resolve the situation at the high values of the initial foam jet obliquity. Namely, (a) corresponds to $\alpha=70^\circ$, (b)- to $\alpha=80^\circ$, and (c) - to $\alpha=90^\circ$. All the three panels depict variation of the axial velocity along the jet. Different values of the cross-flow velocity U_B shown in the panels correspond to curves of different colors.

The results for the axial jet velocity along its arc length calculated at high angles of obliquity show insignificant difference between $\alpha=70^\circ$, $\alpha=80^\circ$, and $\alpha=90^\circ$. The results also show that the fastest cross-flows $U_B=5$ and 10, turn the foam jet faster. However, this results in a situation when a slowly moving foam jet is surrounded by a parallel slurry flow which is faster. As a result, the foam jet contracts, and its axial velocity increases.

7. CONCLUSIONS

1. The problem of foam mixing with slurry in the form of the foam jet issued into stagnant slurry or slurry cross-flow was solved in the framework of the boundary layer approach.
2. The unique approach developed in the present work allows one to elucidate the flow field and mixing rate of non-Newtonian power-law straight submerged jets of foam issued into gypsum slurry.
3. A novel coordinate transformation based on the invariant of the foam content along the jet was proposed with the goal to convert the full quadrant, and thus, infinite in the radial direction, integration domain into a finite strip of a constant width equal to the value of the invariant determined by the conditions at the nozzle exit.
4. Based on the new coordinates, a novel numerical method of integration of the governing momentum balance and foam content partial differential equations was developed. The method is based on the semi-discretization of the problem in the lateral direction, and thus reducing it to a system of the interconnected ordinary differential equations. This method is, in fact, a particular case of the so-called method of straight lines. The resulting system of the ordinary differential equations for the values of the longitudinal velocity and foam content was solved using the Kutta-Merson method with an automatic variation of the time step in the marching direction (along the jet).
5. A novel numerical code was written based on the above-mentioned algorithm and used for numerical simulations of the straight foam jets issued into stagnant slurry.

6. Parametric study of the effect of different governing parameters on the mixing rate has been undertaken, and the profiles of the longitudinal velocity, foam content, the effective viscosity, as well as such global parameters as the distribution of the half width along the jet were predicted.
7. The results revealed that mixing of foam in a straight jet is significantly affected by the value of the Schmidt number (namely, the diffusion coefficient of foam in slurry). The smaller is the diffusion coefficient (the higher is the Schmidt number), the weaker is foam mixing.
8. The results also revealed a significant effect of WSR on the foam mixing, with WSR 75 guaranteeing a better way of foam spreading across the jet in comparison with the case of WSR 68.
9. A new method combining the approach based on the boundary layer theory with the approach of the bar bending theory was proposed to describe flow in foam jets issued into slurry cross flow.
10. A novel numerical code was written and used for numerical simulations of the foam jets issued into slurry cross flow.
11. In the case of the foam jet issued into slurry cross-flow the higher cross-flow velocity and the lower obliquity angles resulted in a faster aligning of the foam jet with the main flow of slurry. However, the faster turning and aligning of the foam jet comes with a price. Namely, it appears to be surrounded by a faster moving co-flow, which results in jet contraction, and increase of foam concentration, i.e. in worse mixing.

This is the first study of gypsum slurry and foam mixing starting in the framework of rheology and non-Newtonian fluid mechanics. Such modeling could trigger additional modeling of different stages of wallboard-forming process, where shear-thinning flow behavior is accompanied by solidification, heat release and the internal structure formation. Rigorous description of gypsum slurry flows can be used for the optimization of different stages used in construction industry, as well as it can diminish efforts required in the trial and error approach. The potential outcomes of such improvements would manifest themselves in lower water and energy consumption and a cleaner and “greener” environment.

The present approach may be applied to similar situations in the building products industry such as pulp consistency in paper making, mineral wool and perlite in water-felted ceiling tile basemat. It also can impact the wide range of applications where a foaming agent is injected into a substance to reduce weight, create an internal void structure or change solid properties for end user applications.

CITED LITERATURES

- Alengaram, U J, Al Muhit, B A, Jumaat, M. Z. bin, Jing, M L Y. A comparison of the thermal conductivity of oil palm shell foamed concrete with conventional materials; *Materials and Design*; 2013; 51; 522–29.
- Allesandrini, A, Lapasin, R, Sturzi, F. The kinetics of thixotropic behavior in clay kaolin aqueous suspensions; 1982; *Chem. Eng. Commun.*; 17; 13–22.
- Amirnia, S, de Bruyn, J R, Bergougnou, M A, Margaritis, A. Continuous rise velocity of air bubbles in non-Newtonian biopolymer solutions. *Chemical Engineering Science*; 2013; 94, 60-8.
- Baravian, C, Quemada, D, Parker, A. A new methodology for rheological modelling of thixotropy application to hydrocolloids; 1996; *Proceedings of the XIIth International Congress on Rheology*; 779–780.
- Barnes, H. A. Thixotropy, rheopexy, yield stress. Section C9.2 in *Springer Handbook of Experimental Fluid Mechanics*. (Eds. C. Tropea, A.L. Yarin and J. Foss), Heidelberg 2008.
- Başpınara M S, Kahraman E. Modifications in the properties of gypsum construction element via addition of expanded macroporous silica granules; *Construction and Building Materials*; 2011; 25; 3327-33.
- Batchelor, G.K. *An Introduction to Fluid Dynamics*. Cambridge University Press, Cambridge, 2002.
- Biondo, S.J, Marten, J C. A history of flue gas desulphurization systems since 1850; 1977; *Journal of the Air Pollution Control Association*; 27; 948–61.

CITED LITERATURES

- Bird, R.B., Curtiss, C.F., Armstrong, R.C., Hassager, O. *Dynamics of Polymeric Liquids*, Wiley&Sons, New York, 1987.
- Blackburn, DR, Lu, R, Tracy, SL, Liu, Q, Wittbold, JR, Petersen, BL, Li, A, Fall, JL; Shake, MP, Lee, C. Foamed slurry and building panel made therefrom; 2012, US 8088218 B2
- Bleszynski R, Hooton R D, Thomas M D A, Rogers C A. Durability of ternary blend concrete with silica fume and blast-furnace slag, laboratory and outdoor exposure site studies; *ACI Mater J*; 2002; 99; 499–508.
- Bubnov, V A. Numerical solution of problems pertaining to a submerged jet in power-law fluids. *Journal of Engineering Physics*; 1968; 14; 265-7.
- Cheng ,D C-H, Evans, F. Phenomenological characterization of rheological behaviour of inelastic reversible thixotropic and antithixotropic fluids; 1965;*Brit. J. Appl. Phys.*; 16, 1599–1617.
- Chhabra, R P. *Bubbles, Drops, and Particles in Non-Newtonian Fluids*- Chapter 6, Second Edition; 2006; CRC Press, Boca Raton
- Damtoft J S, Lukasik J, Herfort D, Sorrentino D, Gartner EM. Sustainable development and climate change initiatives; *Cem Concr Res*; 2008; 38; 115–27
- de Kee, D, Code, R, K, Turcotte, G. Flow properties of time-dependent foodstuffs; 1983; *J. Rheol.*; 27; 581–604.
- de Kee, D., Code, R.K., Turcotte G. Flow properties of time-dependent foodstuffs. 1983; *J. Rheol.* ; 27; 581-604.
- Duxson P, Provis J L, Lukey G C, Van Deventer J S J. The role of inorganic polymer technology in the development of ‘green concrete’; *Cem Concr Res*; 2007; 37; 1590–7

CITED LITERATURES

- Dzhaugashtin, K.E., A.L. Yarin, Numerical simulation of non-self-similar wall jet. *J. Engineering Physics*, 32, 420-426 (1977).
- Dzhaugashtin, K.E., A.L. Yarin, Combustion process in laminar homogeneous gas jets. *Combustion, Explosion and Shock Waves*, 14, 321-327 (1978).
- Dzhaugashtin, K.E., A.L. Yarin, Combustion in laminar diffusion gas jets. *Combustion, Explosion and Shock Waves*, 15, 92-95 (1979).
- Dzhaugashtin, K.E., A.L. Yarin, Grazing flame core of unmixed gases. *Combustion, Explosion and Shock Waves*, 17, 283-289 (1981).
- Filip, P., Kolář, V. Hájek, R. Similarity prediction of wall jets past axisymmetric bodies for power-law fluids. *Acta Mechanica*; 1991, 88, 167-73
- Flower D, Sanjayan J. Greenhouse gas emissions due to concrete manufacture; *Int J Life Cycle Assess*; 2007; 12; 282–8.
- Galos, KA, Smakowski, TS, Szlugaj, J. Flue-gas desulphurisation products from Polish coal-fired power-plants; 2002; *Applied Energy*; 75, 257-65
- Gartner E M, Macphee D E. A physico-chemical basis for novel cementitious binders; *Cem Concr Res*; 2011;41:736–49
- Godfrey J C. Ph.D. Thesis, *Characterisation of thixotropic fluids*; University of Bradford; 1983
- Goodeve, C F, Whitfield, G W. The measurement of thixotropy in absolute units; *Trans. Farad. Soc.*; 1938; 34; 511–520
- Gutfinger, C, Shinnar, R. Velocity distribution in two dimensional laminar liquid-into-liquid jets in power law fluids. *AIChE J.*; 1964; 10; 631–35.

CITED LITERATURES

- Hammad, K J. Velocity and momentum decay characteristics of a submerged viscoplastic jet. *J. Fluids Eng.*; 2013; 136; 021205.
- Herrera-Velarde, J R, Zenit, R, Chehata, D, Mena, B. The flow of non-Newtonian fluids around bubbles and its connection to the jump discontinuity. *Journal of Non-Newtonian Fluid Mechanics*; 2003; 111; 199–209.
- Hilal, A A, Thom N H, Dawson A R. On entrained pore size distribution of foamed concrete; *Construction and Building Materials*; 2015; 75; 227–33.
- Jordan, C., Rankin, G.W., Sridhar, K. A study of submerged pseudoplastic laminar jets. *Journal of Non-Newtonian Fluid Mechanics*; 1992; 41, 323-37
- Jun, S. *Transport Phenomena in Multi-phase Media: Slurries, Foams, Boiling Bubbly Media and Pulps*. Thesis submitted as a partial fulfillment of the requirements for the degree of Doctor of Philosophy in Mechanical Engineering in the Graduate College of the University of Illinois at Chicago, 2013.
- Kapur, J N. On the two dimensional jet of an incompressible pseudoplastic fluid. *J. Phys. Soc. Jpn.*; 17; 1962; 1303–9.
- Kawamura T, Nanba K. MIXER, MIXING METHOD, AND METHOD FOR PRODUCING LIGHTWEIGHT GYPSUM BOARD; 2015; WO/2015/093209.
- Korn, G.A. & Korn, T.M. *Mathematical Handbook for Scientists and Engineers: Definitions, Theorems, and Formulas for Reference and Review*. McGraw-Hill, New York, 2000.
- Krämer, C, Schauerte, M, Kowald, T L, Trettin, H F R. Three-phase-foams for foam concrete application; *Materials Characterization* 102 (2015) 173–179.

CITED LITERATURES

- Kumar, K R, Rankin, G W, Shidhar, K. Laminar length of a non-Newtonian fluid jet. *Journal of Non-Newtonian Fluid Mechanics*; 1984; 15; 13-27.
- Lamb, H. *Hydrodynamics*. Cambridge University Press, Cambridge, 1959.
- Landau, L.D., Lifshitz, E.M. *Fluid Mechanics*. Pergamon Press, New York, 1987.
- Larson, R. *Constitutive Equations for Polymer Melts and Solutions*. Butterworths, New York, 1988.
- Li, H Z, Mouline, Y, Choplin, L, Midoux, N. Chaotic bubble coalescence in non-Newtonian fluids. *Int. J. Multiphase Flow*; 1997; 23; 713-23.
- Li, Y, Sadakata, M. Study of gypsum formation for appropriate dry desulfurization process of flue gas; 1999; *Fuel*; 78; 1089-95.
- Loitsyanskii, L.G. *Mechanics of Liquids and Gases*. Pergamon Press, Oxford, 1966.
- Maestro, A, Gonzalez, C, Gutierrez, J M. Shear thinning and thixotropy of HMHEC and HEC water solutions. *J. Rheol*; 2002; 46; 1445–1457
- McKinley, G. Elongational flows. Section C9.1.3 in *Springer Handbook of Experimental Fluid Mechanics*. (Eds. C. Tropea, A.L. Yarin and J. Foss), Heidelberg 2008.
- Mewis, J, Schryvers, J. unpublished; 1996; International Fine Particle Research Institute report.
- Mitwally, E M. Solutions of laminar jet flow problems for non-Newtonian power law fluids. *Trans. ASME, J. Fluids Eng.*; 1978; 100; 363–66.
- Moore, F. The rheology of ceramic slips and bodies; 1959; *Trans. Brit Ceramics Soc.*; 58; 470–494.

CITED LITERATURES

- Muñoz-Esparza, D, Buchlin, J-M, Myrillas, K, Berger, R. Numerical investigation of impinging gas jets onto deformable liquid layers. *Applied Mathematical Modelling*; 2012; 36; 2687–700.
- Narayanan, N, Ramamurthy, K. Structure and properties of aerated concrete: a review; *Cement and Concrete Composites*; 2000; 22; 321–29.
- No, S-Y. A Review on empirical correlations for jet/spray trajectory of liquid jet in uniform cross flow. *International Journal of Spray and Combustion Dynamics*; 2015; 7; 283-313.
- Olivier JGK, Janssens-Maenhout G, Peters JAHW. Trends in global CO₂ emissions; 2012 report. PBL Netherlands Environmental Assessment Agency, The Hague, Netherlands; 2012.
- Pavlov, K V. Theory of a flat submerged jet of a non-Newtonian liquid with a power rheological law. *Journal of Applied Mechanics and Technical Physics*; 1979; 20; 59-62.
- Prandtl, L. *Essential of Fluid Dynamics*. Hafner, New York, 1952.
- Radl, S, Khinast, J G. Prediction of mass transfer coefficients in non-Newtonian fermentation media using first-principles methods. *Biotechnology and Bioengineering*; 2007; 97, 1329-34.
- Schlichting, H. *Boundary-layer Theory*. McGraw-Hill, New York, 1968.
- Schneider M, Romer M, Tschudin M, Bolio H. Sustainable cement production – present and future. *Cem Concr Res*; 2011; 41; 642–50
- Serth, RW. The axisymmetric free laminar jet of a power law fluid. *J. Appl. Math. Phys.*; 1972; 23; 131–38.
- Sinha-Ray, S., R. Srikar, C.C. Lee, A. Li, A.L. Yarin. Shear and elongational rheology of gypsum slurries. *Applied Rheology* 21, 63071 (2011).

CITED LITERATURES

- Sorrentino F. Chemistry and engineering of the production process: State of the art; *Cem Concr Res* 2011;41; 616–23
- Sucech, S W. Producing foamed gypsum board using a foaming agent blend; 1997; US 5643510 A.
- te Nijenhuis, K. Viscoelastic polymeric fluids. Section C9.1 in *Springer Handbook of Experimental Fluid Mechanics*. (Eds. C. Tropea, A.L. Yarin and J. Foss), Heidelberg 2008.
- Tesárek,P, Drchalová,J, Kolísko, J, Rovnaníková, P, Černý, R. Flue gas desulfurization gypsum: Study of basic mechanical, hydric and thermal properties; 2007; *Construction and Building Materials*; 21; 1500-9.
- Tiu, C, Boger, D, V. Complete rheological characterization of time dependent food products; 1974; *J. Texture Stud.*; 5; 329–338.
- Tiwari, M K, Bazilevsky, A V, Yarin, A L, Megaridis, C M. Elongational and shear rheology of carbon nanotube suspensions. *Rheologica Acta*; 2009; 48; 597-609.
- Tonyan, T D, Gibson, L J. Structure and mechanics of cement foams; *Journal of Materials Science*; 1992; 27; 6371-78.
- van Dyke, M. *Perturbation Methods in Fluid Mechanics*. New York, Academic Press, 1964.
- UN Documents. World Commission on Environment and Development. Our Common Future. Chapter 2: Towards sustainable development. Oxford: Oxford University Press; 1987.
- Waehrer, GM , Dong, XH, Miller, T, Haile, E, Men, Y. Costs of occupational injuries in construction in the United States; 2007; *Accid Anal Prev.*; 39; 1258-66.

CITED LITERATURES

Wei, D. M., Al-Ashhab, S. Similarity solutions for non-Newtonian power-law fluid flow.

Applied Mathematics and Mechanics; 2014; 35; 1155-66.

Wild, G, Poncin, S, Li, H Z, Olmos, E. Some aspects of the hydrodynamics of bubble

columns. *International Journal of Chemical Reactor Engineering*; 2003; 1; 1542-6580.

Wittbold J R, Duvedi A P, Hemphill M K, Fleming W A, Pittman W G, Moore K S, Nelson C.

Slurry mixer outlet; 2002; US 6494609 B1.

Wittbold, JR, Petersen, BL, Li, A. Foamed slurry and building panel made therefrom; 2011; US

6774146 B2.

Yarin, A.L. Aerodynamics of a gas flame serving as a source of solid particles", *Combustion,*

Explosion and Shock Waves, 20, 686 - 689 (1984).

Yarin, A L. *Free Liquid Jets and Films: Hydrodynamics and Rheology*. Longman, Harlow and

John Wiley& Sons, New York, 1993.

Yarin A L, Zussman, E, Theron, A. Elongational behavior of gelled propellant simulants; *J.*

Rheol.; 48; 101-16.

Zhang, Z , Provis, JL , Reid, A, Wang, H. Geopolymer foam concrete: An emerging material for

sustainable construction; *Construction and Building Materials* 2014; 56; 113-27.

Zhang,L, Yang, C Mao, Z-S. Numerical simulation of a bubble rising in shear-thinning fluids.

Journal of non-Newtonian Fluid Mechanics; 2010; 165; 555-67.

CITED LITERATURES

Zussman, E, Yarin A. L. Age- and flow-dependency of salivary viscoelasticity. *J Dent Res.*; 2007; 86; 281-5.

APPENDIX 1: Computer code in FORTRAN developed to predict flow in straight foam jets issued into stagnant slurry

```
INTEGER N,N2,I,J,GA, TOP,CSS,SCC,PT,NXXG,NYYG,SINGLE
REAL*8 HC,EP, TI,DD, VZZZ,FIII, WSR,A,B,NRHEOL,KRHEOL,
&MU0CGS,MUK,RAVZ,VZMAX05,R05
REAL*8 SC,RSR0,VZ0,R0
REAL*8 ATD,DEL,X,Y01,R,R1,RR2,
&AT(40)
REAL*8 VZ(41),FI(41),RO(41),FUN(41),R2(41)
REAL*8 VZZ(41,41),FII(41,41),YY(41,41),XX(41,41)
REAL*8 YF(82)
LOGICAL FIR
EXTERNAL FC
COMMON/SAS/HC,SC,RSR0,N
COMMON/IDI/ATD(41),DEL(41)
COMMON/VISC/WSR,VZ0,R0,MU0CGS,A(7),B(7),NRHEOL(41),KRHEOL(41),
&MUK(41),RAVZ(41)
open(8,file='km5.dat',status='unknown')
open(18,file='km4.dat',status='unknown')
open(28,file='km1.dat',status='unknown')
open(38,file='km2.dat',status='unknown')
open(71,file='km471.dat',status='unknown')
open(72,file='km472.dat',status='unknown')
READ(*,*)VZ0,R0,SC,RSR0,WSR,N, TOP,PT,NXXG,NYYG,SINGLE
WRITE(*,*)'VZ0=',VZ0,'R0=',R0,'SC=',SC,'RSR0=',RSR0,'WSR=',WSR,
&'N=',N,'TOP=',TOP,'PT=',PT,'NXXG=',NXXG,'NYYG=',NYYG,
```

```
&'SINGLE=',SINGLE  
CSS=0  
SCC=0  
N2=2*(N+1)  
EP=.0001  
MU0CGS=.1  
IF(WSR.EQ.68.)THEN  
A(1)=5.065  
A(2)=4.355  
A(3)=-33.25  
A(4)=37.44  
A(5)=-15.32  
A(6)=2.143  
A(7)=.042  
B(1)=41912.  
B(2)=-156380.  
B(3)=225770.  
B(4)=-157420.  
B(5)=54116.  
B(6)=-8844.2  
B(7)=871.5  
END IF  
IF(WSR.EQ.75.)THEN  
A(1)=137.5  
A(2)=-236.0  
A(3)=134.3  
A(4)=-27.53
```

```
A(5)=1.247
A(6)=0.267
A(7)=.0
B(1)=-15734.
B(2)=26645.
B(3)=-14699.
B(4)=28320.
B(5)=-1310.
B(6)=440.
B(7)=0.
END IF
DD=1./N*(1./2.)
DO 3 I=1,N-1
TI=I*DD
AT(I)=3.*TI**2-2.*TI**3
3 CONTINUE
AT(N)=1./2.
ATD(1)=0.0
DO 33 I=2,N+1
ATD(I)=AT(I-1)
33 CONTINUE
DEL(1)=ATD(1)
DO 4 I=1,N
DEL(I+1)=ATD(I+1)-ATD(I)
4 CONTINUE
TI=(DEL(N-1)+DEL(N)+DEL(N+1))/3.
DO 8 I=N-1,N+1
```

```
DEL(I)=TI
8 CONTINUE
ATD(N-1)=ATD(N-2)+DEL(N-1)
ATD(N)=ATD(N-1)+DEL(N)
ATD(N+1)=1./2.
WRITE(6,10)ATD
WRITE(6,10)DEL
10 FORMAT(5F16.4)
DO 5 I=1,N
YF(I)=1.
YF(N+1+I)=1.
5 CONTINUE
YF(N+1)=0.0
YF(2*N+2)=0.0
X=0.0
DO 1 GA=1, TOP
WRITE(6,100)GA,HC,X
100 FORMAT(I8,F16.15,F16.8)
IF(GA.EQ.1)GO TO 99
CSS=CSS+1
99 CONTINUE
IF(GA.EQ.1)Y01=1.E-7
IF(GA.EQ.2)Y01=.01-1.E-7
IF(GA.GT.2)Y01=.01
FIR=.FALSE.
IF(GA.EQ.1)FIR=.TRUE.
CALL KUTTA(N2,X,YF,EP,Y01,FC,FIR)
```

```
IF(CSS.EQ.PT)THEN
SCC=SCC+1
DO 6 I=1,N+1
VZ(I)=YF(I)
FI(I)=YF(N+1+I)
IF(VZ(I).LT.0.0)VZ(I)=0.0
IF(FI(I).LT.0.0)FI(I)=0.0
6 CONTINUE
DO 700 I=1,N
RO(I)=FI(I)+RSR0*(1.-FI(I))
700 CONTINUE
DO 701 I=1,N
FUN(I)=1./(RO(I)*FI(I)*VZ(I))
701 CONTINUE
R2(1)=0.0
DO 7 I=2,N
R2(I)=R2(I-1)+(ATD(I)-ATD(I-1))*(FUN(I-1)+FUN(I))
7 CONTINUE
DO 20 I=1,N
R=R2(I)**.5
R1=VZ(I)
RR2=FI(I)
IF(SCC.EQ.SINGLE)THEN
WRITE(8,21)R,R1
21 FORMAT(2F16.8)
WRITE(18,219)R,RR2
219 FORMAT(2F16.8)
```

```
END IF
XX(SCC,I)=X
YY(SCC,I)=R
VZZ(SCC,I)=R1
FII(SCC,I)=RR2
20 CONTINUE
VZMAX05=VZ(1)/2.
DO 1003 I=2,N
IF((VZ(I-1).GE.VZMAX05).AND.(VZ(I).LE.VZMAX05))THEN
R05=(R2(I-1)**.5+R2(I)**.5)/2.
GO TO 1004
END IF
1003 CONTINUE
1004 CONTINUE
WRITE(38,1005)X,R05
1005 FORMAT(2F16.8)
IF(SCC.EQ.SINGLE)THEN
C NRHEOL(1)=NRHEOL(2)
C KRHEOL(1)=KRHEOL(2)
MUK(1)=MUK(2)
RAVZ(1)=0.0
DO 1000 I=1,N
C R1=NRHEOL(I)
C RR2=KRHEOL(I)
RR2=MUK(I)
R1=RAVZ(I)
R=R2(I)**.5
```

```
WRITE(28,1001)R,RR2,R1
1001 FORMAT(3F16.8)
1000 CONTINUE

END IF

CSS=0

END IF

1 CONTINUE

WRITE(71,*) 'VARIABLES = "X", "Y", "VZZZ"'
WRITE(71,*)'ZONE F=POINT, I=', NXXG, ', J=', NYYG
DO 471 I=1,NXXG
DO 472 J=1,NYYG
R1=XX(I,J)
RR2=YY(I,J)
VZZZ=VZZ(I,J)
WRITE(71,473)R1,RR2,VZZZ
473 FORMAT(3F16.8)
472 CONTINUE
471 CONTINUE

WRITE(72,*) 'VARIABLES = "X", "Y", "FIII"'
WRITE(72,*)'ZONE F=POINT, I=', NXXG, ', J=', NYYG
DO 481 I=1,NXXG
DO 482 J=1,NYYG
R1=XX(I,J)
RR2=YY(I,J)
FIII=FII(I,J)
WRITE(72,483)R1,RR2,FIII
483 FORMAT(3F16.8)
```

482 CONTINUE

481 CONTINUE

STOP

END

SUBROUTINE KUTTA(N,X,Y,EPS,H,FCT,FIRST)

REAL*8 SC,RSR0

REAL*8 X,EPS,H,ERROR,HC,DOP

REAL*8 ATD,DEL

REAL*8 WSR,A,B,NRHEOL,KRHEOL,VZ0,R0,MU0CGS,MUK,RAVZ

INTEGER N,I,LOC,PLOC,NN

LOGICAL FIRST,INCREA,SAD

REAL*8 Y(82),Y1(82),Y2(82),F0(82),F1(82),F2(82)

COMMON/SAS/HC,SC,RSR0,NN

COMMON/IDI/ATD(41),DEL(41)

COMMON/VISC/WSR,VZ0,R0,MU0CGS,A(7),B(7),NRHEOL(41),KRHEOL(41),
&MUK(41),RAVZ(41)

PLOC=1

IF(FIRST)HC=H

IF(FIRST)GO TO 1

2 IF(PLOC.LT.DABS(H/HC))PLOC=PLOC*2

IF(PLOC.LT.DABS(H/HC))GO TO 2

HC=H/PLOC

1 LOC=0

3 CALL FCT(X,Y,F0)

DO 4 I=1,N

4 Y1(I)=Y(I)+HC/3*F0(I)

CALL FCT(X+HC/3,Y1,F1)

```

DO 5 I=1,N
5 Y1(I)=Y(I)+(F0(I)+F1(I))*HC/6
  CALL FCT(X+HC/3,Y1,F1)
  DO 6 I=1,N
6 Y1(I)=Y(I)+(F0(I)+3*F1(I))*HC/8
  CALL FCT(X+HC/2,Y1,F2)
  DO 7 I=1,N
7 Y1(I)=Y(I)+(F0(I)-3*F1(I)+4*F2(I))*HC/2
  CALL FCT(X+HC,Y1,F1)
  DO 8 I=1,N
8 Y2(I)=Y(I)+(F0(I)+4*F2(I)+F1(I))*HC/6
  INCREA=.TRUE.
  DO 10 I=1,N
  DOP=1.0
  IF(DABS(Y1(I)).GT.1)DOP=Y1(I)
9 ERROR=DABS(.2*(Y1(I)-Y2(I))/DOP)
  IF(ERROR.LE.EPS)GO TO 10
  HC=HC/2.
  PLOC=2*PLOC
  LOC=2*LOC
  GO TO 3
10 IF(ERROR*64.GT.EPS)INCREA=.FALSE.
  X=X+HC
  DO 11 I=1,N
11 Y(I)=Y2(I)
  LOC=LOC+1
  IF(LOC.GE.PLOC)GO TO 12

```

```

SAD=INCREA.AND.LOC.EQ.LOC/2*2
SAD=.NOT.SAD
IF(SAD)GO TO 14
HC=2.*HC
LOC=LOC/2
PLOC=PLOC/2
14 GO TO 3
12 RETURN
END
SUBROUTINE FC(XK,YK,FK)
INTEGER N,I
REAL*8 SC,RSR0
REAL*8 XK,HC,
&ATD,DEL,RV,RV1,RAB,
&VZ(41),FI(41),S(41),R(41),Z(41),V(41),W(41),
&F(41),
&RAVZ,RAFI(41),EAVZ(41),EAFI(41),RAQ(41),RAM(41),INTE(41)
REAL*8 MU(41),RO(41),FUN(41),R2(41),P(41),Q(41),L(41),M(41)
REAL*8 YK(82),FK(82)
REAL*8 WSR,A,B,NRHEOL,KRHEOL,VZ0,R0,MU0CGS,MUK
COMMON/SAS/HC,SC,RSR0,N
COMMON/IDI/ATD(41),DEL(41)
COMMON/VISC/WSR,VZ0,R0,MU0CGS,A(7),B(7),NRHEOL(41),KRHEOL(41),
&MUK(41),RAVZ(41)
DO 1 I=1,N+1
VZ(I)=YK(I)
FI(I)=YK(N+1+I)

```

IF(VZ(I).LT.0.0)VZ(I)=0.0

IF(FI(I).LT.0.0)FI(I)=0.0

1 CONTINUE

DO 2 I=2,N

RV=DEL(I)+DEL(I+1)

RV1=DEL(I)*DEL(I+1)

S(I)=DEL(I)/(DEL(I+1)*RV)

R(I)=DEL(I+1)/(DEL(I)*RV)

Z(I)=(DEL(I+1)-DEL(I))/RV1

V(I)=2./(DEL(I+1)*RV)

W(I)=2./(DEL(I)*RV)

F(I)=2./RV1

2 CONTINUE

DO 3 I=2,N

RAVZ(I)=S(I)*VZ(I+1)-R(I)*VZ(I-1)+Z(I)*VZ(I)

RAFI(I)=S(I)*FI(I+1)-R(I)*FI(I-1)+Z(I)*FI(I)

EAVZ(I)=V(I)*VZ(I+1)+W(I)*VZ(I-1)-F(I)*VZ(I)

EAFI(I)=V(I)*FI(I+1)+W(I)*FI(I-1)-F(I)*FI(I)

3 CONTINUE

C VISCOSITY CALCULATION

DO 702 I=2,N

KRHEOL(I)=B(1)*FI(I)**6+B(2)*FI(I)**5+B(3)*FI(I)**4+B(4)*FI(I)**3

&+B(5)*FI(I)**2+B(6)*FI(I)+B(7)

NRHEOL(I)=A(1)*FI(I)**6+A(2)*FI(I)**5+A(3)*FI(I)**4+A(4)*FI(I)**3

&+A(5)*FI(I)**2+A(6)*FI(I)+A(7)

702 CONTINUE

DO 705 I=2,N

INTE(I)=KRHEOL(I)*(VZ0/R0)**(NRHEOL(I)-1.)/MU0CGS

MUK(I)=1.

IF(FI(I).LE..5)MUK(I)=INTE(I)*DABS(RAVZ(I)**(NRHEOL(I)-1.))

IF(MUK(I).GT.5.)MUK(I)=5.

MU(I)=MUK(I)

705 CONTINUE

C VISCOSITY CALCULATION

DO 700 I=1,N

RO(I)=FI(I)+RSR0*(1.-FI(I))

700 CONTINUE

DO 701 I=1,N

FUN(I)=1./(RO(I)*FI(I)*VZ(I))

701 CONTINUE

R2(1)=0.0

DO 7 I=2,N

R2(I)=R2(I-1)+(ATD(I)-ATD(I-1))*(FUN(I-1)+FUN(I))

7 CONTINUE

DO 703 I=2,N

P(I)=MU(I)*RO(I)*R2(I)*FI(I)**2*VZ(I)

Q(I)=MU(I)*RO(I)*R2(I)*FI(I)*VZ(I)

L(I)=RO(I)**2*R2(I)*FI(I)**2*VZ(I)/SC

M(I)=RO(I)**2*R2(I)*FI(I)*VZ(I)

703 CONTINUE

P(1)=P(2)

Q(1)=Q(2)

L(1)=L(2)

M(1)=M(2)

```
P(N+1)=0.0
Q(N+1)=0.0
L(N+1)=0.0
M(N+1)=0.0
DO 704 I=2,N
  RAQ(I)=S(I)*Q(I+1)-R(I)*Q(I-1)+Z(I)*Q(I)
  RAM(I)=S(I)*M(I+1)-R(I)*M(I-1)+Z(I)*M(I)
704 CONTINUE
DO 4 I=2,N
  RAB=RO(I)**2*R2(I)*FI(I)*VZ(I)/SC
  FK(I)=P(I)*EAVZ(I)+FI(I)*RAQ(I)*RAVZ(I)-RAB*RAFI(I)*RAVZ(I)
  FK(N+1+I)=L(I)*EAFI(I)+FI(I)/SC*RAM(I)*RAFI(I)-RAB*RAFI(I)**2
4 CONTINUE
FK(1)=FK(2)
FK(N+2)=FK(N+3)
FK(N+1)=0.0
FK(2*N+2)=0.0
RETURN
END
```

APPENDIX 2: Computer code in FORTRAN developed to predict flow in foam jets issued into slurry cross-flow

```
INTEGER N,N2,I,J,GA, TOP,CSS,SCC,PT,NXXG,NYYG,SINGLE
REAL*8 HC,EP, TI,DD, VZZZ,FIII,WSR,A,B,NRHEOL,KRHEOL,
&MU0CGS,MUK,RAVZ,VZMAX05,R05
REAL*8 SC,RSR0,VZ0,R0,RAB
REAL*8 CD,UB,PI,ALF0,Z0,AA
REAL*8 ATD,DEL,X,Y01,R,R1,RR2,
&AT(40)
REAL*8 VZ(41),FI(41),RO(41),FUN(41),R2(41)
REAL*8 VZZ(41,41),FII(41,41),YY(41,41),XX(41,41)
REAL*8 YF(85)
LOGICAL FIR
EXTERNAL FC
COMMON/SAS/HC,SC,RSR0,N
COMMON/IDI/ATD(41),DEL(41),CD,UB,PI,Z0
COMMON/VISC/WSR,VZ0,R0,MU0CGS,A(7),B(7),NRHEOL(41),KRHEOL(41),
&MUK(41),RAVZ(41)
open(8,file='km5.dat',status='unknown')
open(18,file='km4.dat',status='unknown')
open(28,file='km1.dat',status='unknown')
open(38,file='km2.dat',status='unknown')
open(71,file='km471.dat',status='unknown')
open(72,file='km472.dat',status='unknown')
open(78,file='km11.dat',status='unknown')
open(88,file='km12.dat',status='unknown')
```

```

open(98,file='km13.dat',status='unknown')
READ(*,*)VZ0,R0,SC,RSR0,WSR,
&CD,UB,ALF0,N,TOP,PT,NXXG,NYYG,SINGLE
WRITE(*,*)'VZ0=',VZ0,'R0=',R0,'SC=',SC,'RSR0=',RSR0,'WSR=',WSR,
&'CD=',CD,'UB=',UB,'ALF0=',ALF0,
&'N=',N,'TOP=',TOP,'PT=',PT,'NXXG=',NXXG,'NYYG=',NYYG,
&'SINGLE=',SINGLE
PI=3.141592653589793
ALF0=ALF0*PI/180.
Z0=.001
AA=RSR0*CD*UB*(UB**2+1.)**.5/PI
CSS=0
SCC=0
N2=2*(N+1)+3
EP=.0001
MU0CGS=.1
IF(WSR.EQ.68.)THEN
A(1)=5.065
A(2)=4.355
A(3)=-33.25
A(4)=37.44
A(5)=-15.32
A(6)=2.143
A(7)=.042
B(1)=41912.
B(2)=-156380.
B(3)=225770.

```

```
B(4)=-157420.  
B(5)=54116.  
B(6)=-8844.2  
B(7)=871.5  
END IF  
IF(WSR.EQ.75.)THEN  
A(1)=137.5  
A(2)=-236.0  
A(3)=134.3  
A(4)=-27.53  
A(5)=1.247  
A(6)=0.267  
A(7)=.0  
B(1)=-15734.  
B(2)=26645.  
B(3)=-14699.  
B(4)=28320.  
B(5)=-1310.  
B(6)=440.  
B(7)=0.  
END IF  
DD=1./N*(1./2.)  
DO 3 I=1,N-1  
TI=I*DD  
AT(I)=3.*TI**2-2.*TI**3  
3 CONTINUE  
AT(N)=1./2.
```

```
ATD(1)=0.0
DO 33 I=2,N+1
  ATD(I)=AT(I-1)
33 CONTINUE
  DEL(1)=ATD(1)
  DO 4 I=1,N
    DEL(I+1)=ATD(I+1)-ATD(I)
4 CONTINUE
  TI=(DEL(N-1)+DEL(N)+DEL(N+1))/3.
  DO 8 I=N-1,N+1
    DEL(I)=TI
8 CONTINUE
  ATD(N-1)=ATD(N-2)+DEL(N-1)
  ATD(N)=ATD(N-1)+DEL(N)
  ATD(N+1)=1./2.
  WRITE(6,10)ATD
  WRITE(6,10)DEL
10 FORMAT(5F16.4)
  DO 5 I=1,N
    YF(I)=1.
    YF(N+1+I)=1.
5 CONTINUE
  YF(N+1)=0.0
  YF(2*N+2)=0.0
  IF(DABS(ALF0-PI/2.).LE..01)THEN
  YF(2*N+2+1)=Z0
  YF(2*N+2+2)=1./(AA*Z0)
```

```
END IF
IF(DABS(ALF0-PI/2.).GT..01)THEN
YF(2*N+2+1)=0.0
YF(2*N+2+2)=DTAN(ALF0)
END IF
X=0.0
DO 1 GA=1, TOP
WRITE(6,100)GA,HC,X
100 FORMAT(I8,F16.15,F16.8)
IF(GA.EQ.1)GO TO 99
CSS=CSS+1
99 CONTINUE
IF(GA.EQ.1)Y01=1.E-7
IF(GA.EQ.2)Y01=.01-1.E-7
IF(GA.GT.2)Y01=.01
FIR=.FALSE.
IF(GA.EQ.1)FIR=.TRUE.
CALL KUTTA(N2,X,YF,EP,Y01,FC,FIR)
IF(CSS.EQ.PT)THEN
SCC=SCC+1
DO 6 I=1,N+1
VZ(I)=YF(I)
FI(I)=YF(N+1+I)
IF(VZ(I).LT.0.0)VZ(I)=0.0
IF(FI(I).LT.0.0)FI(I)=0.0
6 CONTINUE
DO 700 I=1,N
```

```

      RO(I)=FI(I)+RSR0*(1.-FI(I))
700 CONTINUE
      DO 701 I=1,N
          FUN(I)=1./(RO(I)*FI(I)*VZ(I))
701 CONTINUE
          R2(1)=0.0
          DO 7 I=2,N
              R2(I)=R2(I-1)+(ATD(I)-ATD(I-1))*(FUN(I-1)+FUN(I))
7 CONTINUE
          DO 20 I=1,N
              R=R2(I)**.5
              R1=VZ(I)
              RR2=FI(I)
              IF(SCC.EQ.SINGLE)THEN
                  WRITE(8,21)R,R1
21 FORMAT(2F16.8)
                  WRITE(18,219)R,RR2
219 FORMAT(2F16.8)
              END IF
              XX(SCC,I)=X
              YY(SCC,I)=R
              VZZ(SCC,I)=R1
              FII(SCC,I)=RR2
20 CONTINUE
          VZMAX05=VZ(1)/2.
          DO 1003 I=2,N
              IF((VZ(I-1).GE.VZMAX05).AND.(VZ(I).LE.VZMAX05))THEN

```

```
R05=(R2(I-1)**.5+R2(I)**.5)/2.  
GO TO 1004  
END IF  
1003 CONTINUE  
1004 CONTINUE  
WRITE(38,1005)X,R05  
1005 FORMAT(2F16.8)  
R=YF(2*N+2+1)  
WRITE(78,1006)X,R  
1006 FORMAT(2F16.8)  
RAB=YF(2*N+2+2+1)  
R=VZ(1)  
WRITE(88,1007)RAB,R  
1007 FORMAT(2F16.8)  
R=FI(1)  
WRITE(98,1008)RAB,R  
1008 FORMAT(2F16.8)  
IF(SCC.EQ.SINGLE)THEN  
C NRHEOL(1)=NRHEOL(2)  
C KRHEOL(1)=KRHEOL(2)  
MUK(1)=MUK(2)  
RAVZ(1)=0.0  
DO 1000 I=1,N  
C R1=NRHEOL(I)  
C RR2=KRHEOL(I)  
RR2=MUK(I)  
R1=RAVZ(I)
```

```
R=R2(I)**.5
WRITE(28,1001)R,RR2,R1
1001 FORMAT(3F16.8)
1000 CONTINUE
END IF
CSS=0
END IF
1 CONTINUE
WRITE(71,*) 'VARIABLES = "X", "Y", "VZZZ"'
WRITE(71,*)'ZONE F=POINT, I=', NXXG, ', J=', NYYG
DO 471 I=1,NXXG
DO 472 J=1,NYYG
R1=XX(I,J)
RR2=YY(I,J)
VZZZ=VZZ(I,J)
WRITE(71,473)R1,RR2,VZZZ
473 FORMAT(3F16.8)
472 CONTINUE
471 CONTINUE
WRITE(72,*) 'VARIABLES = "X", "Y", "FIII"'
WRITE(72,*)'ZONE F=POINT, I=', NXXG, ', J=', NYYG
DO 481 I=1,NXXG
DO 482 J=1,NYYG
R1=XX(I,J)
RR2=YY(I,J)
FIII=FII(I,J)
WRITE(72,483)R1,RR2,FIII
```

```
483 FORMAT(3F16.8)
482 CONTINUE
481 CONTINUE

  STOP

  END

  SUBROUTINE KUTTA(N,X,Y,EPS,H,FCT,FIRST)

  REAL*8 SC,RSR0

  REAL*8 X,EPS,H,ERROR,HC,DOP

  REAL*8 ATD,DEL

  REAL*8 CD,UB,PI,Z0

  REAL*8 WSR,A,B,NRHEOL,KRHEOL,VZ0,R0,MU0CGS,MUK,RAVZ

  INTEGER N,I,LOC,PLOC,NN

  LOGICAL FIRST,INCREA,SAD

  REAL*8 Y(85),Y1(85),Y2(85),F0(85),F1(85),F2(85)

  COMMON/SAS/HC,SC,RSR0,NN

  COMMON/IDI/ATD(41),DEL(41),CD,UB,PI,Z0

  COMMON/VISC/WSR,VZ0,R0,MU0CGS,A(7),B(7),NRHEOL(41),KRHEOL(41),
&MUK(41),RAVZ(41)

  PLOC=1

  IF(FIRST)HC=H

  IF(FIRST)GO TO 1

2 IF(PLOC.LT.DABS(H/HC))PLOC=PLOC*2

  IF(PLOC.LT.DABS(H/HC))GO TO 2

  HC=H/PLOC

1 LOC=0

3 CALL FCT(X,Y,F0)

  DO 4 I=1,N
```

```

4 Y1(I)=Y(I)+HC/3*F0(I)
  CALL FCT(X+HC/3,Y1,F1)
  DO 5 I=1,N
5 Y1(I)=Y(I)+(F0(I)+F1(I))*HC/6
  CALL FCT(X+HC/3,Y1,F1)
  DO 6 I=1,N
6 Y1(I)=Y(I)+(F0(I)+3*F1(I))*HC/8
  CALL FCT(X+HC/2,Y1,F2)
  DO 7 I=1,N
7 Y1(I)=Y(I)+(F0(I)-3*F1(I)+4*F2(I))*HC/2
  CALL FCT(X+HC,Y1,F1)
  DO 8 I=1,N
8 Y2(I)=Y(I)+(F0(I)+4*F2(I)+F1(I))*HC/6
  INCREA=.TRUE.
  DO 10 I=1,N
  DOP=1.0
  IF(DABS(Y1(I)).GT.1)DOP=Y1(I)
9 ERROR=DABS(.2*(Y1(I)-Y2(I))/DOP)
  IF(ERROR.LE.EPS)GO TO 10
  HC=HC/2.
  PLOC=2*PLOC
  LOC=2*LOC
  GO TO 3
10 IF(ERROR*64.GT.EPS)INCREA=.FALSE.
  X=X+HC
  DO 11 I=1,N
11 Y(I)=Y2(I)

```

```

LOC=LOC+1
IF(LOC.GE.PLOC)GO TO 12
SAD=INCREA.AND.LOC.EQ.LOC/2*2
SAD=.NOT.SAD
IF(SAD)GO TO 14
HC=2.*HC
LOC=LOC/2
PLOC=PLOC/2
14 GO TO 3
12 RETURN
END
SUBROUTINE FC(XK,YK,FK)
INTEGER N,I
REAL*8 SC,RSR0
REAL*8 CD,UB,PI,Z0,FF,R12,R1,R22
REAL*8 XK,HC,
&ATD,DEL,RV,RV1,RAB,
&VZ(41),FI(41),S(41),R(41),Z(41),V(41),W(41),
&F(41),
&RAVZ,RAFI(41),EAVZ(41),EAFI(41),RAQ(41),RAM(41),INTE(41)
REAL*8 MU(41),RO(41),FUN(41),R2(41),P(41),Q(41),L(41),M(41)
REAL*8 YK(85),FK(85)
REAL*8 RAD(41),VZNORM(41)
REAL*8 WSR,A,B,NRHEOL,KRHEOL,VZ0,R0,MU0CGS,MUK
COMMON/SAS/HC,SC,RSR0,N
COMMON/IDI/ATD(41),DEL(41),CD,UB,PI,Z0
COMMON/VISC/WSR,VZ0,R0,MU0CGS,A(7),B(7),NRHEOL(41),KRHEOL(41),

```

&MUK(41),RAVZ(41)

DO 1 I=1,N+1

VZ(I)=YK(I)

FI(I)=YK(N+1+I)

IF(VZ(I).LT.0.0)VZ(I)=0.0

IF(FI(I).LT.0.0)FI(I)=0.0

1 CONTINUE

FF=YK(2*N+2+2)

DO 2 I=2,N

RV=DEL(I)+DEL(I+1)

RV1=DEL(I)*DEL(I+1)

S(I)=DEL(I)/(DEL(I+1)*RV)

R(I)=DEL(I+1)/(DEL(I)*RV)

Z(I)=(DEL(I+1)-DEL(I))/RV1

V(I)=2./(DEL(I+1)*RV)

W(I)=2./(DEL(I)*RV)

F(I)=2./RV1

2 CONTINUE

DO 3 I=2,N

RAVZ(I)=S(I)*VZ(I+1)-R(I)*VZ(I-1)+Z(I)*VZ(I)

RAFI(I)=S(I)*FI(I+1)-R(I)*FI(I-1)+Z(I)*FI(I)

EAVZ(I)=V(I)*VZ(I+1)+W(I)*VZ(I-1)-F(I)*VZ(I)

EAFI(I)=V(I)*FI(I+1)+W(I)*FI(I-1)-F(I)*FI(I)

3 CONTINUE

C VISCOSITY CALCULATION

DO 702 I=2,N

KRHEOL(I)=B(1)*FI(I)**6+B(2)*FI(I)**5+B(3)*FI(I)**4+B(4)*FI(I)**3

&+B(5)*FI(I)**2+B(6)*FI(I)+B(7)

NRHEOL(I)=A(1)*FI(I)**6+A(2)*FI(I)**5+A(3)*FI(I)**4+A(4)*FI(I)**3

&+A(5)*FI(I)**2+A(6)*FI(I)+A(7)

702 CONTINUE

DO 705 I=2,N

INTE(I)=KRHEOL(I)*(VZ0/R0)**(NRHEOL(I)-1.)/MU0CGS

MUK(I)=1.

IF(FI(I).LE..5)MUK(I)=INTE(I)*DABS(RAVZ(I))**(NRHEOL(I)-1.)

IF(MUK(I).GT.5.)MUK(I)=5.

MU(I)=MUK(I)

705 CONTINUE

C VISCOSITY CALCULATION

DO 700 I=1,N

RO(I)=FI(I)+RSR0*(1.-FI(I))

700 CONTINUE

DO 701 I=1,N

FUN(I)=1./(RO(I)*FI(I)*VZ(I))

701 CONTINUE

R2(1)=0.0

DO 7 I=2,N

R2(I)=R2(I-1)+(ATD(I)-ATD(I-1))*(FUN(I-1)+FUN(I))

7 CONTINUE

RAD(1)=0.0

DO 715 I=2,N

RAD(I)=R2(I)**.5

715 CONTINUE

DO 707 I=1,N+1

VZNORM(I)=VZ(I)/VZ(1)

707 CONTINUE

DO 706 I=2,N

R1=1./2.-VZNORM(I-1)

R22=1./2.-VZNORM(I)

IF((R1*R22).LT.0.0)R12=RAD(I)

706 CONTINUE

DO 703 I=2,N

P(I)=MU(I)*RO(I)*R2(I)*FI(I)**2*VZ(I)

Q(I)=MU(I)*RO(I)*R2(I)*FI(I)*VZ(I)

L(I)=RO(I)**2*R2(I)*FI(I)**2*VZ(I)/SC

M(I)=RO(I)**2*R2(I)*FI(I)*VZ(I)

703 CONTINUE

P(1)=P(2)

Q(1)=Q(2)

L(1)=L(2)

M(1)=M(2)

P(N+1)=0.0

Q(N+1)=0.0

L(N+1)=0.0

M(N+1)=0.0

DO 704 I=2,N

RAQ(I)=S(I)*Q(I+1)-R(I)*Q(I-1)+Z(I)*Q(I)

RAM(I)=S(I)*M(I+1)-R(I)*M(I-1)+Z(I)*M(I)

704 CONTINUE

DO 4 I=2,N

RAB=RO(I)**2*R2(I)*FI(I)*VZ(I)/SC

```

FK(I)=P(I)*EAVZ(I)+FI(I)*RAQ(I)*RAVZ(I)-RAB*RAFI(I)*RAVZ(I)
FK(N+1+I)=L(I)*EAFI(I)+FI(I)/SC*RAM(I)*RAFI(I)-RAB*RAFI(I)**2
4 CONTINUE
FK(1)=FK(2)
FK(N+2)=FK(N+3)
FK(N+1)=0.0
FK(2*N+2)=0.0
FK(2*N+2+1)=FF/(1.+FF**2)**.5
FK(2*N+2+2)=-RSR0*CD*UB**2*FF**2*R12*
&(1.-2.*VZ(1)/UB/(1.+FF**2)**.5+(VZ(1)/UB)**2)**.5
&/(2.*PI*.5)
FK(2*N+2+2+1)=(1.+FK(2*N+2+1)**2)**.5
RETURN
END

```

VITA

NAME: Dominic A. Dannelsa

EDUCATION: Bachelor of Engineering in Mechanical Engineering, Rayen School of Engineering, Youngstown State University, Youngstown, Ohio, USA, 1978

Master of Science in Mechanical Engineering, Rayen School of Engineering, Youngstown State University, Youngstown, Ohio, USA, 1981

Ph. D., Mechanical Engineering, University of Illinois at Chicago, Chicago, Illinois, USA, 2017

TEACHING: Lecturer in the Department of Mechanical Engineering, Rayen School of Engineering, Youngstown State University, Youngstown, Ohio USA, 1981-1985: Dynamics, Thermodynamics, Drafting, Hydraulics, Tool Design.

HONORS: Woodrow Wilson High School Valedictorian, 4.0 GPA, Youngstown, Ohio, USA, 1974

Rayen School of Engineering, Summa Cum Laude Graduate 3.98 GPA, Youngstown State University, Youngstown, Ohio, USA, 1978

Dean Louis A. Deesz Top Engineering Student Annual Award presented by the Mahoning Valley Society of Professional Engineers, Youngstown, Ohio, USA, 1978

Rayen School of Engineering, Magna Cum Laude Graduate, Youngstown State University, Youngstown, Ohio, USA, 1981

Phi Kappa Phi Honorary Academic Society Member

Tau Beta Pi Honorary Engineering Society Member

PROFESSIONAL

EXPERIENCE: Executive Vice President, Chief Operations & Innovation Officer, USG
Board Of Directors, USG Boral
Board Of Directors, USG Zawawi Gypsum LLC
Board Of Directors, USG Middle East
Board Of Directors, USG Mexico
Board Of Directors, Knauf-USG Systems Joint Ventures.

PROFESSIONAL

MEMBERSHIP: Industrial Research Institute (IRI)
National Association for Manufacturers
Naval War College Foundation
United States Merchant Marine Academy Superintendent's Council
United States Chamber of Commerce

PUBLICATIONS: Journals
Dannessa D, Sinha-Ray S, Jun S, Yarin A L. Numerical Investigation of
Foam Mixing in Gypsum Slurry. Part I: Straight Foam Jet into Gypsum
Slurry at Rest; 2017; Journal of non-Newtonian Fluid Mechanics
(submitted).

Dannessa D, Sinha-Ray S, Yarin A L. Numerical Investigation of Foam Mixing in Gypsum Slurry. Part II: Straight Foam Jet into Gypsum Slurry Crossflow; 2017; Journal of non-Newtonian Fluid Mechanics (submitted).

From: Kroeger Martin [mk@mat.ethz.ch]
Sent: Friday, February 03, 2017 2:36 PM
To: Dannessa, Dominic
Subject: RE: Copyright clearance for using figure to be used in thesis

Dear Dominic,

I hereby grant you permission to reprint any figure that appeared in Applied Rheology, as long as you quote the original article in the figure caption.

Kind regards, Martin Kroger
Editor Applied Rheology

--

Martin Kröger

Prof Computational Polymer Physics, Dr rer nat habil

www.complexfluids.ethz.ch

Swiss Federal Institute of Technology, ETH Zurich

Leopold-Ruzicka-Weg 4, D-MATL HCP F 48.2, CH-8093 ZURICH, Switzerland

phone +41-44-632-6622 fax -1076

Editor Appl Rheol | www.appliedrheology.org | e@appliedrheology.org

ResearcherID: C-1946-2008, ORCID: 0000-0003-1402-6714, Scopus Author ID 7005681007

From: Dannessa, Dominic [DDannessa@usg.com]
Sent: 03 February 2017 18:47
To: editors@appliedrheology.org; Applied Rheology (editors)
Subject: Copyright clearance for using figure to be used in thesis

To
The Editor
Applied Rheology

Dear Professor,

I will be defending my PhD thesis titled "Numerical investigation of foam mixing in gypsum slurry" in March 2017 from the Mechanical & Industrial Engineering Department of University of Illinois at Chicago. For the better depiction of my thesis and to provide background of the relevance of my PhD work, I referred to the following work- Article title: Shear and elongational rheology of gypsum slurries; Author(s): Suman Sinha-Ray, Raman Srikar, Chris C. Lee, Alfred Li, Alexander L. Yarin; DOI: 10.3933/AppRheol-21-63071". In this regard I am using Figure 2, 6 and 7 as a reference owing to their high relevance to my thesis.

I will really appreciate if you can provide me the copyright clearance to use this above mentioned figure as a part of my dissertation.

With Regards

Dominic Dannessa

(Doctoral Student, University of Illinois at Chicago)

Dominic A. Dannessa

Executive Vice President, USG Corporation;

Chief Operations and Innovation Officer

550 West Adams St. | Chicago, IL 60661

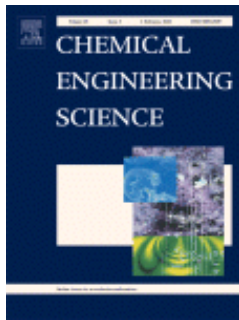
t 312.436.4316 | f 312.672.4316 | ddannessa@usg.com

 usg-logo-trans

IT'S YOUR WORLD. BUILD IT.™



RightsLink®

[Home](#)
[Account Info](#)
[Help](#)


Title: Continuous rise velocity of air bubbles in non-Newtonian biopolymer solutions

Author: Shahram Amirnia, John R. de Bruyn, Maurice A. Bergougnou, Argyrios Margaritis

Publication: Chemical Engineering Science

Publisher: Elsevier

Date: 3 May 2013

Logged in as:
Dominic Dannessa
University of Illinois at Chicago

[LOGOUT](#)

Copyright © 2013 Elsevier Ltd. All rights reserved.

Order Completed

Thank you for your order.

This Agreement between University of Illinois at Chicago -- Dominic Dannessa ("You") and Elsevier ("Elsevier") consists of your license details and the terms and conditions provided by Elsevier and Copyright Clearance Center.

Your confirmation email will contain your order number for future reference.

[Printable details.](#)

License Number	4041400411335
License date	Feb 03, 2017
Licensed Content Publisher	Elsevier
Licensed Content Publication	Chemical Engineering Science
Licensed Content Title	Continuous rise velocity of air bubbles in non-Newtonian biopolymer solutions
Licensed Content Author	Shahram Amirnia, John R. de Bruyn, Maurice A. Bergougnou, Argyrios Margaritis
Licensed Content Date	3 May 2013
Licensed Content Volume	94
Licensed Content Issue	n/a
Licensed Content Pages	9
Type of Use	reuse in a thesis/dissertation
Portion	figures/tables/illustrations
Number of figures/tables/illustrations	1
Format	both print and electronic
Are you the author of this Elsevier article?	No
Will you be translating?	No
Order reference number	
Original figure numbers	table 1
Title of your thesis/dissertation	NUMERICAL INVESTIGATION of FOAM MIXING in GYPSUM SLURRY
Expected completion date	May 2017
Estimated size (number of pages)	160
Elsevier VAT number	GB 494 6272 12
Requestor Location	University of Illinois at Chicago 842 W Taylor St

CHICAGO, IL 60607

United States
Attn: Dominic Danna
0.00 USD

Total

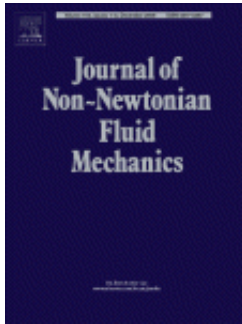
[ORDER MORE](#)

[CLOSE WINDOW](#)

Copyright © 2017 [Copyright Clearance Center, Inc.](#) All Rights Reserved. [Privacy statement.](#) [Terms and Conditions.](#)
Comments? We would like to hear from you. E-mail us at customer@copyright.com



RightsLink®

[Home](#)
[Account Info](#)
[Help](#)


Title: Laminar length of a non-Newtonian fluid jet

Author: K.R. Kumar,G.W. Rankin,K. Shidhar

Publication: Journal of Non-Newtonian Fluid Mechanics

Publisher: Elsevier

Date: 1984

Logged in as:
Dominic Dannessa
University of Illinois at Chicago

Account #:
3001108280

[LOGOUT](#)

Copyright © 1984 Published by Elsevier B.V.

Order Completed

Thank you for your order.

This Agreement between University of Illinois at Chicago -- Dominic Dannessa ("You") and Elsevier ("Elsevier") consists of your license details and the terms and conditions provided by Elsevier and Copyright Clearance Center.

Your confirmation email will contain your order number for future reference.

[Printable details.](#)

License Number	4041421050372
License date	Feb 03, 2017
Licensed Content Publisher	Elsevier
Licensed Content Publication	Journal of Non-Newtonian Fluid Mechanics
Licensed Content Title	Laminar length of a non-Newtonian fluid jet
Licensed Content Author	K.R. Kumar,G.W. Rankin,K. Shidhar
Licensed Content Date	1984
Licensed Content Volume	15
Licensed Content Issue	1
Licensed Content Pages	15
Type of Use	reuse in a thesis/dissertation
Portion	figures/tables/illustrations
Number of figures/tables/illustrations	1
Format	both print and electronic
Are you the author of this Elsevier article?	No
Will you be translating?	No
Order reference number	
Original figure numbers	Figure 1
Title of your thesis/dissertation	NUMERICAL INVESTIGATION of FOAM MIXING in GYPSUM SLURRY
Expected completion date	May 2017
Estimated size (number of pages)	160
Elsevier VAT number	GB 494 6272 12
Requestor Location	University of Illinois at Chicago 842 W Taylor St

CHICAGO, IL 60607

United States
Attn: Dominic Dannessa

Total 0.00 USD

[ORDER MORE](#)

[CLOSE WINDOW](#)

Copyright © 2017 [Copyright Clearance Center, Inc.](#) All Rights Reserved. [Privacy statement](#). [Terms and Conditions](#).
Comments? We would like to hear from you. E-mail us at customercare@copyright.com

From: PermissionsUK [PermissionsUK@sagepub.com]
Sent: Friday, February 03, 2017 6:24 PM
To: Dannessa, Dominic
Subject: RE: Copyright clearance for using figure in Thesis

Dear Dominic Dannessa,

Thank you for your email. I am pleased to report we can grant your request without a fee as part of your thesis.

Please accept this email as permission for your request as detailed below. Permission is granted for the life of the edition on a non-exclusive basis, in the English language, throughout the world in all formats provided full citation is made to the original SAGE publication.

As a courtesy, we ask that you contact the author to let them know the content will be republished. Please note this approval excludes any content which requires additional permission from a separate copyright holder. If the SAGE material includes anything not '© the Author' or '© SAGE', please contact the rights holder for permission to reuse those items.

If I may be of further assistance, please let me know.

Best Wishes,

Craig Myles
on behalf of **SAGE Ltd. Permissions Team**

SAGE Publishing
1 Oliver's Yard, 55 City Road
London, EC1Y 1SP
UK

www.sagepublishing.com

SAGE Publications Ltd, Registered in England No.1017514

Los Angeles | London | New Delhi

Singapore | Washington DC

The natural home for authors, editors & societies

Thank you for considering the environment before printing this email.

From: Dannessa, Dominic [<mailto:DDannessa@usg.com>]
Sent: Friday, February 03, 2017 9:46 AM
To: Journals <Journals@sagepub.com>; polifke@tfd.mw.tum.de
Subject: Copyright clearance for using figure in Thesis

To
The Editor
International journal of spray and combustion dynamics

Dear Professor Wolfgang Polifke,

I will be defending my PhD thesis titled "Numerical investigation of foam mixing in gypsum slurry" in March 2017 from the Mechanical & Industrial Engineering Department of University of Illinois at Chicago. For the better depiction of my thesis and to provide background of the relevance of my PhD work, I referred to the following work- Article title: A Review on Empirical Correlations for Jet/Spray Trajectory of Liquid Jet in Uniform Cross Flow; Author(s): No, Soo-Young;

DOI: 10.1260/1756-8277.7.4.283". In this regard I am using Figure 1 as a reference owing to their high relevance to my thesis.

I will really appreciate if you can provide me the copyright clearance to use this above mentioned figure as a part of my dissertation.

With Regards

Dominic Dannessa

(Doctoral Student, University of Illinois at Chicago)

Dominic A. Dannessa

Executive Vice President, USG Corporation;

Chief Operations and Innovation Officer

550 West Adams St. | Chicago, IL 60661

t 312.436.4316 | f 312.672.4316 | ddannessa@usg.com



IT'S YOUR WORLD. BUILD IT.™



Note: Copyright.com supplies permissions but not the copyrighted content itself.

1
PAYMENT

2
REVIEW

3
CONFIRMATION

Step 3: Order Confirmation

Thank you for your order! A confirmation for your order will be sent to your account email address. If you have questions about your order, you can call us 24 hrs/day, M-F at +1.855.239.3415 Toll Free, or write to us at info@copyright.com. This is not an invoice.

Confirmation Number: 11623374
Order Date: 02/03/2017

If you paid by credit card, your order will be finalized and your card will be charged within 24 hours. If you choose to be invoiced, you can change or cancel your order until the invoice is generated.

Payment Information

Dominic Danna
University of Illinois at Chicag
DDanna@usg.com
+1 (312)4364316
Payment Method: n/a

Order Details

Springer Handbook of Experimental Fluid Mechanics

Order detail ID: 70292722
Order License Id: 4041411081159
ISBN: 9783662491621
Publication Type: Book
Publisher: Springer

Permission Status: **Granted**

Permission type: Republish or display content
Type of use: Thesis/Dissertation

[Hide details](#)

Requestor type	Academic institution
Format	Print, Electronic
Portion	chart/graph/table/figure
Number of charts/graphs/tables/figures	6
Title or numeric reference of the portion(s)	Fig. 9.1, Fig. 9.7, Table 9.2, Table 9.5, Fig. 9.55, Fig. 9.56
Title of the article or chapter the portion is from	Non-Newtonian Flows
Editor of portion(s)	N/A
Author of portion(s)	Nijenhuis, Klaas (et al.)
Volume of serial or monograph	1
Page range of portion	619-743
Publication date of portion	2007
Rights for	Main product
Duration of use	Life of current edition

Creation of copies for the disabled	no
With minor editing privileges	no
For distribution to	Worldwide
In the following language(s)	Original language of publication
With incidental promotional use	no
Lifetime unit quantity of new product	Up to 999
Made available in the following markets	Education
The requesting person/organization	University of Illinois at Chicago
Order reference number	
Author/Editor	Dominic Dannessa
The standard identifier of New Work	not applicable
Title of New Work	NUMERICAL INVESTIGATION of FOAM MIXING in GYPSUM SLURRY
Publisher of New Work	University of Illinois at Chicago
Expected publication date	May 2017
Estimated size (pages)	160

Note: This item will be invoiced or charged separately through CCC's **RightsLink** service. [More info](#)

\$ 0.00

Total order items: 1

This is not an invoice.

Order Total: 0.00 USD